Near-infrared laser surface treatment of milled CFRP aircraft structures for bonded repair applications

Vom Promotionsausschuss der
Technischen Universität Hamburg

zur Erlangung des akademischen Grades

Doktor-Ingenieur (Dr.-Ing.)

genehmigte Dissertation

von
Sergej Harder

aus
Karaganda, Kasachstan

2020

Vorsitzender des

Prüfungsausschusses: Prof. Dr.-Ing. Benedikt Kriegesmann

Gutachter: Prof. Dr.-Ing. habil. Bodo Fiedler

Prof. Dr.-Ing. Wolfgang Hintze

Tag der mündlichen Prüfung: 02.10.2020

II

Technisch-Wissenschaftliche Schriftenreihe

Acknowledgements

Kurzfassung

Kohlenstofffaserverstärkte Kunststoffe (CFK) werden in erheblichem Umfang als Werkstoff für Flugzeugstrukturen eingesetzt. Während ihrer Lebensdauer können Flugzeugstrukturen Schäden erleiden, die zur Wahrung der Flugsicherheit repariert werden müssen. Die leichtbau- und werkstoffgerechte Klebeschäftreparatur wird durch Entfernen des beschädigten Materials durch Fräsen und das anschließende Aufbringen eines Reparaturflickens hergestellt. Ein kritischer Schritt hierbei ist die Oberflächenbehandlung.

In dieser Arbeit wurden die Auswirkungen der Nahinfrarot(N-IR)-Laser-Oberflächenbehandlung auf die Klebeigenschaften von gefrästem CFK untersucht. Die Laserbehandlung ist in der Lage, unerwünschte Fräspartikel von der Oberfläche zu entfernen. Dadurch wurde eine signifikante Steigerung der Klebfestigkeit erreicht. Zusätzlich bewirkt die Laserbehandlung eine Freilegung der Fasern. Dies verbessert die Klebfestigkeit gegenüber dem bereits hohen Wert des Referenzprozesses. Die Erhöhung der Rauheit und Vergrößerung der Oberfläche wird als treibender Mechanismus hinter der weitergehenden Verbesserung gesehen. Im Gegensatz zum Referenzverfahren ist die Laserbehandlung in der Lage, Kontaminationen zu entfernen. Die Entfernung von Kontaminationen ist ein wesentlicher Vorteil der Laserbehandlung angesichts des hohen Risikos, das von diesen ausgeht. Obwohl keine Hinweise auf eine Funktionalisierung beobachtet wurden, zeigt die Oberfläche eine hohe Funktionalität ohne Verunreinigungen und ist daher für eine Klebung geeignet. Der wesentliche Nachteil des Verfahrens ist die Wechselwirkung zwischen der Matrix und dem N-IR-Laser und die daraus resultierende Bildung von Kavitäten unter matrixreichen Bereichen. Die Kavitäten können nur teilweise gefüllt werden und könnten ein Versagen der Klebung verursachen.

Dennoch konnte bei allen getesteten Konfigurationen eine Steigerung der Klebfestigkeit gegenüber dem Referenzprozess erreicht werden. Dies zeigt das hohe Potenzial der N-IR-Laserbehandlung für Composite-Reparaturen.

Abstract

Carbon fibre reinforced polymers (CFRP) are widely used as a material for aircraft structures. During their lifetime, aircraft structures can be subject to damages that have to be repaired to maintain aircraft safety. For a lightweight and material-efficient repair, the scarf bonded joint is the preferred solution. The scarf bonded joint is produced by removing the damaged material by milling and the application of a repair patch through adhesive bonding. A critical step during the adhesive bonding process is surface treatment since it significantly influences the bond strength.

This work investigates the effects of near-infrared (N-IR) surface treatment on the adhesive properties of milled CFRP. The laser treatment is able to remove disruptive milling debris from the surface. As a result, a significant increase in bond strength is achieved. Furthermore, the laser treatment is able to strip the fibres. The fibre stripping improves the bond strength compared to the already high standard of the reference process. The increase of the roughness and surface area is seen as the driving mechanism behind the further improvement. Opposed to the reference process, laser treatment is additionally capable of removing contaminations. The removal of contaminations is a considerable advantage of laser treatment, given the severe risk that is posed by contaminations. Though no clear evidence of a functionalisation was found, the chemical composition shows a high functionality without any contaminations and is therefore suitable for adhesive bonding. The main downside of the process is the physically induced interaction between the epoxy resin matrix and the N-IR laser and the consequential formation of cavities under matrix-rich areas. The cavities, though comparably small, can only be partially filled and could induce failure in the bond.

Nevertheless, for all tested scarf ratios and lay-ups, an increase of the bond strength compared to the reference process was achieved. This shows the high potential of N-IR laser treatment for composite repair applications.

VIII

Content

List of abbreviations

AC	Acetone rinsing
ANOVA	Analysis of variance
AR	As received
BET	Brunauer-Emmet-Teller
CFRP	Carbon fibre reinforced polymer
FE	Finite element
HAZ	Heat affected zone
IPA	Isopropyl alcohol
LMWOM	Low molecular weight oxidized material
LPX	Laser parameter
MEK	Methyl ethyl ketone
M-IR	Mid-infrared
N-IR	Near-infrared
OWRK	Owens-Wendt-Rabel-Kaelble
PAN	Polyacrylonitrile
QI	Quasi-isotropic
RA	Release agent
SC	Solvent cleaning
SFE	Surface free energy
TSA	Total surface area
UD	Unidirectional
UT	Untreated
UV	Ultraviolet

XIV

1   Introduction

Nowadays, composites and especially carbon fibre reinforced polymers (CFRP), are a common material for aircraft structures. The newer aircraft generations like the Airbus A350 XWB or the Boeing 787 consist of 53 and 51 per cent by weight from composites [1]. During their lifetime, aircraft structures can be subject to damages. Collected data from Airbus of over 30 million flight hours revealed that a majority of the damages result from impacts to the fuselage. For the Airbus A350 XWB and the Boeing 787, the fuselage consists of CFRP to a significant part. Sources for damages are numerous but mostly involve ground handling. While commercial aircraft follow a damage tolerance approach that ensures operation after accidental damage, a repair is necessary to maintain aircraft safety [2]. Following the presence of damages that need to be repaired and the increasing use of CFRP in aircraft structures, there is a demand for suitable repair solutions.

Composites can be repaired by either bolting, bonding or a combination of both methods [3]. Bolted joints are easy to assess and have multiple load paths, which is a significant advantage of this joining technique. On the other hand, the safety factor and therefore, the weight needs to be increased because holes in the structure introduce stress concentrations [4,5]. Bonded repairs offer the advantage of a more evenly distributed load, but are difficult to assess, and performance is highly dependent on the quality of the manual work. Therefore, in the last years, considerable effort has been taken to automise the bonded repair process and increase reliability.

In several projects milling tools and robots were designed to substitute the manual grinding process and make an on-site repair possible (e.g. CAIRE repair robot from Lufthansa Technik or ULTRASONIC mobileBLOCK from DMG Mori, see Figure 1.1) [6,7]. While solutions for the automated removal of the damaged material exist, the necessary subsequent surface treatment relies on manual solvent cleaning so far. Generally, surface treatment is a

critical step during the adhesive bonding process, which can greatly influence the performance of the joint. Several surface treatment methods like chemical, plasma and laser surface treatment exist [8,9]. Recently, laser surface treatment of CFRP has received major interest as it offers low wear and short process times. For the laser surface treatment of CFRP, classification by the wavelength is the most reasonable as it determines the absorption behaviour of the constituents. Laser in the near-infrared laser (N-IR) range offer high efficiency, are comparably cheap and can be guided by optical fibres, making them suitable for automation purposes. The low absorbance of N-IR laser in the epoxy resin of the CFRP matrix, on the other hand, makes the process itself, as well as the assessment challenging [10].
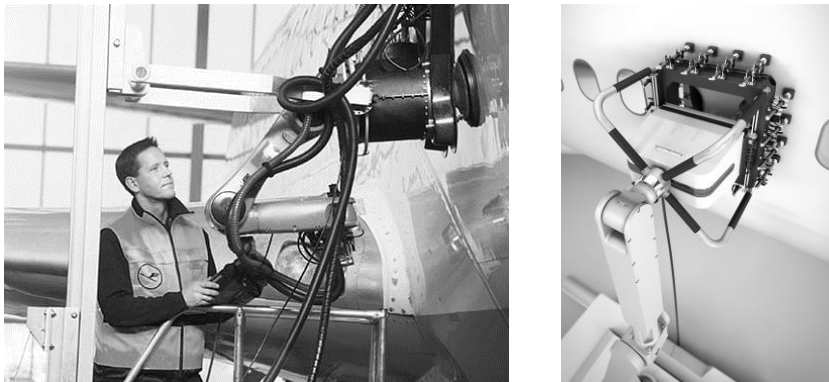
Figure 1.1: Left: CAIRE repair robot from Lufthansa Technik, Right: ULTRASONIC mobileBLOCK composite repair milling robot from DMG Mori [6,7].

1.1 Aims and scope

This work aims to investigate the effects of N-IR surface treatment on the adhesive properties of milled CFRP. Adhesive bonding involves multidisciplinary knowledge about surface chemistry, polymers, mechanics and other scientific fields. Keeping also in mind that several adhesion theories exist (e.g. mechanical interlocking and chemical bonding) extensive knowledge of the surface is necessary [11].

Therefore, the first part involves the detailed characterisation of the surface with several advanced analysis methods. In the characterisation, the surface morphology is analysed on different scales with light microscopy and scanning electron microscopy, both also involving the preparation of cross-sectional views. The analysis of the morphology is accompanied by roughness measurements that give a quantitative measure of the surface. This part aims to investigate the effect of the N-IR surface treatment on the morphology. Since heat is introduced into the surface, special attention is given to potentially damaging effects. Consequently, also the effect in the thickness direction is examined. Furthermore, the surface chemistry is analysed by XPS. Here, the CFRP, as well as the carbon fibre, are measured to achieve an independent view of the processes during the laser surface treatment and to evaluate a functionalisation of the surface. Finally, the wetting behaviour is investigated. The wetting behaviour is influenced by the morphology, as well as the chemistry and is an important measure for the adhesive properties of a surface.

In the second part, the resulting mechanical properties of the adhesive bonds are evaluated. For the mechanical characterization, materials and processes from the aerospace industry are adopted as these parameters can have a significant impact on the outcome. Only aerospace certified materials are used, and the curing process emulates an out-of-autoclave on-site repair. From the composite repair geometry, the scarf bonded joint can be derived. Therefore, the scarf bonded joint is the preferred geometry for mechanical testing on the laboratory scale. Different scarf angles and lay-ups are tested

under static and fatigue load to account for different loading conditions. Furthermore, the ability to remove contaminations is investigated to evaluate the process robustness.

In the final part, the surface properties and resulting adhesive properties are discussed to create guidelines for the bonded repair approach with N-IR laser surface treatment. Consequently, this work contributes to efficient aircraft structures with suitable composite repair methods.

4

2 Literature survey

2.1 Scarf bonded joints for composite repair

Bonded composite repairs are usually performed by circularly removing material in the damaged zone and thereby creating a scarf. The scarf increases the bonding surface and creates a uniform load transfer to the repair patch that is applied afterwards. The uniform load transfer makes the scarf repair more weight-efficient than a bonded overlap repair and therefore, the chosen technique for composite repairs [12,13]. As the manufacturing of composite repairs is expensive for research purposes, most studies use the simplified scarf bonded joint for mechanical testing. The derivation of the scarf bonded joint from the composite scarf repair is shown in Figure 2.1. For further simplification, the specimen geometry can be reduced to one bond line.
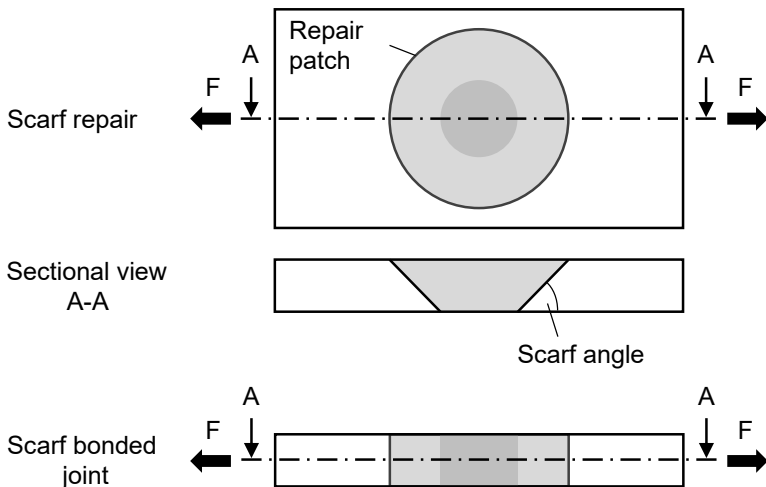
Figure 2.1: Scarf repair and the derived scarf bonded joint geometry. The sectional view A-A applies for both geometries (own illustration according to [14]).

Two main differences can be observed: First, for scarf bonded joints, only the direction with the highest load is considered [15]. Second, the load can only be transferred through the joint. An alternative path through pristine material, as it is the case in composite scarf repairs, is not possible. A numerical model showed that a two-dimensional scarf bonded joint underestimated the strength by more than 40 % compared to a three-dimensional composite scarf repair [16]. Therefore, the scarf joint is considered to show a conservative estimation of the behaviour in industrial applications [17].

2.1.1 Stress distribution and failure

The scarf bonded joint can be primarily characterised by the scarf ratio that is given by the thickness of the laminate and the projected length of the scarf or the scarf angle α. Scarf ratios usually range from 1:40 (α = 1.4°) for a shallow scarf bond up to 1:5 (α = 11.3°) for a steep scarf bond. Shallow scarf ratios result in an exponential increase of the failure load as the surface for bonding is increased, and the peel stress ratio is decreased [18–21]. This effect is even more pronounced in cycle fatigue tests, where shallow scarf ratios show significantly better performance [22]. On the other hand, in an aerospace application, the repair area is often restricted due to the proximity to e.g. doors, making steep scarf ratios necessary. Additionally, shallower scarf angles are more difficult to machine and are prone to adherend tip bluntness [18,23].

The stress distribution along the bondline depends on the scarf ratio and lay-up of the adherends. For lay-ups with multiple fibre directions, peel and shear stress peaks can be observed in the vicinity of the stiffest plies [24]. This is a major difference compared to other bonding types like the single-lap joint, where only one ply orientation is in contact with the adhesive [25]. For quasi-isotropic (QI) laminates, strain and stress peaks were observed close to the 0°-ply in finite element (FE) simulations and digital image correlation inspections [26,27]. For unidirectional (UD) lay-ups, the stress distribution is similar to adherends from isotropic materials. Here, peel and

shear stress peaks, as well as strain peaks, can be found at the scarf endings [26,27].

Similarly, the failure is dependent on the scarf ratio and lay-up of the adherends. For QI lay-ups the failure initiates in the 90°-ply because it has the lowest strength of all plies and then propagates through the bondline [14,15,26]. For smaller scarf angles the amount of adherend failure further increases [16,22]. For UD lay-ups, the failure initiates at the scarf endings in the region of the stress peaks and propagates through the bondline [26]. Only for very shallow scarf angles ($\alpha = 0.5°$), the failure changes to adherend failure [23]. Consequently, the material and lay-up specific joint failure can be adjusted by the scarf ratio [16].

2.1.2 Hard- and soft-patch approach

Scarf bonds can be produced by either a hard- or a soft-patch. For the hard-patch approach, a pre-cured repair patch is bonded in a secondary bonding process. The dimensional accuracy of the repair patch is critical as it determines the bondline thickness. The bondline thickness, on the other hand, is critical for the strength of the joint. A thickness between 0.15 and 0.25 mm was found to be ideal for scarf joints with brittle adhesives like epoxy resin [28]. For the soft-patch approach, the repair patch is cured together with the adhesive in a co-bonding process. In that case, a carrier inside the film adhesive controls the bondline thickness. A study comparing the strength of hard- and soft-patch repairs found similar results for both methods with slightly better performance of the soft-patch repair [29].

2.2 Milling of CFRP

The first step of a scarf bond repair process is to remove the damaged material. In an automated repair approach, this is done by end milling. For further processing by laser treatment, it is therefore essential to characterise the existing surface after milling.

While milling of CFRP has been extensively investigated in the literature, most studies focused on the edge trimming. This is due to the fact that CFRP parts are produced near net shape, and edge trimming is often necessary to achieve the final shape of the part [30]. Edge trimming differs from end milling in terms of engagement conditions. In edge trimming, the material is removed in-plane, whereas in end milling it is mainly removed in the thickness direction perpendicular to the laminate plane as shown in Figure 2.2 [31,32].

a_p = axial depth of cut

a_e = radial depth of cut

a_e = radial depth of cut

a_p = workpiece thickness

End Milling
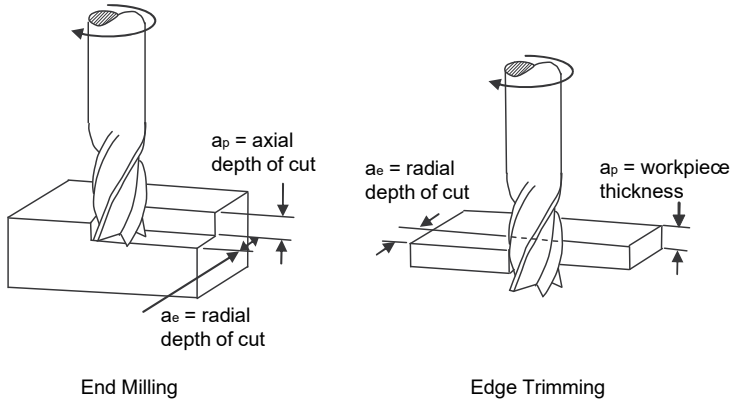
Edge Trimming

Figure 2.2: Comparison of the engagement conditions of end milling and edge trimming [31].

Still, for the characterisation of the surface after the milling process, some general information can be derived. Several studies found that the surface quality, fracture mechanisms and chip formation depends on the fibre cutting angle [33–43]. For the fibre cutting angles relevant for repair applications ($\theta \approx 0\,°$), they found that fibre-matrix debonding and compression-induced fibre fractures are the main fracture mechanisms [33–35]. Fibre-matrix debonding resulted in a large number of fibres being exposed [34,36]. The exposed fibres show fracture surfaces that are rough and perpendicular to the fibre direction [35,38,41]. Additionally, cavities were detected after milling, indicating that the surface could be weakened [33,35,38].

8

The surface roughness is an essential parameter for the surface quality and has been investigated by some authors. Arithmetic average roughnesses (Ra) between 0.8 and 1.3 µm have been reported [34,35,41]. This value is low compared to the theoretical surface roughness between 2.5 and 6.0 µm when assuming a hexagonal arrangement and a diameter of 5 µm [32]. Hence, it was assumed that the surface roughness is influenced by abrasive microparticles that smoothen the surface [34]. These microparticles are residues that originate from a series of fractures during the milling process and are usually between 0.25 and 2 µm in diameter [38,44,45].

Although some of these results date back to investigations by Koplev et al. from 1983 [38], there has been relatively little literature published on the effect of end milling and the resulting surface characteristics on the adhesive bond strength of CFRP. Reisgen et al. and de Freese et al. both reported that a higher surface roughness correlates with improved adhesive bond strength [46,47]. Reisgen et al. produced different surface roughnesses by varying the milling parameters. Whereas they assumed a relationship between the surface roughness and the smoothening effect by microparticles, no evidence for the relationship was shown. Furthermore, no method for the removal of these particles was presented [46].
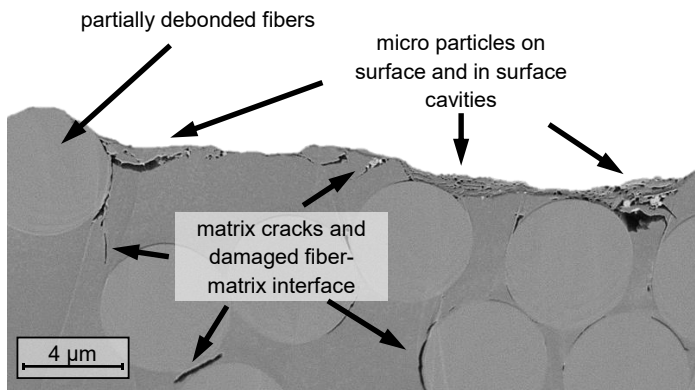
Figure 2.3: SEM image of a CFRP cross-section after milling and manual cleaning with a lab wipe and acetone [46].

The study by de Freese et al. was the first to systematically investigate the effect of milling microparticles and the cleaning method on the adhesive bond strength. They found that microparticles are present despite a manual cleaning with lab wipes in combination with acetone as can be seen in Figure 2.3. While other defects were also present on the milled surface, the authors concluded that microparticles were the main limiting factor on the adhesive bond strength. Additionally, the authors showed that with ultrasonic cleaning, they were able to remove microparticles, increase the surface roughness and consequently improve the bond strength [46]. Except for the study by de Freese et al. [46], no research about further treatment of milled CFRP surfaces has been published. Given the fact that milling is an essential step in an automated CFRP repair approach, additional research about the characteristics of milled surfaces and cleaning methods are necessary.

2.3   Laser beam and CFRP surface interaction

Laser beam and CFRP surface interaction can be differentiated by the wavelength of the laser. The energy of the photons is inverse to the wavelength. In order to break the covalent bonds between the carbon atoms in a polymer and achieve ablation through the photochemical effect, wavelengths below 250 nm are necessary. This is the range of ultraviolet (UV) laser sources. For higher wavelengths, that include near-infrared (N-IR) and mid-infrared (M-IR) laser sources, the material is heated through excitation, which causes the photothermal effect. Additionally, the absorption behaviour of the constituents is essential for the process [48]. Figure 2.4 shows the absorption behaviour of epoxy resin for different laser sources that are typically used for industrial applications. The absorption behaviour shows a strong dependence of the wavelength with an absorption rate of around 90 to 95 % for UV and M-IR laser sources and almost 0 % for N-IR laser sources [10]. The absorption behaviour has further implications for the effect of material removal as the carbon fibre has a high absorption over the complete wavelength spectrum. Consequently, for the N-IR laser, the material is removed through the heating of the fibre and subsequent

sublimation of the epoxy resin [49]. This is illustrated in Figure 2.5, where the direct- and indirect-induced ablation is compared for a CFRP surface.
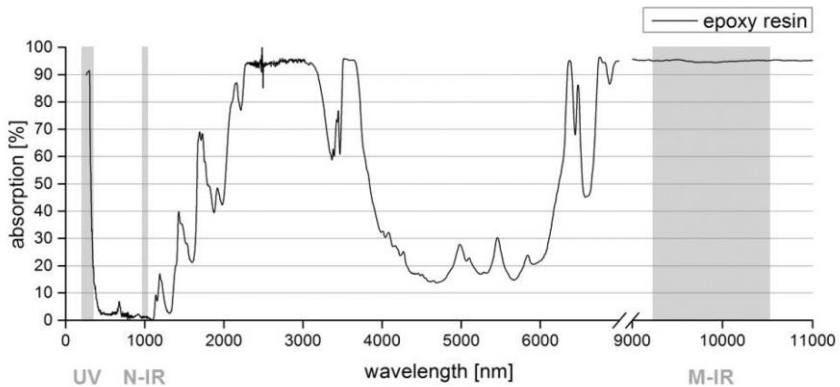
Figure 2.4: Absorption behaviour of epoxy resin. The typical laser source ranges ultraviolet (UV), near-infrared (N-IR), and medium-infrared (M-IR) are indicated [10].
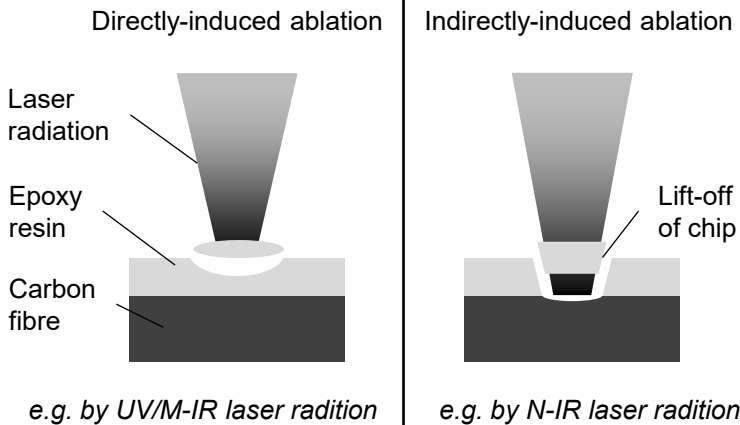
Figure 2.5: Comparison between the directly- and indirectly-induced ablation of epoxy resin on a CFRP surface (own illustration according to [49]).

The following subsections describe the interaction between typically used laser types and the CFRP surface in more detail while focussing on the N-IR laser that is used for the experiments in this work.

2.3.1 UV laser

UV laser systems are characterized by the high absorption of the epoxy and ablation that is dominated by the photochemical effect. This is achieved by high photon energy that is able to break chemical bonds in the epoxy matrix and carbon fibres as well [50,51]. Direct targeting of the epoxy matrix is possible, making the stripping of fibres very effective. As the ablation is dominated by the photochemical effect, the heat-affected zone (HAZ) was found to be less than one-third of the HAZ induced by an N-IR laser in CFRP cutting experiments [52]. Since even UV laser systems cannot eliminate the presence of a HAZ, it is expected that photothermal effects also have an influence during UV laser treatment. This is especially the case for processes with higher laser fluences [53].

2.3.2 N-IR laser

N-IR laser systems have a very low absorbance in epoxy resin, and as a result, the epoxy matrix can only be removed by the heating of the fibre [49]. The resulting process is characterized by the significant difference in thermal conductivity, sublimation temperature and the latent heat released through the sublimation of the respective material between the constituents as seen in Table 2.1 [54]. The laser process involves the interaction between laser and materials, chemical reactions, combustion phenomena, and so on. Furthermore, the process takes place on different scales with large temperature gradients in short periods [49,55]. This makes the assessment of the laser process difficult. So far, no study was able to determine the temperature during the laser pulse experimentally. Ohkubo et al. investigated the interaction between CFRP and the laser pulse on a micro-scale with a numerical model and published three separate studies [54–56]. The authors found that combustion plays a significant role during the

ablation process [54]. The combustion is accompanied by an ablation plume that can reach temperatures from 3000 to 7000 K, while the temperature in the material reaches values of 500 to 1000 K [55,56].

Table 2.1: Thermo-physical properties of the CFRP constituents [57–59] (as cited in [54]).

	Carbon fibre	Epoxy resin
Density in g/cm^3	1.85	1.25
Thermal conductivity in W/(m·K)	∥: 50, ⊥: 5	0.2
Heat capacity in J/(kg·K)	710	1200
Sublimation temperature in K	3900	800
Latent heat in kJ/kg	43,000	1000

Experimental investigations usually focused on the microscopic evaluation of the surface with varying fluence, which is defined as the optical energy per unit area, and intensity [10,49,60]. Three threshold levels depending on the material were identified experimentally by Blass et al. [10]. At low intensities, no ablation of the CFRP is detectable, though the material shows an optical change. With an increase of the intensity, the epoxy resin is ablated while the fibre remains visibly intact. With a further increase of the intensity, the epoxy resin, as well as the carbon fibre, are ablated, and some of the fibres are completely cut through. The intensity level for the removal of the epoxy resin also depends on the thickness of the top resin layer with thinner layers needing less intensity [10]. Similarly, Pagano et al. [60] defined six quality levels ranging from stripped and undamaged fibres to severely damaged and scattered fibres. It was therefore concluded that the level of stripping could be adjusted by the laser parameter [60].

2.3.3 M-IR laser

Though M-IR lasers show a high absorbance in epoxy resin, the photon energy is not sufficient to break chemical bonds. The absorbance of multiple photons is only possible in an experimental setup, and therefore only photothermal effects can be expected using an M-IR laser for epoxy resin ablation. Experiments with epoxy resin coatings showed a decrease in oxygen and oxygen-containing groups, indicating that deactivation took place [61]. Carbon fibre ablation is also possible with an M-IR laser source, though the HAZ was found to be larger than for an N-IR laser [62].

2.4   Surface treatment for adhesive bonding of CFRP

This section provides an overview of methods that are used to improve the adhesive bond properties of CFRP. While plenty of methods are described in the literature, this section focuses on methods that could potentially be embedded into an aircraft structural repair. So for instance, peel-plies are not further explained, because they need to be applied during the manufacturing of the part and so is low-pressure plasma treatment, because a vacuum chamber is necessary making an on-site repair practically impossible. Furthermore, a majority of the studies focus on surface treatment during manufacturing. After manufacturing the surface is covered by a smooth layer of epoxy resin. Additionally, a release agent from the mould is often present [63]. This is in contrast to the repair process where parts of the fibres are exposed, the roughness is increased, and microparticles are present due to the removal of the damage (see also Chapter 2.2). Nevertheless, mechanisms and characteristics from the manufactured surface can also be transferred to the surface after milling. As publications dealing with the surface treatment after the damage removal are rare, this section mainly includes publications about the surface treatment during the manufacturing process. Literature that deals explicitly with the surface treatment after damage removal will be pointed out in the text.

2.4.1 Overview of different surface treatment methods

Grit blasting, grinding and milling

While mechanical surface treatments like grit blasting, grinding and especially milling (as presented in Chapter 2.2) are suitable methods to remove large amounts of material, they can also be seen as a surface treatment method. Together with solvent cleaning, it is the default method and is therefore included as a reference in many publications that investigate surface treatment methods mentioned further in this section. In the process of material removal, polymer chains are broken, producing a reactive surface [8]. The resulting surface shows an increase in oxygen as well as roughness compared to an untreated or solvent cleaned surface [8,64–67]. Moreover, existing fluorine contamination can be wholly or partly removed according to several studies [8,64,68,69]. The increase of roughness and oxygen, as well as the removal of contaminations, contributed to the improved wetting that was observed in contact angle measurements [64,66–68]. Compared to untreated configurations, where often a release agent from the production process is present, the bonded joint strength could be improved [70,71]. The damaging of fibres can be seen as one of the downsides of mechanical abrasion techniques. Furthermore, the formation of microparticles often makes a subsequent cleaning of the surface necessary [71].

Solvent cleaning

Solvent cleaning is the default surface treatment method of CFRP before bonding and is also recommended by the SAE International in the aerospace standard "Masking and Cleaning of Epoxy and Polyester Matrix Thermosetting Composite Materials". Several cleaning agents like methyl ethyl ketone (MEK), acetone or the less hazardous isopropyl alcohol (IPA) are suggested [72]. The main goal of solvent cleaning is the removal of contaminations. The ability to remove contaminations, in turn, depends on the cleaning agent and the contamination type itself [48]. As a result, some

authors report that solvent cleaning was able to remove contaminations [73], while others report insufficient cleaning performance [64]. Likewise, the contamination can dissolve and spread across the surface and even diminish the adhesive strength [8]. The surface morphology remains mostly unaffected by the solvent cleaning process. Still, microparticles can partly be removed, and solvent cleaning is, therefore, often used as a second step after mechanical abrasion processes [23,46,70,74–79] or plasma treatment [80]. Despite the contamination removal, no significant shift of the chemical composition has been reported and hence, no functionalisation can be expected [64].

Atmospheric pressure plasma treatment

The primary purpose of plasma treatment is the introduction of functional groups to the surface. These functional groups improve the adhesion by providing a reactive surface for the adhesive [8,25]. A significant increase in oxygen and oxygen-containing functional groups has been reported in several studies [64,68,81–85]. Deconvolution of the carbon peaks from XPS measurements showed an increase of carboxyl groups (-COOH) in particular [67,85]. The increase of carboxyl groups could be directly correlated to an increase of the lap shear strength in one case [67]. Some authors also reported an increase of nitrogen on the surface, indicating that both oxygen and nitrogen, could contribute to the functionalisation of the surface [67,83]. As a result of the functionalisation, an improved wetting behaviour with increased surface energy was measured in contact angle measurements [64,67,75,82–85]. The change of surface energy was remarkably dominant for the polar part [67,75]. For the surface roughness, no significant change could be observed, though some studies reported a surface ablation on a nanoscale with increased exposure time [64,67,85]. In general, the ability to remove material when heat introduction needs to be considered is limited to less than 50 nm [8]. As a result, the removal of contaminations is also limited. Though the amount of release agent could be decreased, even for longer exposure times, a significant ratio remained on the surface [64,82]. In order

to remove contaminations and functionalize the surface, a combined approach where the surface was mechanically abraded or solvent cleaned in a first step and plasma treated in a second step was used in some studies [8,64,82]. For clean surfaces, the adhesive strength could be improved further and a cohesive failure was observed [64,75,81–83,86].

2.4.2 Laser surface treatment with a UV laser

UV laser surface treatment of CFRP has been widely used because of the efficient removal of epoxy resin as discussed in Chapter 2.3.1. The direct removal of epoxy resin reduces the degradation of the surrounding material [87]. The surface treatment strategies can be mainly divided by the ablation depth: While the first group aims to remove a layer of epoxy resin only [63,70,88,89], the other group aims to remove a more significant amount of epoxy resin in order to strip the fibres [90,91]. Both strategies have in common that the removal of contaminations like release agent is essential for successful surface treatment. The surface cleaning effect of a UV laser has been reported by several authors [65,87,89,91]. This effect has been accompanied by a reduction of fluorine, chlorine and silicone on the surface as these elements are often used in release agents [65,87]. Overall, most publications saw a positive effect of the UV laser surface treatment on the surface chemistry with an increase of oxygen and nitrogen on the surface [65,87,89,92]. It was hypothesised that the UV laser treatment induced free carbon radical through chain scission that would react with ionised gases near the surface and created oxygen and nitrogen-containing functional groups [89]. In some cases, also an increased surface roughness was reported [65,90]. As a consequence, the wetting behaviour improved [65,87]. Because direct targeting of the epoxy resin is possible with a UV laser, a pattern on the surface could be produced without damaging the fibre [93]. Finally, for optimized parameter sets the bonded joint strength could be improved in single-lap-shear tests compared to untreated, solvent cleaned, and ground configurations [63,65,73,87,91,92,94]. However, for some parameter sets and material combinations, the adhesive strength

decreased compared to solvent cleaned and especially ground surfaces [70,73,89]. Here, in some cases, a weakening of the CFRP is observed [70,73]. This result emphasises the importance of the laser parameter selection and an adjustment to the material to be treated.

2.4.3 Laser surface treatment with an N-IR laser

Keeping the characteristically low absorbance of N-IR laser radiation in epoxy resin in mind, a complete stripping of the carbon fibres is necessary to avoid cavities at the surface. Several studies showed that the stripping of the fibres is possible with an N-IR laser. This could be achieved with UD laminate [73,95] as well as fabric laminate [96,97] that has more resin-rich areas. It was hypothesised that the stripping of the fibres benefits the interlocking between the CFRP surface and the adhesive [98]. On the other hand, the formation of cavities in the topmost carbon fibre layer has been reported by some authors, as seen in Figure 2.6 [70,73]. It was assumed that this was caused by the high transmission coefficient of the matrix. Most of the energy is absorbed by the fibre. While the energy in some cases was enough to cause a fibre-matrix debonding, the resulting heat was not able to sublimate the matrix leaving cavities near the surface as a result [73]. The stripping of the fibres is usually accompanied by a narrowing of the fibres. It was therefore concluded that the temperature must reach 400 °C and more during the process as this is the temperature at which the fibre begins to oxidize [73]. Some authors concluded that functionalization of the fibre takes place during the oxidation that improves the adhesive properties [73,97]. In contrast, Sun et al. published XPS results where the oxygen and nitrogen content decreased after N-IR laser surface treatment [98]. Still, the lap shear strength could be improved compared to an untreated configuration as the fibres were stripped, which was accompanied by a removal of a release agent layer [98]. Likewise, the wetting behaviour improved after N-IR laser treatment, and some authors even reported a complete wetting [70,99].
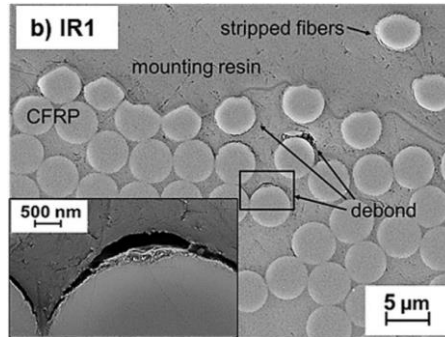
Figure 2.6: Debonding and formation of cavities after N-IR laser surface treatment [73].

The only publication investigating the N-IR laser surface treatment of a scarfed surface was published in 2014 by Schmutzler et al. [97]. Here, a warp and weft fabric was used in a QI layup. The specimens were repaired with an approximate scarfing ratio of 1:25 using sand paper. Four different laser parameter configurations were tested. It could be shown that one laser parameter could fully recover the strength of the QI laminate. The standard repair was able to recover around 87 % of the quasi-isotropic laminate strength. The improvement in static strength was 15 % compared to a standard repair. The three other laser parameter performed similar or worse compared to the standard repair. The investigation showed that it is possible to increase the strength of scarfed CFRP repairs by laser surface treatment. The study also demonstrated that the selection of the laser parameter is critical as only one parameter set was able to improve the performance compared to a standard repair. The improved strength was attributed to the fibre stripping that could be seen in SEM. Additionally, it was assumed that the laser treatment results in oxidation of the fibres, which also improves the adhesion between fibre and adhesive.

Though the presence of cavities appears to be consequential, so far, no detailed study on the presence and size has been published. Additionally, it was not investigated, whether the cavities can be filled and thus further

contribute to the interlocking. Despite the unfavourable N-IR laser-surface interaction, several authors reported an improvement of the bonded joint strength. This leads to the conclusion that with proper parameter selection, an improvement of the adhesion properties is possible. The fact that a prior mechanical abrasion exposes large parts of the carbon fibres in a repair process should further benefit the N-IR laser characteristics.

2.4.4 Laser surface treatment with an M-IR laser

With M-IR laser surface treatment, a directly-induced ablation of epoxy resin is possible. The degree of the fibre stripping can be adjusted by the treatment speed, pulse energy and pulse frequency [100]. With the given laser characteristic, some studies experimented with surface structuring and patterning to increase the surface and improve the adhesive strength [101,102]. The removal of contaminations appears to be the main strength increasing effect of the M-IR surface treatment which was demonstrated in some studies [71,100]. A functionalisation of the surface was shown to be unlikely. As a decrease of oxygen and hydroxyl functional groups was detected, a deactivation of the surface was observed [61].

2.5   Carbon fibre and epoxy matrix adhesion

During the milling of CFRP, the surface is stripped, and therefore the adhesion between the fibre and the adhesive is important for the mechanical properties of the bond. As the adhesives that are used for the repair of CFRP in aerospace are epoxy based resins, the problem is very similar to the fibre-matrix adhesion. Carbon fibre and epoxy matrix adhesion has been one of the main topics in composite research since many years and comprehensive literature can be found on that topic, e.g. in [103–106]. This chapter aims to give a brief overview.

2.5.1 Structure and morphology

The majority of commercially available carbon fibres are obtained in a multi-step process involving the spinning, stabilization and carbonization of a polyacrylonitrile (PAN) precursor. The resulting carbon fibre consists of aromatic carbon layers with covalent bonds aligned in the fibre direction. The layers form ribbons that run through the complete length of the carbon fibre. Parallel to the primary direction, weaker van der Waals forces act resulting in the characteristic anisotropic mechanical, electrical and thermal behavior of the carbon fibre [104]. Commercial carbon fibres are available in varying diameters between 5 and 10 μm [107]. The resulting theoretical surface area for a cylindrical fibre shape and a density of 1.85 g/cm^3 lies between 0.2 and 0.4 m^2/g. Brunauer-Emmet-Teller (BET) surface area analysis revealed that the measured total surface areas (TSA) were significantly larger than the theoretical value for carbon fibres. It was shown that the TSA could be increased from 0.4 up to 2 m^2/g by oxidation in air under elevated temperatures [108]. In another study, a TSA of up to 1500 m^2/g was achieved by oxidation with oxygen gas mixtures [109]. The deviation of the TSA from theoretical values indicates that the surface is rough and contains mesopores with diameters between 2 and 50 nm [110]. Furthermore, it was hypothesized that an increased roughness could benefit the fibre-matrix adhesion through mechanical interlocking [104].

2.5.2 Surface chemistry

The surface of carbon fibres mainly consists of carbon, oxygen and for PAN-based fibres also a considerable amount of nitrogen [104,111]. An increased oxygen and nitrogen content is associated with an increase of functional groups that naturally benefits the adhesion to epoxy resin [112–115]. Consequently, the oxygen content can range from 2 % for untreated up to 20 % for oxidised fibres [104,112]. The nitrogen content on the other hand, is significantly lower and ranges from 0 to 3 % [111,116]. Figure 2.7

illustrates different oxygen and nitrogen containing functional groups on carbon.
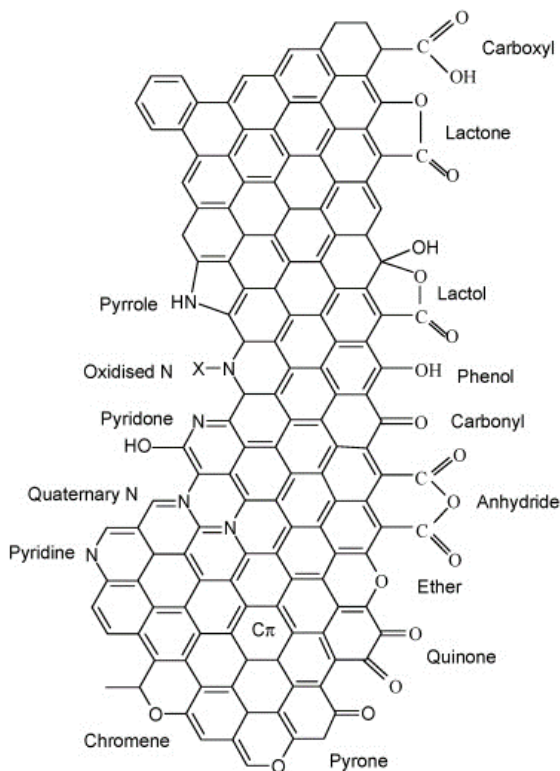
Figure 2.7: Nitrogen and oxygen containing functional groups on carbon [117].

While various functional groups can be present on the surface, most of the studies focus on hydroxyl (-OH, phenol contains a hydroxyl group in Figure 2.7), carboxyl (-COOH) and ester (-COOR, lactones in Figure 2.7 are a type of ester) groups. Several authors reported that carboxyl, ester and amide functional groups are of special importance for the interfacial shear strength, which is a characteristical parameter for the fibre-matrix adhesion [112,113]. The carboxyl group can react with the epoxy groups, the amine

22

groups and the hydroxyl groups of the matrix and is highly reactive [112,113,115]. Therefore, the aim of most fibre surface treatments is to introduce functional groups.

2.5.3 Surface treatment

Fibre surface treatments aim to improve the adhesive properties of the surface. The different fibre surface treatments can be categorized into dry gaseous oxidation, wet oxidation, electrochemical oxidation and plasma treatment [103]. Dry gaseous oxidation uses an oxidizing gas at elevated temperatures in order to burn away surface layers and create active sites [103]. Oxidation with oxygen-containing gases under 500 to 700 °C produced promising results [109]. On the other hand, a degradation through burned-off material can weaken the fibre and therefore, process parameters have to be chosen carefully [118,119]. For wet oxidation, the fibres are treated in e.g. nitric acid. Wet oxidation is comparably time consuming and therefore rarely used in industrial processes [103]. The electrochemical oxidation on the other hand, is generally used for the surface treatment of commercially used carbon fibres as it is fast and produces a uniform surface [120]. Electrochemical oxidation is a continuous process where the fibres are immersed in an electrolyte like sodium hydroxide under a current. After the process, the fibres are washed to remove excessive electrolyte [120]. Finally, plasma treatment is a method that showed promising results in terms of the introduction of functional groups, but so far lacks industrial application [121].

2.5.4 Sizing

After the surface treatment of the carbon fibre, a sizing is applied to the surface. The role of the sizing is to protect the fibre during handling and furthermore improve the adhesion [105]. Generally, the sizing is an epoxy based solution, but detailed information is hardly available. The sizing contributes around 0.5 to 1 % by weight or 0.03 to 0.5 µm by thickness to the fibre [104]. As for the surface treatment, the choice of the sizing type is

essential for the mechanical properties of the composite [122]. Studies found that sized fibres are characteristic for low nitrogen content and a high concentration of C-OR type functional groups [116,123,124].

3 Manufacturing procedures

From the literature review, it could be concluded that the laser parameters are very much dependent on the material and surface properties at hand. The material and manufacturing processes involved were therefore closely matched to aerospace standards.

3.1 Materials

3.1.1 CFRP prepreg

Two different prepreg systems were used. The primary laminate HexPly M21/34%/UD194/T800S from Hexcel Corporation (Stamford, United States) consists of an M21 epoxy resin matrix and a T800S carbon fibre. The prepreg system has a cured ply thickness of 190 μm. It is used for the manufacturing of the Airbus A380 and in a modified version also for the Airbus A350 XWB [125].

Table 3.1: Fundamental mechanical properties of the prepreg materials in fibre direction [126,127].

	Primary laminate M21/34%/UD194/T800S	Repair laminate M20/34%/UD194/IM7
Tensile strength in MPa	2970	2600
Modulus in GPa	165	163
ILSS[1] in MPa	102	90

[1]ILSS: Interlaminar shear strength

The repair laminate Hexply M20/34%/UD194/IM7 also from Hexcel Corporation consists of an M20 epoxy resin matrix and an IM7 carbon fibre. The M20 epoxy resin system was developed for composite repair

applications and is qualified by the Commercial Aircraft Composite Repair Committee (CACRC), Boeing and Airbus [128].

Fundamental mechanical properties in the fibre direction of both prepreg systems are summarised in Table 2.1. The primary laminate material shows a slightly better performance in terms of tensile strength, modulus and ILSS. Both prepreg systems have a fibre volume content of 58 % [126,127].

3.1.2 Epoxy adhesive film

FM300-2M.06PSF from Solvay (Brussels, Belgium) was used as an adhesive system. The epoxy resin film adhesive includes a carrier film from randomly oriented polyamide fibres that control the bond line thickness. The adhesive has a single lap shear strength of 40.7 MPa (according to ASTM 1002 at 24 °C with aluminium adherends) [129].

3.1.3 Carbon fibre roving

For the experiments with fibre rovings, T700S carbon fibres from Toray Industries (Tokyo, Japan) were used as the T800S carbon fibres from the primary laminate were not commercially available. The carbon fibres have a diameter of 7 µm and are delivered on a spool with a 12K tow. T700S have a larger diameter (5 µm for T800S fibres), lower modulus (294 GPa vs 230 GPa) and strength (5880 MPa vs 4900 MPa) compared to T800S carbon fibres [130,131].

3.2   Prepreg autoclave process

This chapter consists of the manufacturing of the primary laminate plate and the repair patch in an autoclave process. Several other manufacturing steps chronologically separate both autoclave processes. These manufacturing steps are described in the following chapters. For a better understanding, the chronological sequence between both autoclave processes is shown in Figure 3.1.
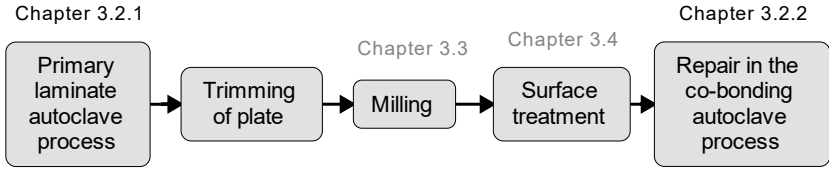
Figure 3.1: Process diagram of the autoclave processes and steps in between.

3.2.1 Primary laminate autoclave process

The primary laminate was manufactured in an autoclave according to the guidelines provided by the manufacturer. Curing was done at 180 °C for 2 h. The relative pressure in the oven was 7 bar and -0.25 bar in the vacuum bag.
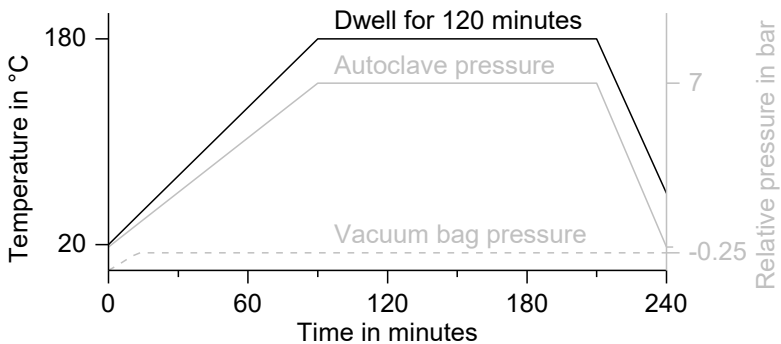
Figure 3.2: Curing process for the primary laminate HexPly M21/34%/UD194/T800S from Hexcel.

Two different lay-ups were produced:

- A Unidirectional (**UD**) lay-up with the stacking sequence $[0°]_8$. The UD lay-up was used to minimize adherend failure and increase the effect of the surface treatment method.
- Quasi-isotropic (**QI**) lay-up with the stacking sequence $[45°/0°/-45°/90°]_s$. The QI lay-up contains all fibre orientations used for primary load-bearing composite aircraft structures. The

precise ratio of the orientations (50 % of 0°, 37.5 % of 45° and 12.5 % of 90° according to [14]) is not matched since this would significantly increase the thickness of the laminate and consequently the milling costs.

Both lay-ups resulted in a cured laminate thickness of 1.5 mm. The primary laminate plate was trimmed and then milled in the next step (see Chapter 3.3).

3.2.2 Repair in the co-bonding autoclave process

The repair laminate was cured together with the film adhesive under ambient pressure in a co-bonding process. In this way, an out-of-autoclave repair process was supposed to be emulated. The relative pressure in the vacuum bag was -0.95 bar. Two temperature dwells, 100 °C for 3 h and 140 °C for 2 h, were applied. The lay-up of the primary laminate was matched by the repair laminate.
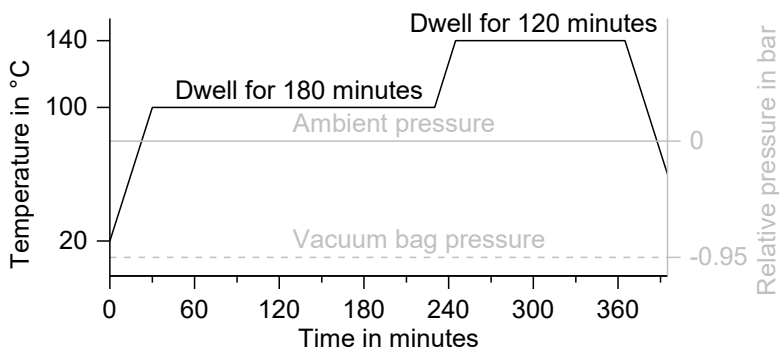
Figure 3.3: Curing process for the repair patch consisting of the Hexply M20/34%/UD194/IM7 T800S prepreg from Hexcel and the adhesive FM300-2M.06PSF from Solvay.

The film adhesive had an overlap of 5 mm on each side of the scarf endings, and the repair laminate plies were placed overlapping. As for the primary laminate and adhesive film, the materials were cut with the cutting machine

Aristomat TL 1625 from Aristo (Hamburg, Germany). For a precise placing of the film adhesive and repair plies, an aluminium mould was manufactured. The mould was fixed at the sides of the primary laminate plate (Step 1 in Figure 3.4). The film adhesive, as well as the repair laminate plies, were then placed in the designated steps of the mould (Step 2 and 3 in Figure 3.4). This way, a reliable placing of the repair patch could be achieved. The mould was removed prior to curing as the tack was strong enough to keep the adhesive and repair laminate in place. The combination of a plane primary laminate and a stepped repair laminate resulted in a varying bond line thickness (50 µm to 250 µm).
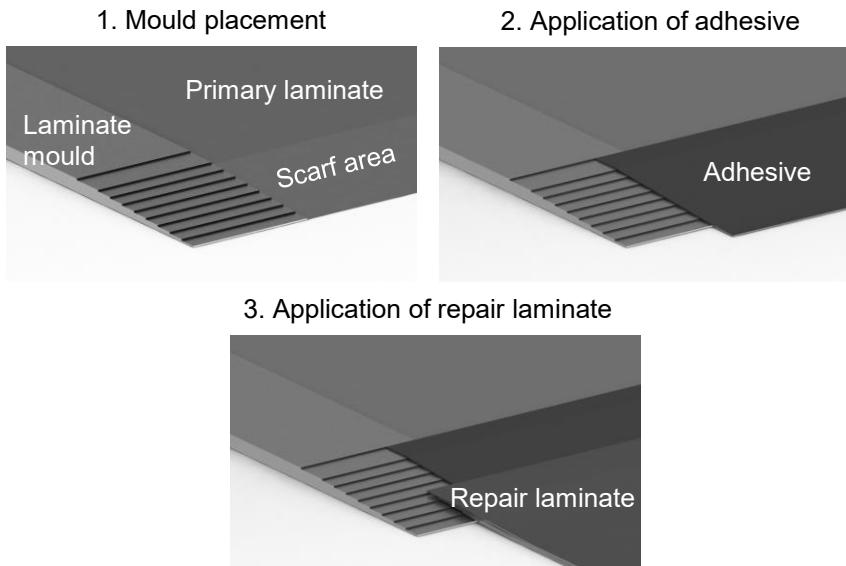
Figure 3.4: Schematic representation of the application of repair laminate with a mould. For the repair laminate, the first four plies are shown.

3.3 Milling

Milling was done in the facility of Lufthansa Technik (Hamburg, Germany). For the milling, a diamond-coated tungsten carbide tool from Mapal (Aalen, Germany) with a diameter of 6 mm, corner radius of 1 mm and eight cutting edges was used. Spindle speed was set to 15 915 min^{-1}, and the feed rate was 3.6 m·min^{-1}. A 5-axis CNC milling machine from Homag (Schopfloch, Germany) equipped with a suction system was used for processing. By pocket milling, the scarf was produced. After the milling, at a distance of 10 mm from the blunt scarf end and along the width of the plate, an area was ground. Therefore 320-grit sandpaper was used. This was done in order to avoid resin-rich areas at the scarf ends that could be critical for a laser treatment. This step could be easily substituted by a face milling for a later adaption of the repair process.

3.4 Surface treatment

Different surface treatments were applied on CFRP as well as carbon fibre rovings during the investigation.

For the milled CFRP surface the following configurations were tested:

- Untreated (**UT**): The CFRP surface was bonded without further treatment after the milling process.
- Release agent (**RA**): Release agent was applied on the surface in order to emulate a worst case for contamination.
- Solvent cleaning (**SC**): Solvent cleaning with isopropanol was used as a reference process as it is the default process for surface cleaning in aerospace (see Chapter 2.4.1).
- Laser treatment (**LT, LP1-LP9**): The laser treatment is generally referred to as **LT** in experiments where only one laser parameter was tested. For results involving all of the nine laser parameters, the configurations are numbered from **LP1** to **LP9**. **LT** corresponds to **LP4**.

- Release agent application with subsequent solvent cleaning (**RA+SC**): The contaminated surface was cleaned with isopropanol.
- Release agent application with subsequent laser treatment (**RA+LT**): Here, the laser treatment was used to remove the contamination.

For the carbon fibre rovings, the following configurations were tested:

- As received (**AR**): Fibres were tested as received without further treatment.
- Acetone rinsing (**AC**): Fibres were rinsed in acetone for 24 h. This has been used previously in order to remove the sizing [132,133].
- Laser treatment of the as received fibres (**AR+LT**).
- Laser treatment of the acetone rinsed fibres (**AC+LT**).

3.4.1 Solvent cleaning

Isopropanol (99.9 % purity) soaked paper wipes were wiped over the scarfed surface in 0° fibre direction until no residues from the milling process were visible on the wipes. The surfaces were given at least 1 h of time prior to bonding.

3.4.2 Release agent application

As a release agent, Mikon W-64+ from Münch Chemie (Weinheim, Germany) was used. The release agent is suitable for composites on an epoxy resin basis and can be used for application temperatures up to 450 °C. As recommended by the manufacturer, three layers have been applied with a cotton wipe. Though this scenario is unlikely for real contamination, it represents the worst possible case where no chemical bonding is possible. Since the variety of contaminations is nearly endless, the worst possible was assumed.

3.4.3 Laser treatment

Laser surface treatment was done at the laboratory of the Fraunhofer-Einrichtung für Additive Produktionstechnologien IAPT (former Laser Zentrum Nord) in Hamburg. A nanosecond pulsed 1060 nm Ytterbium fibre laser from IPG controlled by a scanning system. No process gas was added, while a suction was placed in a few centimetres distance of the surface. The main system characteristics are listed in Table 3.2.

Table 3.2: Laser system characteristics.

Characteristic	Value	Unit
Wavelength	1060	nm
Nominal average power	18	W
Maximum pulse energy[1]	0.06	mJ
Focused spot diameter	32.5	µm
Working area	100 x 100	mm^2
Beam quality, M^2	< 1.3	

[1] At 18 W and 300 kHz.

The primary scanning direction was parallel to the 0° fibre direction, as shown in Figure 3.5. The primary laminate was fixed on a vacuum plate and rotated in order to account for the scarf angle. This was necessary in order to treat the complete scarf area in the focus distance of the laser. Each surface was only processed once. This way process times between 1.0 cm^2/s to 7.4 cm^2/s were achieved.
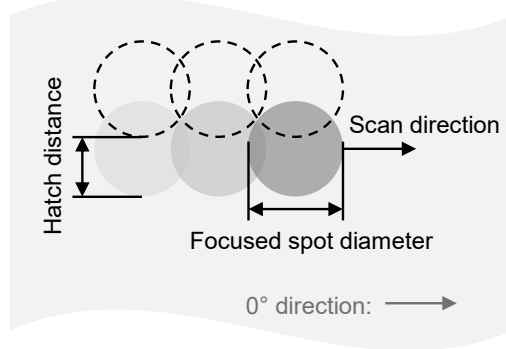
Figure 3.5: Schematic representation of the laser treatment process.

For the laser treatment of the carbon fibres, the rovings were spread and stretched so that the fibres were oriented in one plane and a high percentage of the fibres could be treated by the laser. For the analysis in the SEM and XPS, a length of approximately 20 mm of one roving was sufficient. For the BET analysis, a mass of around 2.5 g was necessary. For a 12K tow, the fibre diameter of 7 µm and a density of 1.8 g/cm^3 accounts to a mass per length of 0.8 g/m and around 3 m of carbon fibre roving. The roving was, therefore, wound around two fixed steel tubes with a distance of 105 mm (centre-to-centre) and a diameter of 16 mm until a length of 3 m was achieved. Only the straightly oriented parts of the carbon fibres were treated, meaning that some parts remained untreated. Since the aim of the investigation was to obtain a statement about the surface area change after the laser treatment, this approach was regarded as reasonable.

The laser parameters, including the pulse energy, pulse frequency, hatch distance and scan speed, can be found in Table 3.3.

Table 3.3: Laser parameter sets used for surface treatment. The parameter label, scan speed and hatch distance are given in each cell from top to bottom.

| | | In % of maximum pulse energy | | |
		40	50	60
Pulse frequency in kHz	150	**LP1** 1177 mm/s 12 μm	**LP2** 1793 mm/s 15 μm	**LP3** 2410 mm/s 19 μm
	200	**LP4 (LT)** 1897 mm/s 15 μm	**LP5** 2513 mm/s 19 μm	**LP6** 3130 mm/s 23 μm
	250	**LP7** 2617 mm/s 19 μm	**LP8** 3233 mm/s 23 μm	**LP9** 3850 mm/s 27 μm

The scan speed and hatch distance were adjusted for a given combination of the pulse energy and frequency in order to achieve a homogenous temperature field during the treatment. This approach was developed by the IAPT and verified by thermography measurements. The laser-treated specimens are labelled LP1 to LP9.

3.5 Specimen preparation

3.5.1 Cross-section preparation

Cross-sections were prepared for the analysis of the bond line. The specimen was embedded with KEM 15 plus from ATM (Mammelzen, Germany) and then polished with a Saphir 550 polishing machine from ATM. For the last polishing step, a diamond suspension with a particle size of 1 μm was used.

3.5.2 Ion beam milling

In order to investigate the depth effect of the laser treatment, ion beam milling preparation was used. This was necessary as a common mechanical polishing process would smear the surface. Ion beam milling, on the other hand, removes the material with minimal stress introduction [134].

Prior to ion beam milling, the specimens were cut to dimensions of 5 mm x 5 mm with a Brillant 220 precision saw from ATM. Preparation of the edge to be investigated is very important for good ion beam milling results. The effect of the cutting should be minimized. Therefore, a diamond-coated saw blade was used. The cutting direction was chosen such that tearing off of the fibres could be minimized.

Ion beam milling of the specimens and acquisition of the images of the unbonded surfaces has been done by the Wehrwissenschaftliches Institut für Werk- und Betriebsstoffe in Erding, Germany. The preparation of the bonded surfaces has been done by the following procedure. The specimen was placed in a slope cutter holder. The surface to be investigated faced the tungsten carbide mask (see Figure 3.6). A three-step process was applied where the surface was cleaned, polished and contrast enhanced in the EM RES102 ion beam milling system from Leica (Wetzlar, Germany). The corresponding process parameters are summarized in Table 3.4.
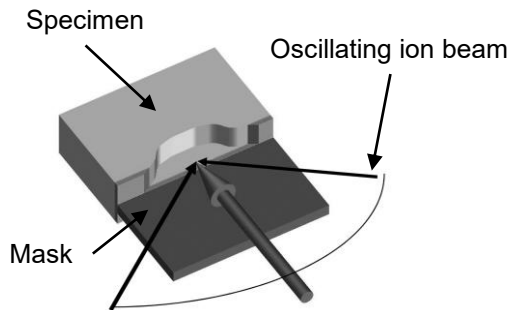
Figure 3.6: Principle of ion beam milling [135].

Table 3.4: Ion beam milling process parameter.

Parameter	Cleaning	Polishing	Enhancing
Acceleration voltage	4 kV	5 kV	3 kV
Gun current	1.8 mA	2.6 mA	1.5 mA
Oscillation angle		±70°	
Milling angle	10.5°	3°	90°
Milling time	10 min	23 h	3 min

3.5.3 X-ray photoelectron spectroscopy

As XPS offers a high sensitivity for the chemical characterisation of surfaces, avoidance of contaminations is essential. Therefore, the surface was covered with aluminium foil and fixed by adhesive tape on the edges during cutting. The specimens were cut to 10 mm x 10 mm for point measurements and 23 mm x 23 mm for area measurements. Then, specimens were wrapped in aluminium foil for transportation. This type of packaging for XPS specimens is common practise for CFRP and is assumed to have no influence on the surface [92].

3.5.4 Scarf bonded joint

After the repair in the co-bonding process (see Chapter 3.2.2), the specimens were cut in the Brillant 265 precision saw from ATM (Mammelzen, Germany). A diamond-coated saw blade was used. The specimens were cut to a width of 25 mm according to the standard DIN EN 6066 [136]. Even though the standard has been withdrawn, in the absence of a replacement, the standard has been used as a guideline for the geometry and testing procedure. As suggested by the standard, no end tabs have been used for static testing. For fatigue testing, end tabs were necessary as the specimen tend to slip out of the clamping otherwise. The end tabs were made of glass

fibre reinforced plastic and aluminium on the outer layer. The overall thickness of the end tabs was 2 mm.

A schematic illustration of the specimen geometry can be seen in Figure 3.7. Four different configurations constituting of four different scarf ratios between 1:10 and 1:30 have been tested. The corresponding geometry measurements can be found in Table 3.5.
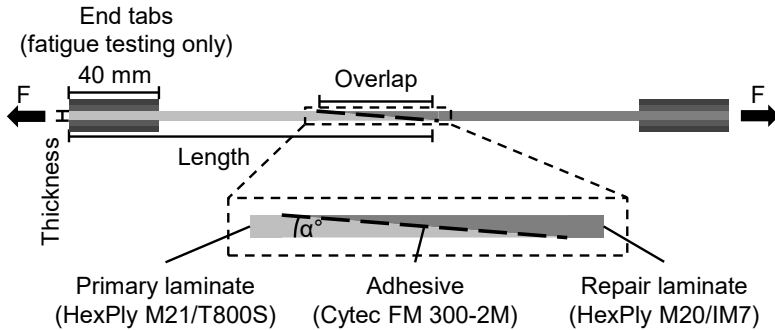
Figure 3.7: Scarf joint specimen geometry. The scarf angle is labelled as α.

Table 3.5: Scarf joint specimen geometry measurements. See Figure 3.7 for annotation.

Parameter					Unit
Scarf ratio	**1:10**	**1:15**	**1:20**	**1:30**	
Scarf angle	5.71	3.81	2.86	1.91	°
Overlap	15.0	22.5	30.0	45.0	mm
Length	115[1]	123	130	145	mm
Width			25		mm
Thickness			1.5		mm

[1]For fatigue testing the length was 105 mm.

38

4 Experimental methods

4.1 Quality assurance

4.1.1 Light microscopy

A BX51 microscope from Olympus (Tokyo, Japan) was used for the assessment of the embedded cross-section specimen. The microscope was used in bright-field mode.

4.1.2 Ultrasonic inspection

The bonded CFRP plates were tested with the pulse-echo method. Only the bonded area was investigated. C-scans were created with the ultrasonic imaging system USPC 3040 from Dr. Hillger (Braunschweig, Germany) for quality assurance. None of the inspected bonds showed a defect.

4.2 Surface analysis

4.2.1 Scanning electron microscopy

An SEM Supra VP 55 from Zeiss (Jena, Germany) with an Everhart-Thornley secondary electron (SE2) detector was used for a detailed analysis of the morphology. Samples were cut dry to dimensions of up to 20 mm x 20 mm and placed on a stub with a carbon adhesive disc. For an improved element contrast, the specimens were not coated. As epoxy resin has a low conductivity, the beam acceleration voltage was set to 1 kV to reduce sample charging. The aperture was set to 30 µm.

4.2.2 X-ray photoelectron spectroscopy

XPS has been widely accepted as the preferred method for the analysis of the elemental composition of the surface for adhesive bonding and has been used in numerous publications therefor.

A K-Alpha K1102 spectrometer from Thermo Scientific (Massachusetts, United States) with an Al-K X-ray source was used for the XPS analysis. All specimens were measured 1 d after the treatment, if not specified otherwise. The spectrometer operated at 36 W and a vacuum of 2.0×10^{-8} mbar. A pass energy of 150.0 eV was used for the spectra. All spectra were referenced to 285.0 eV binding energy of the C1s signal. The information depth of the measurement was approximately 10 nm. Two different measurement approaches were necessary:

1. 10 mm × 20 mm area scan of 110 points each having a diameter of 400 µm. This way, it was possible to account for inhomogeneities in the material like matrix-rich areas at the cost of not being able to deconvolute the element peaks.
2. Point scan with a diameter of 400 µm. With this type of scan, it was possible to deconvolute the C1s spectrum. The different peaks in the C1s spectrum indicate the chemical state of the carbon.

Using both methods, the chemical homogeneity of the laser treatment process, as well as the chemical state, were evaluated.

While the correlation of binding energies and the corresponding elements is quite clear for CFRP and carbon fibres, the deconvolution of the C1s spectrum is variously interpreted in different publications [137–139]. For the peak fitting of the C1s, the parameters of Lindsey et al. [140] were used, because it has been widely accepted and also showed a good fit quality for the measured surfaces. Seven peaks have been identified. The fit parameter, as well as the corresponding groups, are shown in Table 4.1.

Table 4.1: Peak fitting parameters of the bonds and functional groups [140].

Name	Bond / Functional group	Shift[1]
Aliphatic / aromatic structure	C–C	-
Amine group	C–NH$_2$	0.7
Hydroxyl group	C–OH	1.8
Imine group	C=NH	3.0
Carbonyl group	C=O	4.4
Carboxyl group	COOH	5.8
Shake up satellite	π–π*	7.0

[1]Shift from C–C peak

4.2.3 Adsorption measurement

The specific surface areas were determined by an adsorption measurement with a Surfer Gas Adsorption Porosimeter from Thermo Scientific (Massachusetts, United States), using nitrogen at a temperature of 77 K. The carbon fibres were dried at 120 °C for 6 h in a vacuum oven before the measurement as suggested in the literature [141]. The sample mass was between 2.5 and 3 g. The specific surface area was calculated by the BET method. The BET equation is given by

$$\underbrace{\frac{1}{W \cdot (\frac{P}{P_0} - 1)}}_{y} = \underbrace{\frac{C - 1}{W_m C}}_{a} \cdot \underbrace{\left(\frac{P}{P_0}\right)}_{x} + \underbrace{\frac{1}{W_m C}}_{b}$$

with the adsorbed weight W, the partial vapour pressure of adsorbate gas p, the saturated pressure of adsorbate gas p_0, the weight adsorbed in a monolayer W_m and the dimensionless BET constant C. For the calculation of the weight adsorbed in a monolayer, y is plotted versus x, and the slope a and

the intercept b are determined and then solved for W_m. The total surface area S_t is then calculated by

$$S_t = \frac{W_m N_A A_x}{M}$$

with the Avogadro's constant N_A, the cross-sectional adsorbate area A_X and adsorbate molecular weight M. At last, the total surface area is divided by the sample weight, which gives the specific surface area [142].

4.2.4 Roughness measurement

The roughness was measured with the surface profiler GD 120 from Mahr (Göttingen, Germany). For the evaluation, a section of 12.5 mm was divided into five parts and measured with a speed of 0.5 mm/s, as suggested by the given standard [143]. The surfaces were measured perpendicular to the fibre direction. Surface roughness values were evaluated according to DIN EN ISO 4287 [144]. The arithmetical mean deviation of the profile Ra

$$Ra = \frac{1}{l} \int_0^l |z(x)| dx$$

with the height coordinate z, the length of the profile x and the section of measurement l. Additionally, the surface roughness parameter Rz is calculated, that is given by the maximum peak to valley height.

4.2.5 Contact angle measurement

The change of surface energy free energy (SFE) was assessed through a contact angle measurement. Therefore, a 10 µl droplet was placed with a syringe on the surface, and the contact angle was measured with a high-resolution camera facing in the 0°-direction. The right and left contact angle were measured as shown in Figure 4.1. The average of both contact angles was used for the results and calculation of the surface energy. The specimens had a UD lay-up and were milled with a scarfing ratio of 1:20. The drop shape

analyser DSA100 from Krüss (Hamburg, Germany) was used for the measurement. Two testing liquids were applied for the evaluation of the surface energy: deionized water and diiodomethane. The polar and dispersive fractions of the testing liquids are listed in Table 4.2. The SFE was calculated according to the Owens-Wendt-Rabel-Kaelble (OWRK) method according to [145,146]

$$\underbrace{\frac{\gamma_L \cdot (\cos \alpha + 1)}{2 \cdot \sqrt{\gamma_{L,d}}}}_{y} = \underbrace{\sqrt{\gamma_{S,p}}}_{a} \cdot \underbrace{\frac{\sqrt{\gamma_{L,p}}}{\sqrt{\gamma_{L,d}}}}_{x} + \underbrace{\sqrt{\gamma_{S,d}}}_{b}$$

that can be derived from Young's equation. The contact angle α is measured for each testing liquid with the characteristic surface energies γ_L, $\gamma_{L,d}$, and $\gamma_{L,p}$. Then, the linear equations are solved for the slope a and intercept b, giving the surface energies of the solid surface $\gamma_{S,p}$ and $\gamma_{S,d}$. Five measurements were taken for each surface configuration.

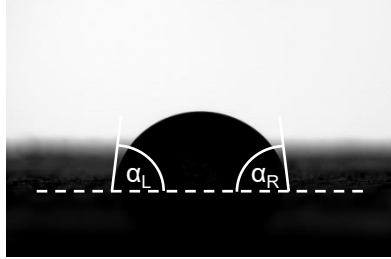Figure 4.1: Measurement of the left and right contact angle α_L and α_R.

Table 4.2: Surface free energy characteristics of the testing liquids at 20 °C [132].

Testing liquid	Surface energy in mJ/m^2		
	Overall γ_L	Dispersive $\gamma_{L,d}$	Polar $\gamma_{L,p}$
Deionized water	72.8	21.8	51.5
Diiodomethane	50.8	50.4	0.4

4.2.6 Fracture surface evaluation

The fracture surfaces were photographed with a digital camera (E-330 from Olympus, Tokyo, Japan). Qualitative assessment of the fracture surface was done by comparing the brightness on the primary and repair laminate. If the bright adhesive could be found on both surfaces, it was assigned to a cohesive failure (CF). Adhesive failure (AF) was assigned in the case that adhesive could be found on only one of the surfaces. In the case of adherend material on both surfaces, cohesive substrate failure (CSF) was assigned. For the quantitative assessment, images of the fracture surfaces were analysed by an image evaluation procedure in Matlab from The Mathworks (Natick, USA). For the first step, the fracture surface of the primary laminate was isolated. Then the adhesive on the primary laminate side was selected. This was possible by a brightness selection as the bright adhesive stood out against the dark CFRP. The selection of the adhesive and primary laminate is solely based on the brightness. Therefore, fibres from the repair laminate cannot be separated from the primary laminate. This poses a limitation to the image evaluation procedure. Overall, only a small amount of failed repair laminate is visible on the fracture surfaces, so that the error should be negligible. The number of pixels was calculated and divided by the total number of pixels. Additionally, the scarf endings were evaluated separately as these represent regions with stress concentrations for UD lay-ups. The mentioned regions reached from the scarf ending up to 10 % of the overlap length into the middle of the scarf. Figure 4.2 shows the process of data acquisition and the regions of interest according to the location on the scarf. With this method, it was possible to quantify the amount of adhesive on the fractured surface as a measure of the surface treatment quality for the UD lay-up specimens.

Original	Processed	Ratio of adhesive on primary laminate
	Blunt end — Feathered end	Overall: 40 % Blunt end: 17 % Feathered end: 39 %
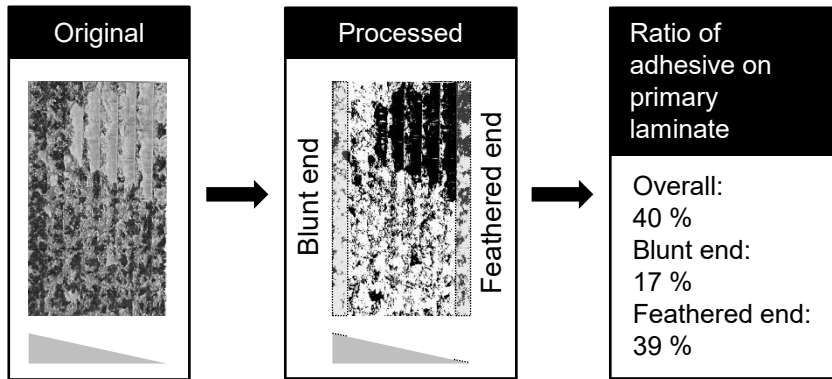
Figure 4.2: Processing of the fracture surface images by the evaluation procedure.

4.3 Mechanical testing

4.3.1 Scarf bonded joint – static strength

The static strength of the scarf bonded joint was evaluated by tensile tests. A Z100 universal testing machine from Zwick Roell (Ulm, Germany) was used for testing. The specimens were clamped at a length of 50 mm with a distance of 50 mm to the respective scarf ending. The extensometer multiXtens from Zwick Roell measured the displacement in a distance of 20 mm from the respective scarf ending. The experimental setup is shown in Figure 4.3. As recommended by the standard DIN EN 6066, a displacement rate of 2 mm/min was applied [136]. All tests were executed at an ambient temperature of 21 ± 1 °C and a humidity of 50 ± 10 %. For the evaluation of the strength for the specimen with a UD lay-up, the actual bonded area was measured from the fracture surfaces. The bond strength σ_A was therefore calculated by

$$\sigma_A = \frac{F}{w \cdot o}$$

with the failure load F, the width of the specimen w and the overlap o.

As the overlap was not assessable for the specimens with a QI lay-up, the thickness of the specimen was used for calculation of the strength. The strength was therefore calculated in terms of the laminate stress σ_t

$$\sigma_t = \frac{F}{w \cdot t}$$

with the thickness of the specimen t.

For every configuration, a minimum of five specimens was tested.
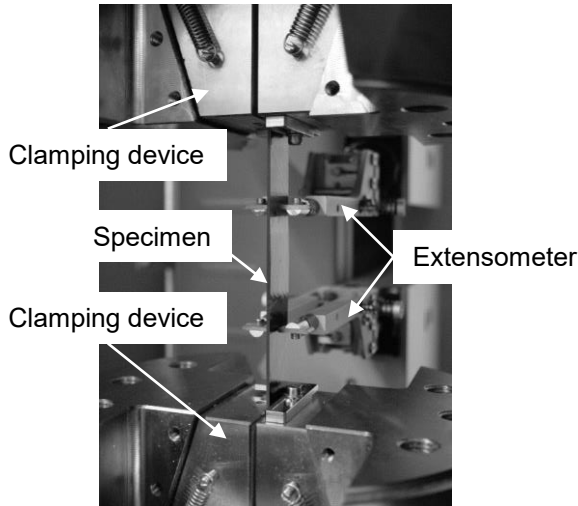
Figure 4.3: Experimental setup for the evaluation of the static scarf bond strength.

4.3.2 Scarf bonded joint – fatigue strength

For the fatigue tests, a servohydraulic testing system from Instron (Norwood, USA) was used. The specimens were tested in a tension-tension load cycle corresponding to a stress ratio of R = 0.1 at a frequency of 5 Hz. This was found to be a suitable frequency as no heating up of the specimens was observed during testing. All tests were executed at an ambient temperature of 21 ± 1 °C and a humidity of 50 ± 10 %. The fatigue test was

stopped when a specimen reached 10^6 cycles. The Wöhler line was calculated with the "Perlenschnurverfahren" according to DIN 50100 [147]. Only failed specimens were considered for the calculation of the Wöhler line.

5 Results and discussion

5.1 Morphological characterization

The morphological characterization will be analysed on two different scales that involve three different analyses methods. The first is the macroscopic scale, where changes from photographs that are visible without further magnification will be investigated. After that, the surfaces will be evaluated on the microscopic scale. First, by LM with areas of a several hundred micrometres, then, by SEM with areas of just a few micrometres. The basis of all images with CFRP surfaces is a milled surface.

5.1.1 Macroscopic surface

Figure 5.1 shows images of the UT, SC and LT surfaces in comparison side by side. While the UT and SC surfaces appear very similar and no difference can be pointed out, the LT surface shows distinctive characteristics. The LT surface is significantly darker than the other two configurations. As a result, the resin-rich areas are more clearly visible in the form of wavy lines for the LT configuration. The resin-rich areas are present in the SC as well as LT surface, which means that neither of the surface treatments is able to remove these layers. The LT surface appears to be smooth without fuzzy fibres protruding from the surface as reported by some authors [97,99]. This is a result of the low power laser used in this work which also should reduce the HAZ. The changed appearance of the LT configuration compared to the UT and SC configurations could be used as an indicator for surface treatment, thus simplifying a visual quality control of surface treatment.
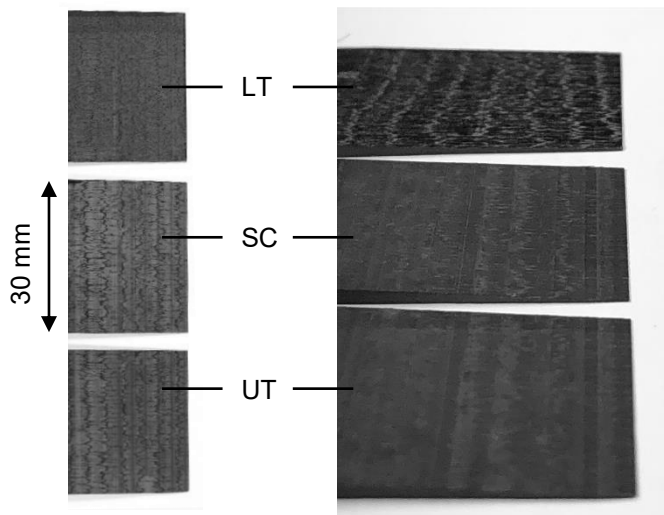
Figure 5.1: Comparison of the untreated (UT), solvent cleaned (SC) and laser-treated (LT) surface by photography. Left column: Top view. Right column: Side view with perspective.

5.1.2 Microscopic surface

LM images in Figure 5.2 only show slight differences between the three different surfaces. On the lowest magnification only in the area of the resin-rich areas, a difference is visible. Here, the UT and SC configurations show a smoother transition of the epoxy resin. For the LT configuration, this is not the case, as part of the epoxy resin could be removed. Looking at the higher magnifications, carbon fibre fragments can be seen on the UT and SC configuration. Fibre fragments are recognizable by the deviation from the 0° direction. Comparing the UT and SC configuration, a difference in the length of the fibre fragments can be observed. While the UT configuration shows a significant amount of fibre fragments that can reach lengths of up to 50 μm, the SC configuration shows only few fibre fragments which have lengths of less than 10 μm. This clearly shows the ability of the SC surface treatment to remove larger fibre fragments from the surface.

Figure 5.2: Images of the untreated (UT), solvent cleaned (SC) and laser-treated (LT) surface taken with a light microscope. Each column represents the same configuration, while each line represents the same magnification.

Overall, no fibre fragments are visible on the LT surface. This is a remarkable result, considering the low energy of the pulse and the fact that also large fibre fragments are removed from the surface, while the rest of the surface appears to remain intact. Considering the knowledge about the N-IR laser beam and CFRP surface interaction from Chapter 2.3.2, two reasons could be possible:

1. As shown in an analytical model by Emonts et al. [49], considerable pore pressures (up to 35 bar) are generated in the interface between the fibre and epoxy resin during a pulse. The generated pressure lifts-off fibre fragments, which are then drawn up by the suction of the laser system.
2. The same process, as mentioned in the first point, but larger fibre fragments are not directly drawn up by the suction. Instead, larger fibre fragments are lifted-off by the laser pulse and again land on the surface. This process is repeated until a critical length or mass is reached, such that the fibre fragment can be sucked up by the suction. As the surface is only processed once by the laser, this requires the fibre fragments to land in front of the laser pulse.

The three configurations also show clear distinctions in the SEM images in Figure 5.3. As in the LM images, fibre fragments can be seen on the UT as well as the SC surface. Exposed fibres of the UT configuration indicate fibre-matrix debonding during the milling process. Furthermore, on the UT surface, a layer of milling debris is visible. While the SC is able to remove the debris layer, smaller particles are still visible. The surface of the LT configuration shows higher contrast with stripped fibres reaching deep into the surface. The stripping of the fibres is a result of the heating and subsequent sublimation of the epoxy resin of the surrounding matrix as previously reported [54]. Though the exact temperature on the surface is not known, it can be estimated from the stripping behaviour: The M21 epoxy resin is known to decompose between 400 °C and 500 °C in air [148]. A T700 carbon fibre, which is similar to the T800S fibre in terms of thermal properties, decomposes between 700 °C and 1000 °C [149]. Therefore, in the proximity of the fibre temperatures of at least 700 °C are reached, while between fibres temperatures of at least 400 °C are possible.

Smaller epoxy resin particles are also visible on the LT surface. Furthermore, partially debonded epoxy resin strips can be observed on the LT surface. Here, the power was apparently too low to remove the epoxy resin. As these strips are still partially embedded into the surface, the suction was not able

to remove the debonded parts. Adding to the fibre stripping, an increased roughness of the fibres for the LT surface can be observed. The fibres show wavy indentations that in part resemble a flame. These indentations could be the result of the combustion process that was hypothesised by several authors [49,54].
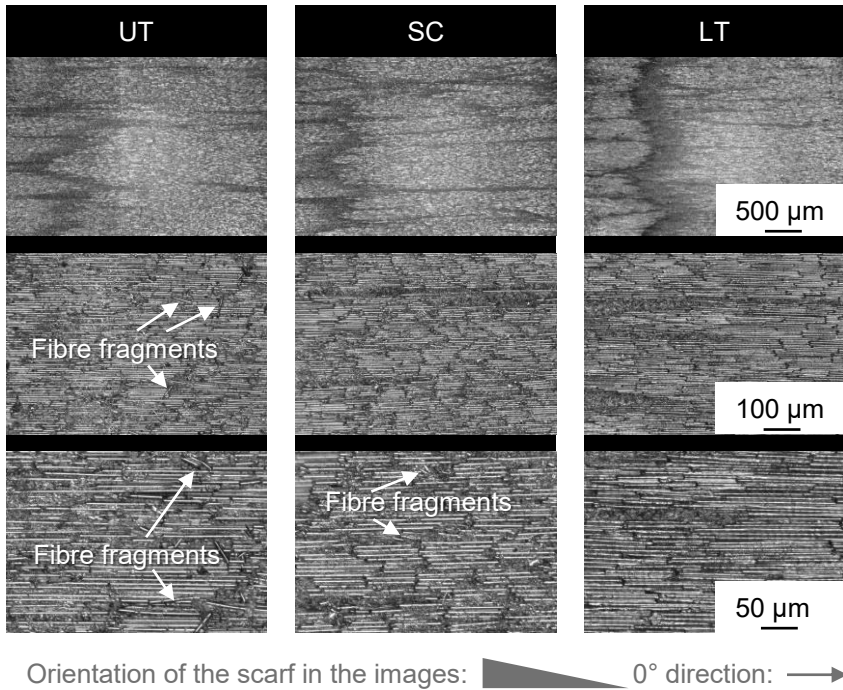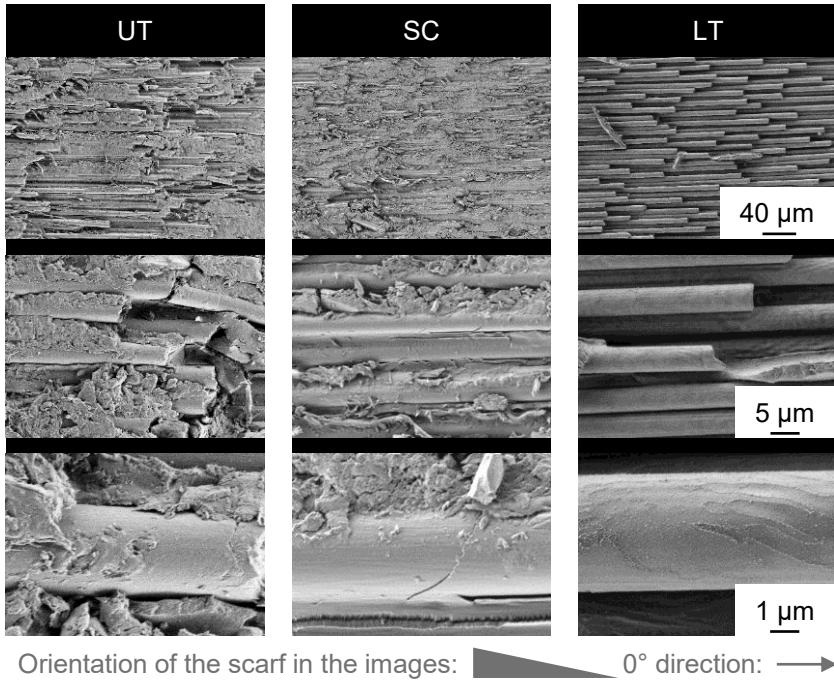

Figure 5.3: Images of the untreated (UT), solvent cleaned (SC) and laser-treated (LT) surface taken with an SEM. Each column represents the same configuration, while each line represents the same magnification.

Removal of residues

From the SEM images, it was evident that all configurations showed remaining debris on the surface to a different extent. Electrically conductive carbon adhesive discs (i.e. Leit tabs) with a diameter of 12 mm were bonded

to the surface, to examine the scale of the remaining debris. On the other side, the adhesive disc was bonded to an SEM pin stub with a matching diameter. Then, the adhesive disc was removed from the CFRP surface by a peeling movement.

Figure 5.4 shows the adhesive disc and the peeled off debris for the UT and SC configuration. For the LT configuration, it was not possible to remove the adhesive disc without significant damage. This indicates that the amount of loose debris on the LT surface must be very low and therefore supports the observations from Figure 5.3.

Figure 5.4: Debris removed from the untreated (UT) and solvent cleaned (SC) surface by an adhesive disc. The laser-treated (LT) configuration is not shown, as the adhesive disc could not be removed from the surface.

For the UT and SC configurations, the focus was on the largest observed agglomeration. From Figure 5.4, the difference between both configurations

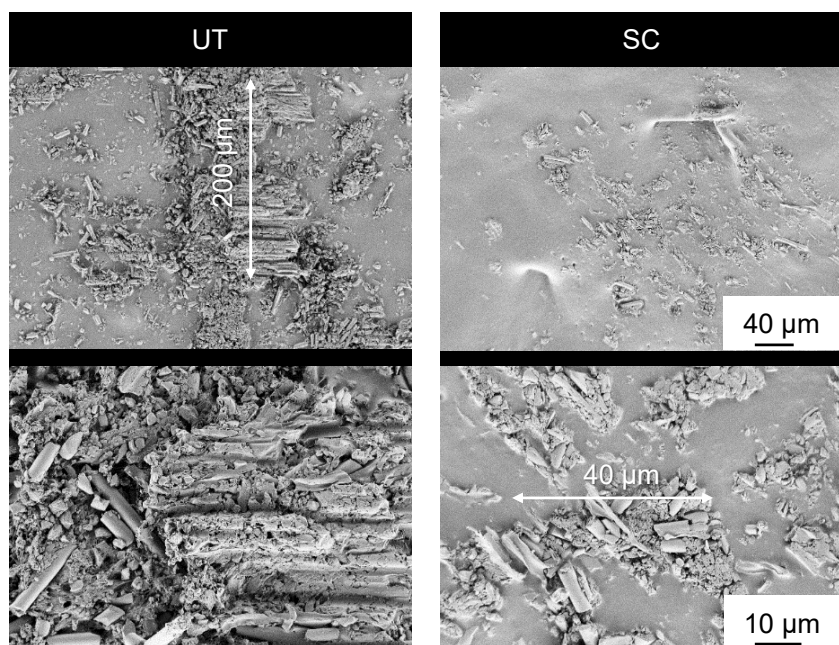is quite significant. While the removed debris on the UT configuration has a size of at least 200 μm and also a substantial depth, particles of around 40 μm length are visible on the SC surface. Apparently, the solvent cleaning is already able to remove larger debris agglomerates that originate from the milling process, though some smaller particles still remain on the surface. While it was not possible to examine the LT configuration, the results show that a significant amount of milling debris can be removed, thus achieving a good bond with the adhesive disc.

Comparison of different laser parameters

Differences between the investigated laser parameters were only visible in the SEM. Figure 5.5 shows that all tested laser parameters are able to strip the fibres, though the degree of stripping varies. The highest degree of stripping and the cleanest surface can be observed for LP4, LP5 and LP6. These three laser parameters were treated at a pulse frequency of 200 kHz. The adjustment of the scan speed and hatch distance appears to work better for this pulse frequency. As for the stripping, all laser parameters show a roughening of the fibre and removal of milling residues. Remaining epoxy resin appears to be embedded into the surface, though a clear distinction is not always possible for laser parameter with a high percentage of remaining epoxy resin (e.g. LP9). Nevertheless, in the case of embedded epoxy resin, no negative effect on the adhesive strength can be expected since the bonding between epoxy resins is known to be sufficiently good even without surface treatment [25].

From the comparison of the different laser parameter, LP4 showed good stripping without significant damage to the fibres. Furthermore, from the parameters with a pulse frequency of 200 kHz, it had the lowest pulse energy. Hence, a low thermal impact on the surface with effective stripping could be expected. As a consequence, LP4 was chosen for further detailed assessment.
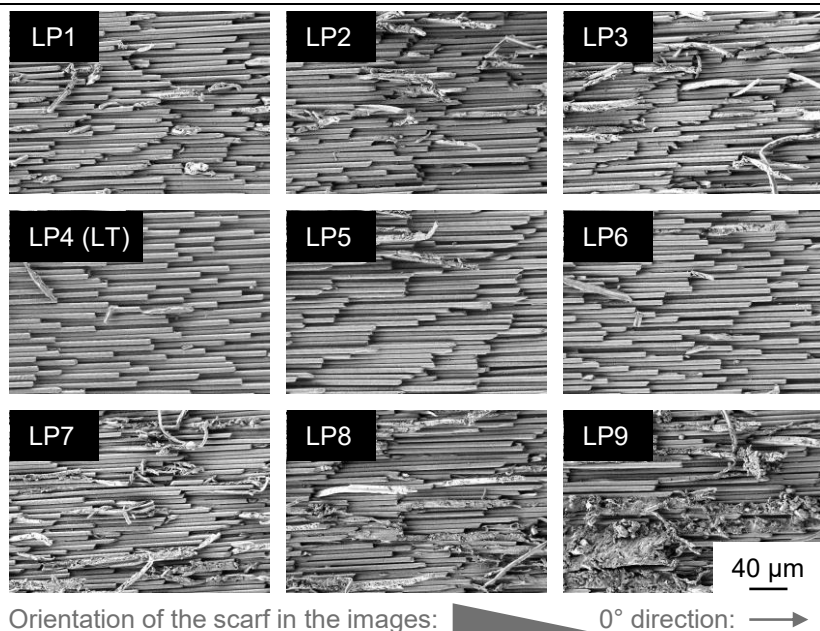
Figure 5.5: Comparison of different laser parameters in the SEM. All images were taken at the same magnification.

Effect of different fibre directions in a lay-up

The laser surface treatment followed a strategy where the surface was only treated in the 0° direction. CFRP, on the other hand, is a highly anisotropic material with different thermal conductivity parallel and perpendicular to the fibre direction [150]. The anisotropy of CFRP, on the other hand, means that for lay-ups that contain multiple fibre directions, the heat distribution will be different for each ply.

The heat distribution is an essential aspect of the laser surface treatment results and therefore needs to be considered. As laminates with multidirectional lay-ups are common in aerospace structures, it was essential to investigate the effect of the laser treatment on these laminates.

Figure 5.6 shows the different ply orientations of a laser-treated scarf with a QI lay-up. No apparent difference in the morphology can be identified when comparing the different ply orientations. The effect of the laser treatment appears to be very similar for all ply orientations. Presumably, this is a result of the low pulse energy and duration of the laser system used for this investigation. As an effect, the material is only heated in the vicinity of the laser pulse. Furthermore, all parameters involve an overlap of at least 46 % related to the pulse distance and at least 17 % related to the hatch distance. That means that for all laser parameters, the whole surface is covered by the laser pulses, which leads to a homogenous treatment independent from the ply orientation.
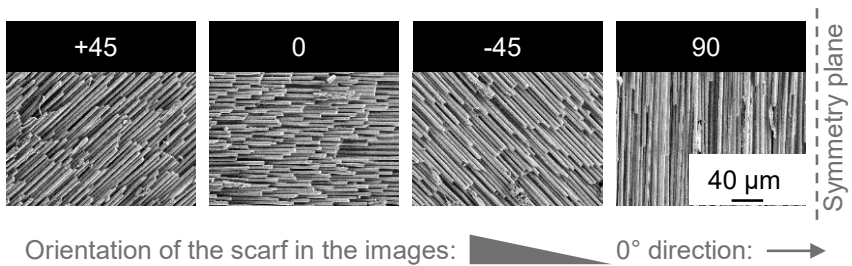
Figure 5.6: SEM images of the different ply orientations of the laser-treated (LT) scarf with a QI lay-up.

Fibre bundle treatment

In order to separate the effect of the laser treatment on the fibre and matrix, treated carbon fibre bundles were investigated by SEM. Even though the environment during the treatment of fibre bundles differs from the laser treatment of CFRP, which means: All of the fibres are surrounded by air, and no matrix is involved. Still, as some of the fibres are partly stripped after the milling, the laser treatment of carbon fibre bundles contribute to the understanding of the processes taking place on the top-most layer.

Figure 5.7 shows a comparison between the acetone treated (AR) and as-received (AC) as well as the laser-treated (AR+LT, AC+LT) combinations of both. Comparing the AR and AC configuration, no clear difference can be observed. Both configurations show a smooth surface with slight striations in the fibre direction. Similar results have been reported previously for T700S fibres [116]. The T800S fibres from the UT and SC configurations of the CFRP as shown in Figure 5.3 have slightly deeper striations, which is also in accordance with the literature [114]. Whether the sizing could be successfully removed by the acetone treatment is not identifiable from the SEM images. As the thickness of the sizing tends to be around 0.03 μm, removal would not necessarily be recognizable in the SEM for the given magnifications [103].

After laser treatment, both configurations show an increase of roughness. For the AR+LT configuration combustion marks are visible. Furthermore, a roughening and particles of a few nanometres size can be observed. Overall the fibre appears very similar to the laser-treated fibres in the CFRP from Figure 5.3. The same holds true for the AC+LT configuration, though no combustion marks are visible. One reason for that could be the increased energy of the combustion in case of the as-received fibre because of the sizing. For CFRP the combustion effect is even intensified because the fibre is additionally surrounded by epoxy resin.

The particles that are visible after the laser treatment are likely a byproduct of the combustion process, similar to so called "low molecular weight oxidized material" (LMWOM) that results from intense plasma treatment of polymers. These particles appear not to be bonded to the surface. In case of LMWOM, particles can be washed off with, e.g. ethanol. Some studies found a strength decreasing effect, while others showed no influence from LMWOM and argued that particles could be successfully integrated into the load bearing surface [151]. Thus the effect of such particles cannot be clearly stated.
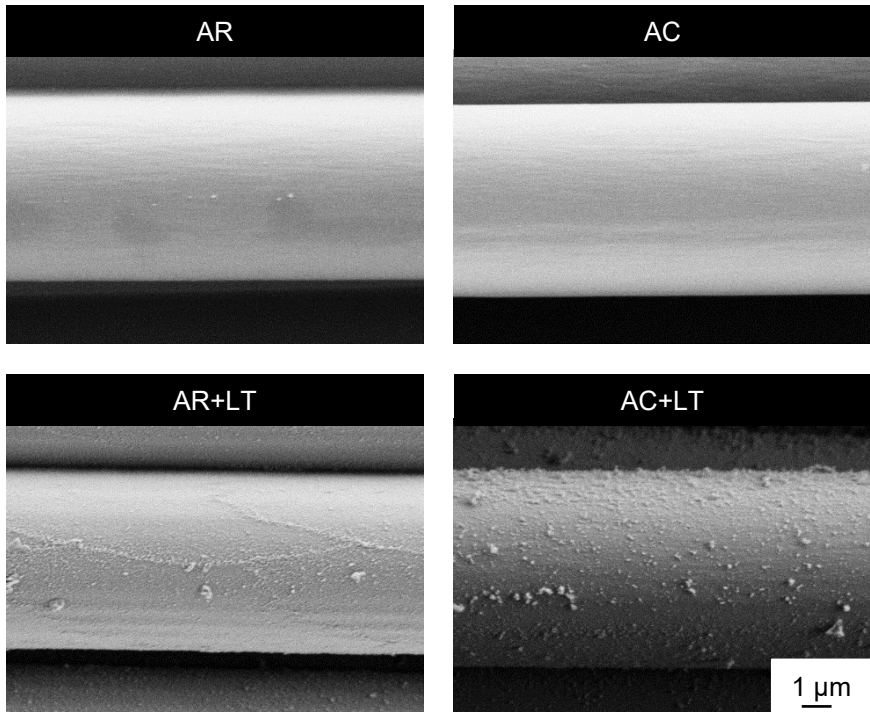
Figure 5.7: Comparison of the as-received (AR), acetone rinsed (AC) and afterwards laser treated (AR+LT, AC+LT) configuration of carbon fibres.

5.1.3 Laser surface treatment depth

Due to the N-IR laser and CFRP surface interaction, a detailed investigation of the treatment depth is necessary. As mechanical abrasion preparation methods did not show any differences between the configurations, cross-sections have been prepared by ion-beam milling. During ion-beam milling, particles can end up on the top surface and it may appear less clean than in Figure 5.3 and Figure 5.5.

A comparison between the SC and LT configuration can be seen in Figure 5.8. The cross-section reveals that the milling process introduces inter-fibre failure of a few micrometres depth. Inter-fibre failure is a result of the forces applied during the milling process and have been previously reported for CFRP [46]. These defects are limited to the top-most fibre layer and are comparably small.
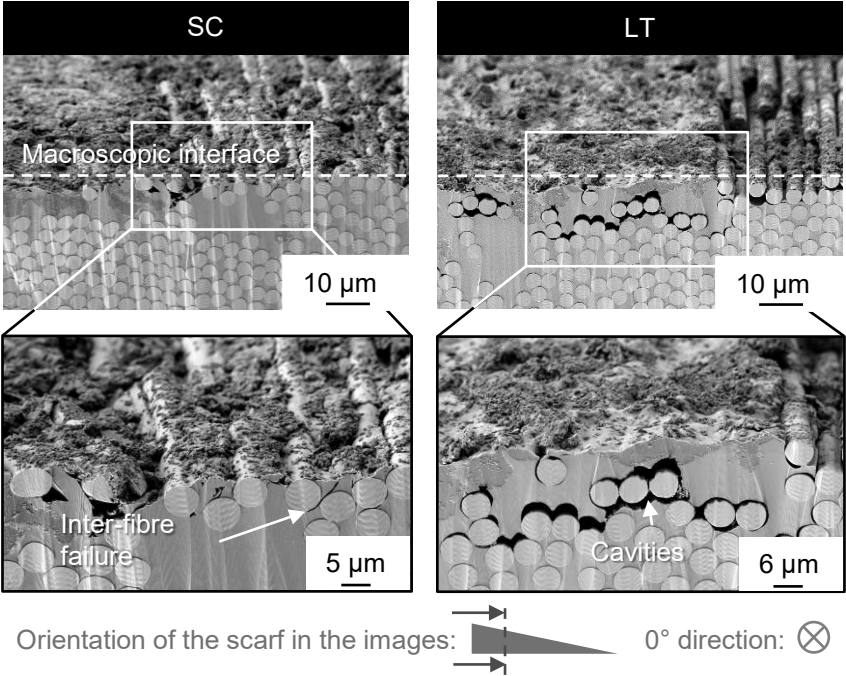
Figure 5.8: SEM images of the laser treatment prepared by ion beam milling. Comparison between solvent cleaning (SC) and laser treatment (LT).

For the laser-treated configuration, two phenomena depending on the depth of the first fibre layer are visible.

1. Fibres that were already partially stripped on the surface of the macroscopic interface are completely stripped along the entire

surface. Some of these fibres even appear to be lifted, as they are no longer bonded to the epoxy resin.

2. Because of the wavelength, the laser also targets the first fibre layer that is covered by epoxy resin. In that case, the epoxy resin in the vicinity of the fibre is removed, and complete stripping of the fibre is not possible. The covering epoxy resin layer is no longer bonded to the fibre and cavities develop.

Figure 5.8 also indicates that a layer of only a few micrometres (around 5 µm) of epoxy resin is enough to disrupt the stripping of the fibres. This is a result of the low power laser used in the investigation. On the other hand, the surrounding epoxy resin appears to be unaffected showing no sign of degradation. Furthermore, the fibres are still well aligned even after the laser surface treatment.

Figure 5.9: SEM image of a laser-treated (LT) surface showing the stripping under resin-rich area.

As resin-rich areas were found to be critical for the fibre stripping effect, additional images were taken with the SEM to achieve a three-dimensional impression of the laser treatment.

Figure 5.9 shows a laser-treated surface that focuses on a resin-rich area. Additionally, the surface was tilted by 45° to see the effect in depth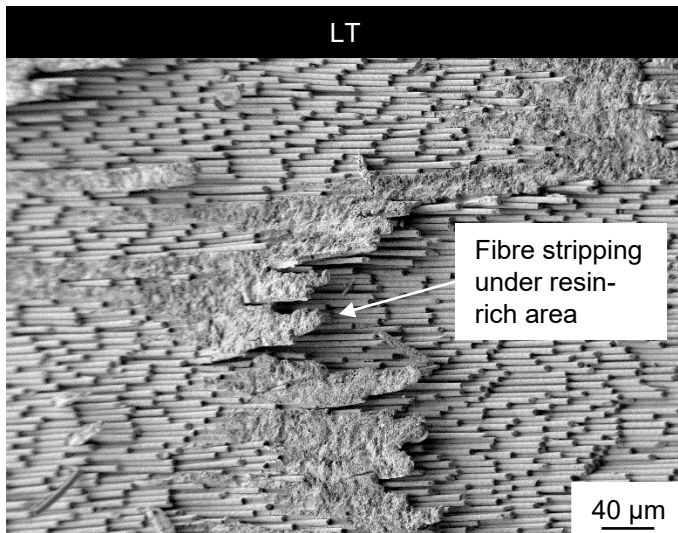 and in the surface plane. In the proximity to the resin-rich area, the laser stripping is identical to that of a fibre-rich area. From the shadow under the resin, it can be concluded that resin of a significant thickness has been removed, which is in accordance to the findings from Figure 5.8. This leaves access to the stripped fibres and cavities under resin-rich areas. The effect of cavities depends on whether they can be infiltrated by an adhesive. Consequently, a bonded surface was investigated in the next step.

The top image in Figure 5.10 shows a few hundred micrometres of the bonded surface after laser treatment. Though a holistic view for the evaluation of the treatment depth is not possible due to the preparation method, some general approximations can be derived. The adhesive, as well as the carrier fibres of the adhesive and the constituents of the CFRP, can be distinguished by their shade of grey. The image clearly shows that overall a significant amount of the cavities can be filled by the adhesive. In terms of mechanical interlocking, this should benefit the adhesive properties of the bond. On the other hand, connected cavities as large as 100 µm can also be found close to the surface as seen in the bottom image in Figure 5.10. Here, the dependency of the cavity depth on whether it can be filled can be observed well as both marked cavities are partially filled. The depth for which the cavities can be filled varies between 20 µm and 30 µm. Therefore, from the investigated section, it can be concluded that areas with epoxy resin layers that are thicker than 30 µm lead to unfilled cavities. Moreover, these cavities can reach lengths of 100 µm in at least one dimension.

As a similar temperature and viscosity of the adhesive throughout the curing can be assumed for both cavities, the depth of the filling must largely depend on the volume and accessibility of the cavities. Furthermore, the filling of cavities also depends on the volume of the adhesive. Given that the thickness

of the adhesive varies throughout the bondline, sections with lower thickness should be able to fill a higher ratio of cavities. Following the 0° fibre direction to the surface, the partial volume of the cavities decreases, which increases the chances of a filling.
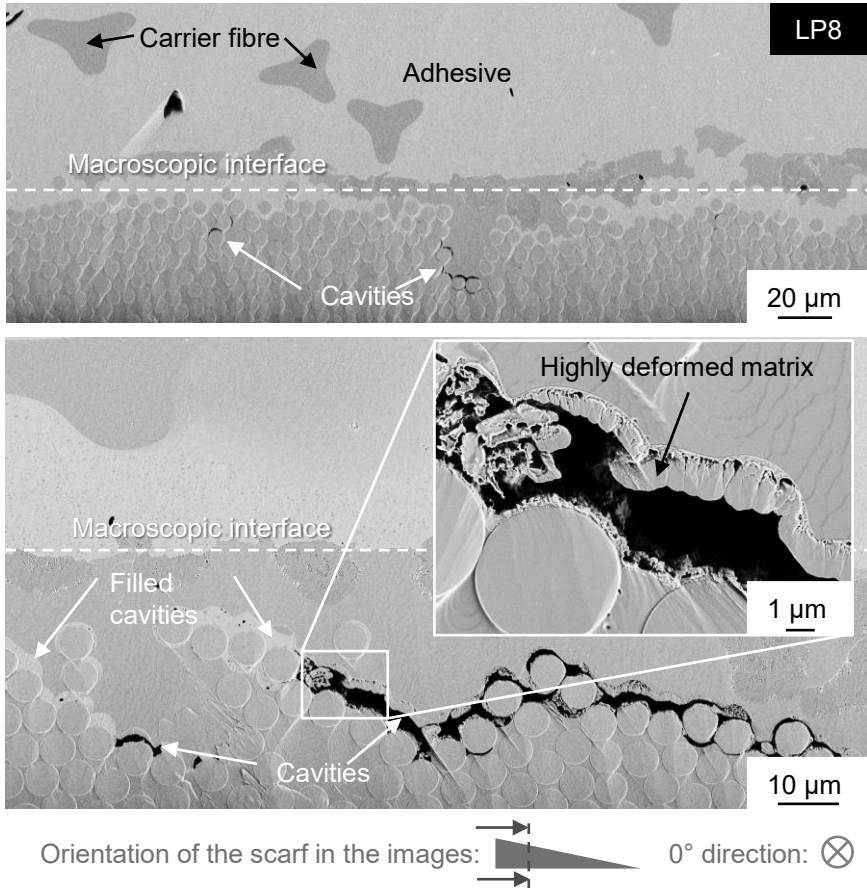
Figure 5.10: SEM image of a laser-treated and bonded surface with large epoxy resin-rich areas and small cavities prepared by ion beam milling.

The 0° fibres run through the complete length of the adherend and are connected to the scarf. Therefore, it is reasonable to assume that cavities can

be partially filled perpendicular to as well as in 0° fibre direction. Nevertheless, cavities represent potential weak points in the bonded surface. As the whole dimension of the cavities, as well as the critical size of a defect, cannot be quantified, mechanical testing is necessary in order to evaluate the effect.

Another remarkable observation can be made from Figure 5.10. The epoxy resin inside the cavities appears to be highly deformed which is surprising given the fact that epoxy resin is not meltable after curing and furthermore shows brittle behaviour. On the other hand, previous studies showed that epoxy resin could undergo large deformations if the volume is sufficiently small [152]. In the case of laser treatment, high temperatures could facilitate highly deformed epoxy resin.
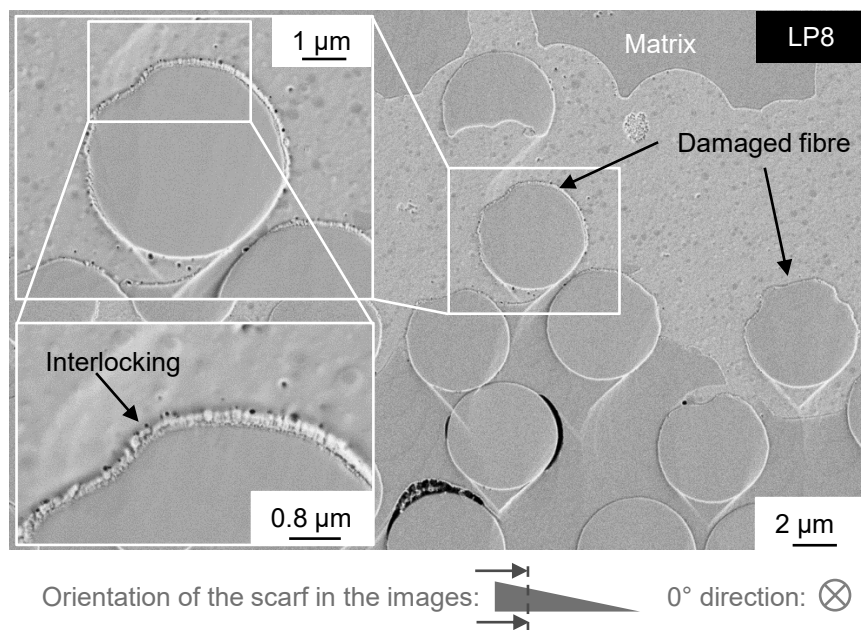
Figure 5.11: SEM image of a laser-treated and bonded surface prepared by ion beam milling. Detailed view of the fibre roughening effect.

In the last step, the interaction between laser-treated fibres and the adhesive was investigated. Figure 5.11 shows fibres in the proximity of the macroscopic surface that are surrounded by the adhesive. The indentations on the fibre surface are clearly visible in the cross-section view indicating that the fibre has been damaged. These indentations are only visible on the upper part of the fibre. Here the effect of the laser beam is more pronounced.

Increasing the magnification, an interlocking between the fibre interface and the adhesive can be observed. It is not possible to state whether the interlocking happens between the particles or the fibre and the adhesive, though it appears as the rough section is part of the fibre. This would support the theory that the particles can be incorporated into the load bearing interface. The roughening is likewise only visible on the upper part of the top most fibre layer. As for the fibre stripping and filling of cavities, an increase of the adhesion with regards to the mechanical interlocking can be assumed through the roughening of the fibre on a nanoscale. On the other hand, the effect on the fibre roughening is only limited to the upper half of the first fibre layer. Furthermore, the fibre is weakened by the reduction of the diameter.

5.2 Surface roughness

The morphological characterization in Chapter 5.1 showed that the surface roughness is significantly influenced by surface treatment. The macroscopic roughness, on the other hand, was shown to be a good indicator for the bond strength of milled CFRP surfaces [46]. With increasing surface roughness, the bonded surface area increases and as a consequence, the bond strength improves. Therefore, the surface roughness was quantified by a tactile measurement. The profiles of the respective surface configurations are given in Figure 5.12. The LT configuration showed some pronounced peaks that cannot be explained by the stripping of fibres but rather partly detached fibres. Since these peaks would disproportionately contribute to the surface roughness values, they were marked as outliers according to a distance of three scaled median absolute deviations from the local median. Outliers were linearly interpolated by the closest non-outlier values. Qualitatively the profiles already can be well distinguished. While the UT and RA configurations show small peaks, the size of the peaks significantly increases for the SC and even further for the LT configurations. The peak heights of the outliers from the LT configuration can be reduced effectively. Comparing the profile heights with the cross-section views in Figure 5.8 and Figure 5.10, the removal of outliers seems to be achieved with reasonable precision. Furthermore, detached fibres can also be regarded as an increase of the surface area since the adhesive can bond to the bottom side of the fibre.

Figure 5.13 shows the evaluation of the roughness profiles with the arithmetical mean deviation of the profile Ra and the maximum peak to valley height Rz. The determined roughness values confirm the observations made from the profiles.

Figure 5.12: Surface profiles for the release agent applied (RA), untreated (UT), solvent cleaned (SC) and laser-treated (LT) configurations. Scales for length and profile depth vary.

The LT configuration shows the highest roughness for both parameters and even after correction for outliers. The removal of the outliers more than halves the values of *Rz* from 29.7 µm to 14.1 µm and significantly reduces the standard deviation. The surface roughness parameter *Ra* is by definition less influenced by outliers and therefore only reduced by less than 10 %. This emphasises that the surface is most likely roughened beyond the detached fibres. As already seen from Figure 5.3, laser treatment is able to strip the fibres, which increases the roughness values.

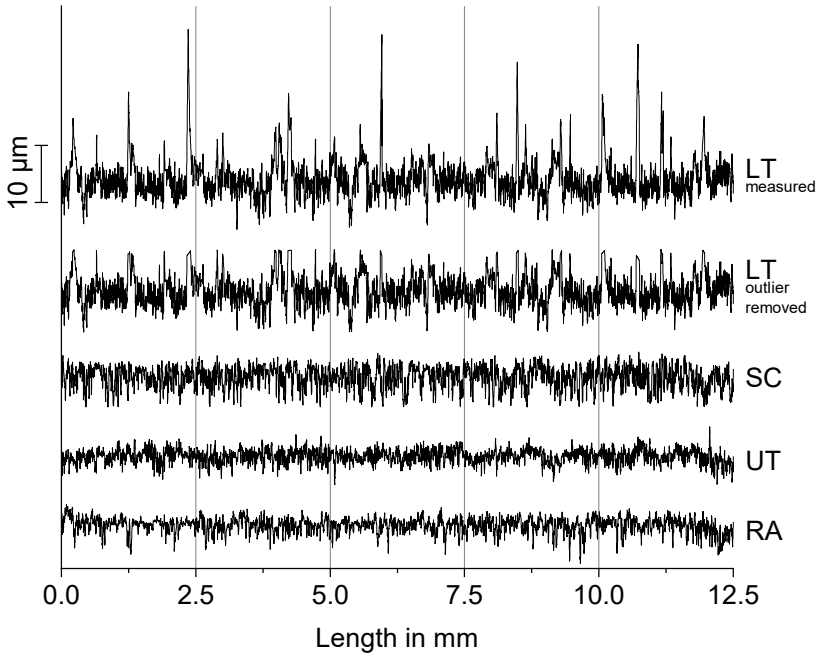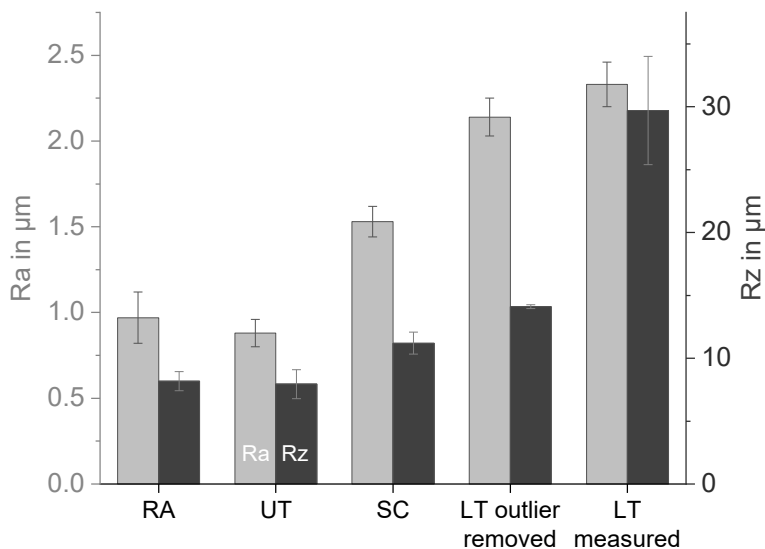Figure 5.13: Comparison of the surface roughness parameter Ra and Rz for the release agent applied (RA), untreated (UT), solvent cleaned (SC) and laser-treated (LT) configuration.

The achieved arithmetic surface roughness value Ra of 2.14 µm is close to the theoretical value of 2.04 µm for an in-plane milled CFRP surface with uniformly distributed fibres with a diameter of 5.2 µm as proposed by de Freese et al. [46]. For a T800S carbon fibre with a diameter of 5 µm, a theoretical arithmetic surface roughness Ra of 1.96 µm can be calculated. Given that the fibres are not evenly distributed and resin-rich layers are present on the surface, the measured value for the LT configuration after removal of the outliers appears to be in reasonable agreement. The comparably high roughness furthermore emphasises an efficient stripping and cleaning effect of the laser treatment. The surface roughness for the UT and RA configuration is significantly lower than for both surface treatment methods. This is due to the fact that the milling residues fill out the surface cavities. The higher roughness of the RA configuration compared to the UT

configuration could be attributed to the application of release agent with a cotton wipe, thereby removing some of the milling residues.

According to the previously determined correlation between the roughness and adhesive strength of a milled surface, both surface treatment methods should improve the bond strength. For the SC configuration, the governing mechanism behind the increased roughness is assumed to be the removal of milling debris between the fibres. As milling debris tends to fill out space between the fibres, a removal is accompanied by an increase of the roughness. The further increase of the roughness for the LT configuration is a result of the additional fibre stripping. Whether the increased roughness of the LT configuration also benefits the bond strength is not clear, since it is accompanied by the formation of cavities.

5.3 Chemical composition through XPS

Assessing the chemical composition of milled CFRP combined with an N-IR laser surface treatment is not as straight forward as, e.g. for plasma treated surfaces that are covered by epoxy resin. First of all, due to the diameter of the measurement spot ($\sim$ 400 µm), the spectrum of a milled CFRP surface is an average of both constituents, the carbon fibre and the epoxy resin. Both have different chemical compositions that can differ greatly. Furthermore, during the laser treatment, the ratio between both constituents changes. In order to account for the changing ratio of the materials and the effect of the laser treatment, separate studies have been conducted. In the first step, the effect of the laser treatment on milled CFRP surfaces has been investigated. This study also involved the chemical characterisation of the epoxy resin and a laser parameter study. In a second step, the effect of N-IR laser treatment on the chemical composition of carbon fibre bundles analogously to the morphological characterisation from Chapter 5.1.2 has been investigated. Lastly, the ageing behaviour of laser surface treatment was examined. As time spans between the surface treatment and bonding process can vary, it was relevant to study the effect of time on the chemical composition of the surface. The following chapters are structured as follows:

1. The elemental composition is evaluated. As the ratio of oxygen to carbon (O/C) and nitrogen to carbon (N/C) is a good indicator for a functionalisation of the surface (see Chapter 2.4 and 2.5.2), special interest was on both of these factors.
2. One of the main advantages of the XPS measurement compared to other surface chemistry characterisation methods is the ability to evaluate the chemical bonding state of the different elements. For carbon fibres and epoxy resin, the bonding state of carbon is of particular interest as it can provide information about functional groups that are bonded to the carbon. Therefore, the deconvolution and shape of the carbon peaks (C1s spectra) are discussed in a second step.

3. Lastly, the chemical bonding states of carbon are quantified and assessed.

5.3.1 CFRP

Figure 5.14 shows the elemental composition of the bulk matrix, the SC and LT configuration. From Chapter 5.1.2 and 5.1.3, a significant fibre stripping effect was identified after the laser treatment. As a result, matrix and fibre-rich regions could be identified. Therefore, for the point scan results, the laser-treated surface has been investigated separately in terms of matrix and fibre-rich. Still, the point scan has to be seen as a composition of both constituents. This is especially true for the matrix-rich region, as the spot diameter is significantly larger than at least one dimension of the matrix-rich region (compare Figure 5.2).
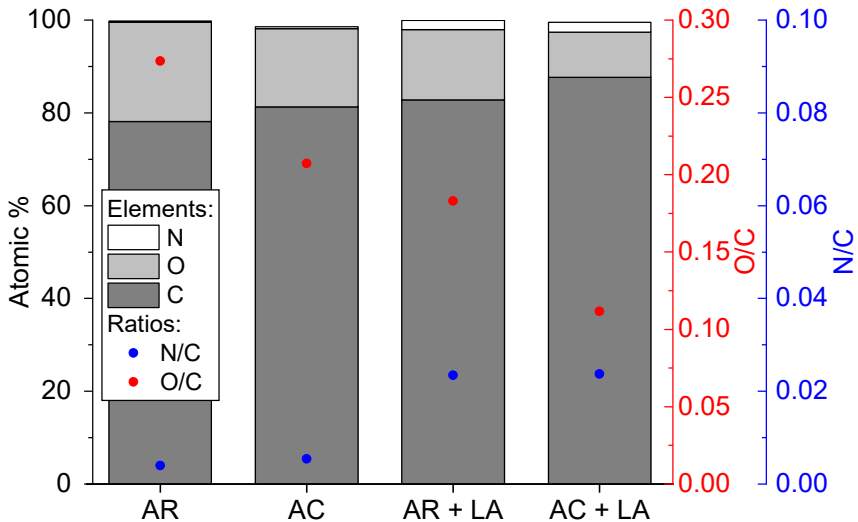

Figure 5.14: Surface elemental composition of the bulk matrix and milled CFRP after solvent cleaning (SC) and laser treatment (LT).

Carbon and oxygen account for at least 90 % for all configurations and are therefore by far the most present elements in epoxy resin and CFRP. Furthermore, smaller amounts of nitrogen and sulphur were detected. The results show no indication of a functionalisation on the surface, but rather a decrease of the O/C ratio after the laser treatment, especially for the fibre-rich region. Though an increase of the N/C ratio is observed for the matrix-rich region, the increase is significantly lower than the decrease of the O/C ratio. The bulk matrix shows the highest O/C ratio and sulphur content of all configurations. Epoxy resin is known to have a relatively high oxygen ratio of around 20 % [153]. Furthermore, sulphur most likely cannot be found on the carbon fibre surface. A significant decrease of sulphur can be identified for the LT (fibre- and matrix-rich) as well as SC configuration compared to the bulk matrix. Both configurations show stripped fibres to a varying degree on the surface. Therefore, a decrease of the O/C ratio of the LT configurations can be attributed to the decrease of epoxy resin on the surface to some extent.

To get a better understanding of the processes that could lead to the changes of the elemental composition on the surface, the C1s spectra of the respective configurations were compared as seen in Figure 5.15. Generally, a very good agreement between the XPS signal and the fitting (envelope) was achieved for all configurations. All configurations have a significant amount of carbon-carbon bonds. Given the high carbon ratio on the surface, this is a reasonable result and in accordance with the literature [104]. Except for the fibre-rich LT configuration, the hydroxyl group has the highest ratio of all functional groups. Hydroxyl groups are present in cured epoxy resin systems that involve an amine curing agent, which is generally the case for prepreg type epoxy resins [154]. Adding to the change in the elemental composition, the comparably low hydroxyl content of the LT, fibre-rich configuration is another indicator for the removal of epoxy resin, but cannot be correlated to removal of functional groups on the fibre.
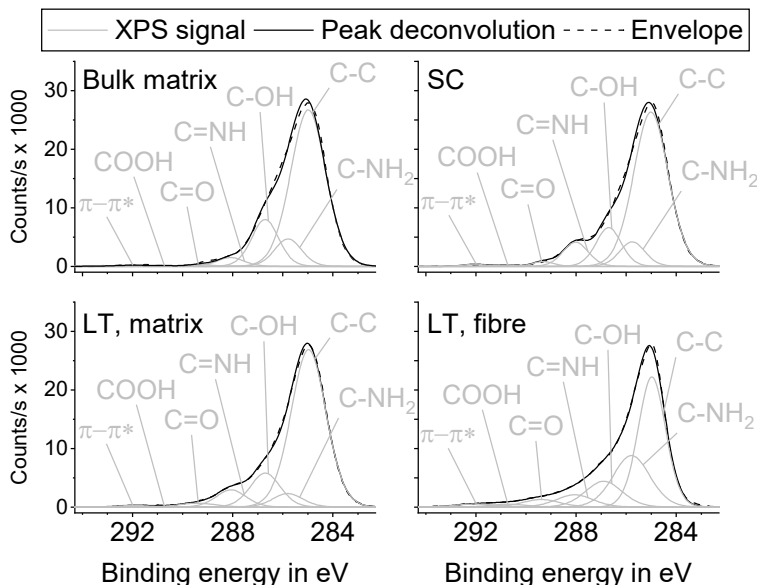
Figure 5.15: C1s spectra of the bulk matrix and milled CFRP after solvent cleaning (SC) and laser treatment (LT).

An evaluation of the functional groups present on the surface is given in Figure 5.16. The fibre-rich region of the LT configuration stands out in terms of the $C-NH_2$ ratio, which is significantly higher than for the other regions. A high amount of $C-NH_2$ functional groups is characteristic for electrochemically treated carbon fibres [140]. Electrochemical oxidation is the preferred surface treatment method for industrially produced carbon fibres and has most probably been used for the manufacturing of the T800S carbon fibres. Additionally, the LT fibre-rich configuration shows the highest ratio for the COOH functional group, which is known to be an indicator for good bonding to epoxy resin [112]. All of the configurations show a high ratio of functional groups on the surface with at least 28 % of the C1s peak being composed of functional groups. As a functionalisation from the solvent cleaning can be ruled out, the underlying surface is already suitable for adhesive bonding after the milling process, from a chemical point of view.

Furthermore, it is known that epoxy resin bonds well to epoxy resin, if the surface is free of contaminations [25]. Therefore, all of the shown configurations should provide strong chemical bonds with epoxy resin based adhesives.
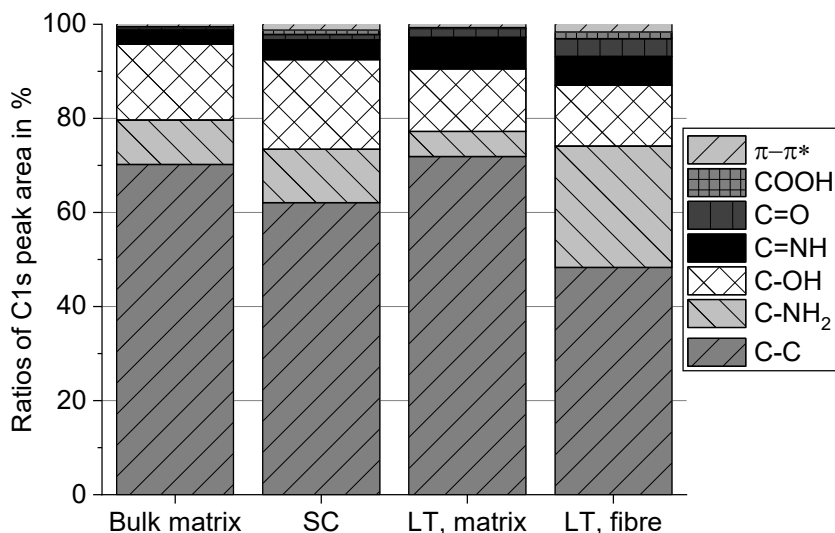
Figure 5.16: Functional composition of the C1s peak for the bulk matrix and milled CFRP after solvent cleaning (SC) and laser treatment (LT).

Because of the superimposed change of the ratio of constituents on the surface, a functionalisation could not be validated. Still, the revealed surface after laser treatment shows a high chemical similarity to electrochemically treated carbon fibres and thus should provide very good adhesive properties.

Comparison of different laser parameter

Similar to the morphological investigation for different laser parameter from Chapter 5.1.2, the effect on the chemistry has been evaluated. A surface of 10×20 mm^2 has been investigated by an area scan, to assess the homogeneity of the surface treatment. Therefore, the result for each laser parameter is an average of approximately 110 point measurements.

Figure 5.17 shows the effect of the pulse energy and the pulse frequency on the elemental composition on the surface. A correlation between the pulse energy and the atomic concentration of all four elements can be observed. Generally, with higher pulse energies, the atomic concentration of carbon increases, while the atomic concentration of the other three elements decreases. As for the change from SC to LT, this could be the result of the removal of epoxy resin on the surface. This is supported by the fact that the laser parameters with a pulse frequency of 200 kHz have the highest degree of stripping (compare Figure 5.5) and also have the highest atomic concentration of carbon. Therefore it could be argued that higher pulse energy provides a higher surface temperature and as a result removes a larger amount of epoxy resin. The same could also be argued for higher pulse frequencies, but in that case, the adjustment of the scan speed and hatch distance apparently influences the effect of the surface treatment.

Overall, the differences between the atomic concentrations are small between the different laser parameter. Keeping in mind the results from the point scans in this chapter, it can be concluded that all surfaces should provide similar suitable chemical bonding properties.
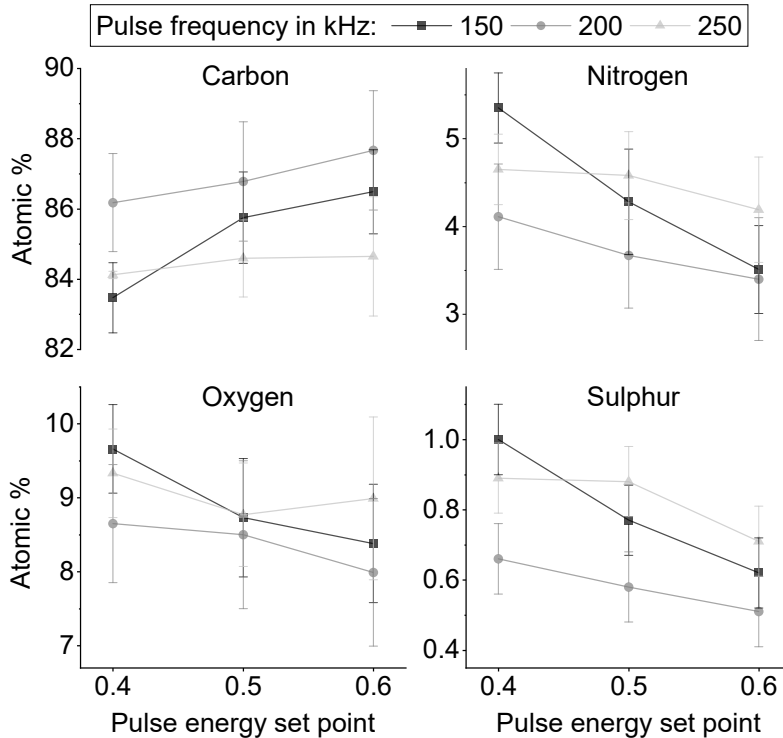
Figure 5.17: Effect of the pulse energy and pulse frequency on the elemental composition on the surface for different laser parameters.

5.3.2 Carbon fibre

The elemental composition on the surface of the carbon fibre bundles can be seen in Figure 5.18. Compared to the elemental composition of the CFRP, no sulphur was found on the surface. This further emphasizes that the sulphur content in Figure 5.14 and Figure 5.17 is a good indicator for the amount of epoxy resin on the surface.

From the composition, a difference between the AR and AC configuration can be observed. The goal of the acetone treatment was to remove the sizing

from the fibre. Therefore, the elemental composition has to be evaluated with regards to that. A sized fibre is associated with higher oxygen and lower nitrogen content compared to an unsized fibre [124,155]. The acetone treatment causes a decrease of the oxygen and a slight increase in the nitrogen content on the surface. Accordingly, it can be concluded that the acetone treatment was able to remove the sizing at least partially. Further decreasing oxygen and increasing nitrogen content can be observed for the AR+LT and AC+LT configuration. Some authors argued that high temperatures are necessary in order to completely decompose the sizing and acetone treatment alone is not sufficient [156].

Figure 5.18: Surface elemental composition of the T700S carbon fibre for the as-received (AR), acetone rinsed (AC) and afterwards laser treated (AR+LT, AC+LT) configuration.

As mentioned in Chapter 5.1.2, the temperature on the surface of the fibre must reach at least 700 °C to sublimate material and change the morphology.

This would be high enough to furthermore sublimate an epoxy resin based sizing.

The C1s spectra of the different configurations in Figure 5.19 show significant differences.

Figure 5.19: C1s spectra of the T700S carbon fibre for the as-received (AR), acetone rinsed (AC) and afterwards laser treated (AR+LT, AC+LT) configuration.

The AR configuration shows a distinctive peak for the C-C bond and the C-OH functional group. For the other configurations, the C-OH peaks seem to diminish in the same order as the decrease of oxygen in the elemental composition. Furthermore, the C-NH₂ peak increases. The AR and AC configurations show a close resemblance with the results of a study by Dai et al. [155]. In the study, a desizing of the T700S fibre was assumed. Given the fact that the C-OH functional group, which is an indicator for the presence of epoxy resin, further decreases after laser treatment, a complete desizing

after acetone treatment seems unlikely. The C1s spectrum of the AC+LT configuration shows a close resemblance with the LT fibre-rich configuration of the CFRP (see Figure 5.15), which means that similar processes must have taken place.

As for the LT fibre-rich configuration, the result of the fibre bundle laser treatment is a chemical state that is similar to the electrochemical surface treatment. Therefore it can be concluded that the presence of the embedding matrix is negligible for the reaction of the fibres. The results of the fibre bundle further support the finding that a laser treatment with such low pulse energies removes the sizing as well as a layer of the fibre. The freshly exposed surface is most likely a result of the electrochemical surface treatment during manufacturing. Given the information depth of the XPS measurement, at least 10 nm of material has to be removed from the surface. Given the thickness of a conventional sizing (~0.03 µm up to 0.5 µm [104]) and the morphological changes observed (see Figure 5.7) it is reasonable to assume that at least 10 nm have been removed from the surface of the fibre.

The quantification of the C1s spectra in Figure 5.20 shows that the gradual removal of the sizing also increases the ratio of C=NH, C=O and COOH functional groups. Especially the increase of COOH functional groups should benefit the adhesion with an epoxy based adhesive, though it is small.

Finally, it is not possible to assess which chemical composition would provide the best adhesive properties. Concerning the influence of the sizing on the fibre/matrix, different views have been stated. While some authors argue that the sole function of the sizing is to protect the fibre against damage for further processing, other authors also observed an increase of the interfacial strength [122,157]. As for the investigation of the CFRP, all fibre bundle configurations show high ratios of functional groups and should therefore generally be suitable for adhesive bonding.
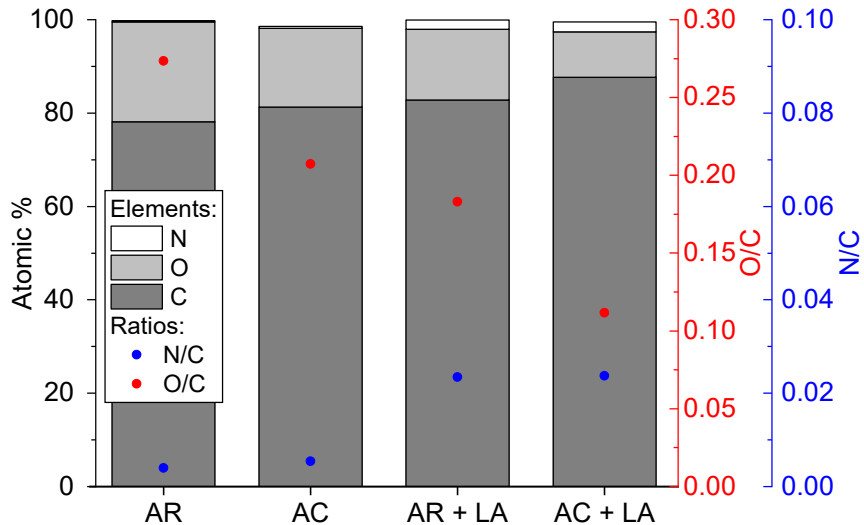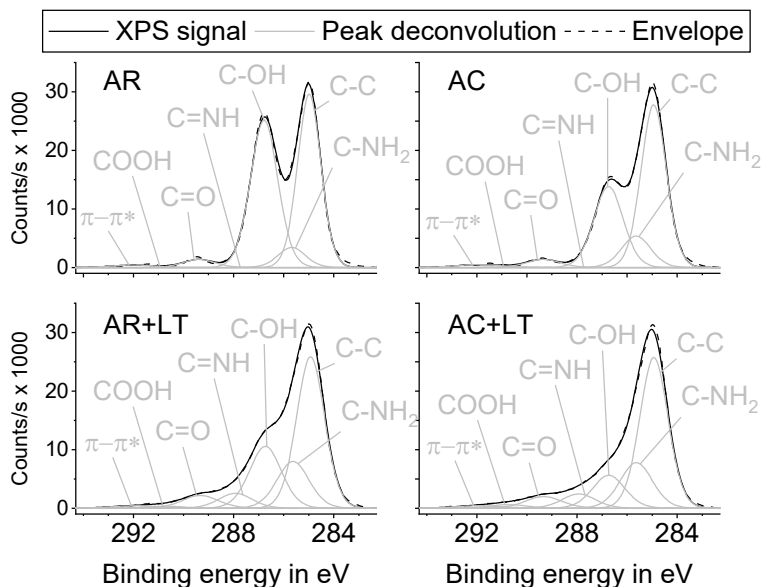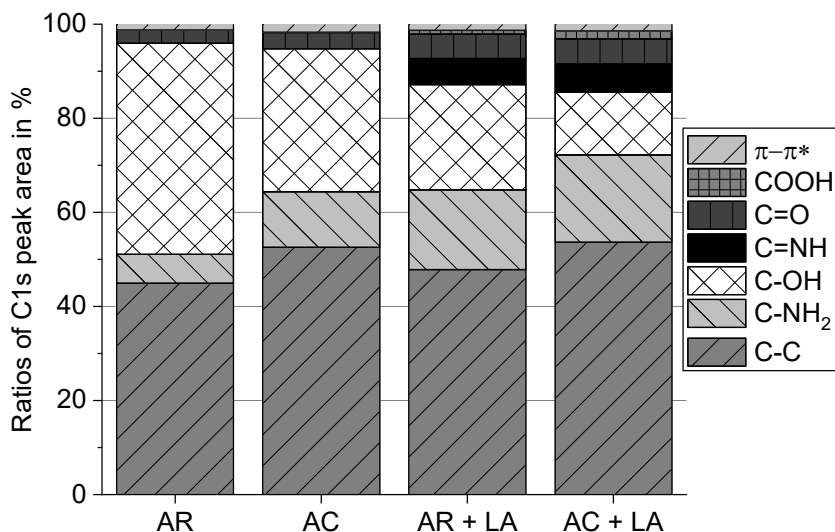
Figure 5.20: Functional composition of the T700S carbon fibre for the as-received (AR), acetone rinsed (AC) and afterwards laser treated (AR+LT, AC+LT) configuration.

5.3.3 Aging of laser-treated CFRP

The ageing of the laser surface treatment was investigated by separate measurements of the same specimen at the same position. The first measurement was taken after one day. This was the normal procedure for all previously mentioned XPS measurements. The second measurement was taken three days, and the third was taken seven days after the laser surface treatment. Specimens were stored under ambient conditions. Figure 5.21 shows the elemental composition of the aforementioned configurations and the SC configuration for reference. Elemental compositions for the different measurement dates are similar, though a slight increase in O/C ratio is

visible. On the other side, this increase is also accompanied by an increase in sulphur, which could be the result of a slight deviation of the measurement point. Though the point of measurement was marked for reference, it cannot be recovered completely. Therefore, the increased sulphur content could indicate that an area with slightly more matrix was investigated. This is also accompanied by an increase of oxygen, as known from the previous investigation of the fibre- and matrix-rich region of the laser treated surface in Chapter 5.3.3.

Figure 5.21: Surface elemental composition for a defined time after the laser treatment (LT) and the solvent cleaned (SC) configuration for reference.

Still, if the increase of oxygen is a result of the ageing, it is not necessarily a weakening effect since an increase of oxygen is generally seen as a positive indicator for the functionality of a surface. As the elemental compositions of

the laser treated configurations, the C1s spectra in Figure 5.22 also show similar shapes. Overall, the shapes very much resemble the fibre-rich regions of the laser treated configuration in Figure 5.15. As matrix-rich regions were significantly smaller, the C1s spectra are dominated by the fibre chemistry, which would explain the similarity to the LT fibre-rich configuration. Therefore, as already mentioned in Chapter 5.3.1 good adhesive properties can be expected. An increase in the C-OH peak can be observed. This could be a result of the aforementioned shift of the measurement spot or an oxidation process. Nevertheless, the shape is largely uninfluenced by the time after laser treatment. As from the C1s spectra, the increase of the C-OH functional group ratio is also visible in Figure 5.23.
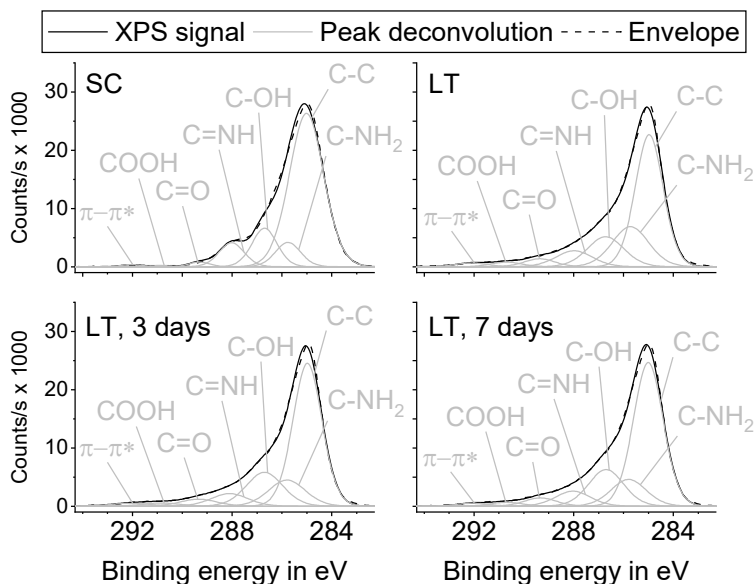
Figure 5.22: C1s spectra for a defined time after the laser treatment (LT) and the solvent cleaned (SC) configuration for reference.

All of the configurations show a high ratio of functional groups of at least 49 %. Furthermore, the ratio for the COOH functional group remains constant during the period of seven days. Overall, the investigated surfaces

show a high functionality. The ageing of the laser treated surface is negligible for the evaluated time. The variation of the elements is in the range of the measurement scatter and therefore no ageing can be expected for the given time. It is thus reasonable to assume that the adhesive properties of the surface should not change and the bonding process can be postponed up to seven days after the laser treatment.

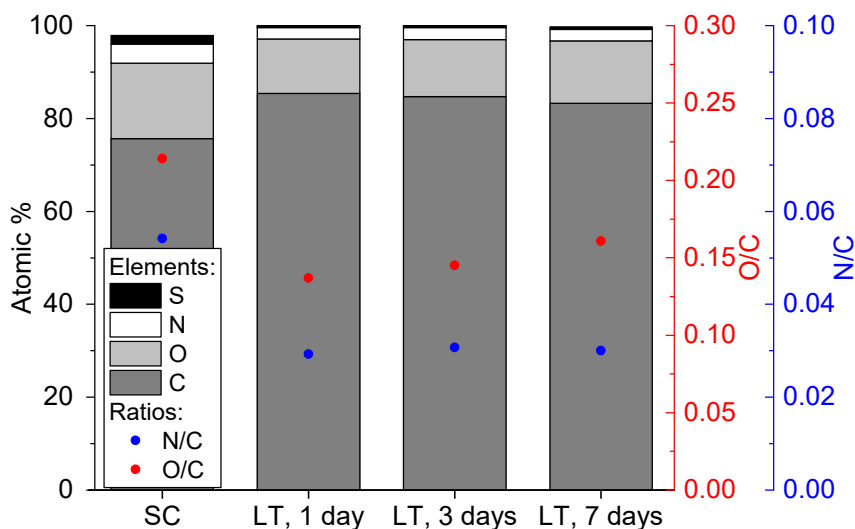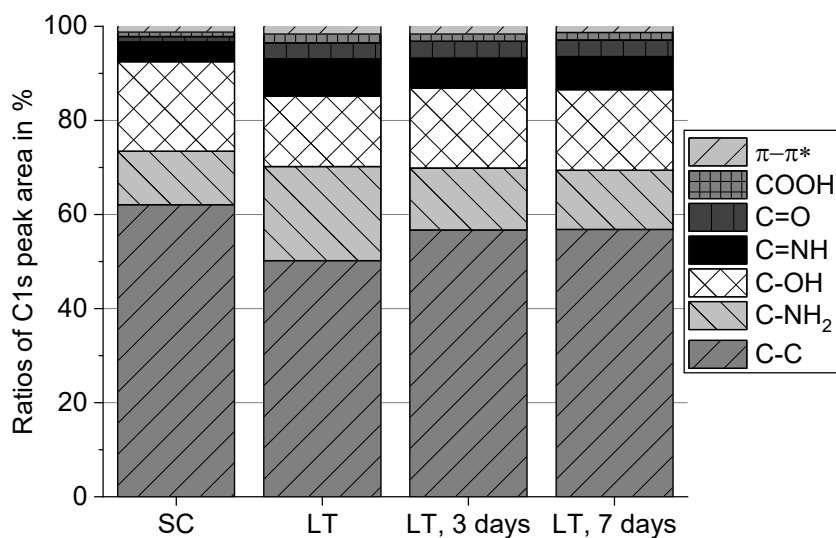Figure 5.23: Functional composition of the C1s spectra for a defined time after the laser treatment (LT) and the solvent cleaned (SC) configuration for reference.

5.4   Wetting behaviour

The wetting behaviour was investigated by a contact angle measurement. Contact angle measurements are often used because of an easy assessment of multiple parameters of the surface since it is influenced by the roughness as well as the chemistry on the surface.

Figure 5.24 shows the static contact angle of the RA, UT, SC and LT configuration.
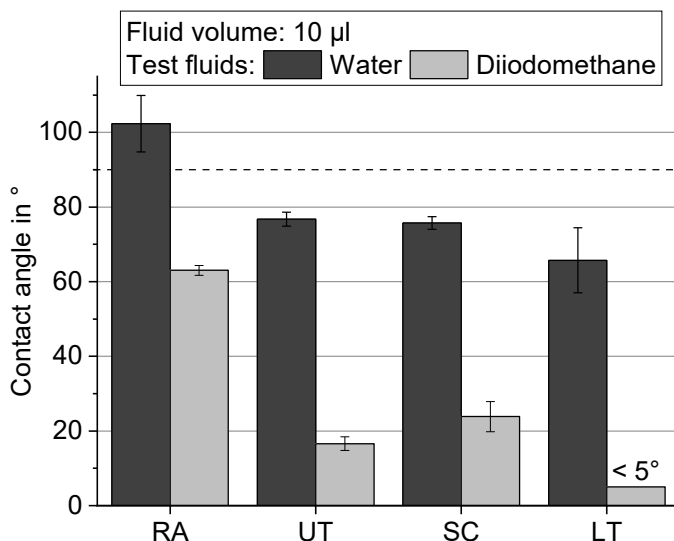
Figure 5.24: Static contact angle for the release agent applied (RA), untreated (UT), solvent cleaned (SC) and laser-treated (LT) configuration of a milled surface.

An angle of 90° is considered to be the threshold for good wetting. Despite the RA configuration, all other configurations show good wetting with water as a test fluid. Since the aim of the RA configuration was to have a reference where poor adhesive properties could be expected, this result shows good agreement. For diiodomethane, even the RA configuration shows good

84

wetting, but still has the highest contact angle among all configurations. Water has a significantly higher polar part of the surface energy than diiodomethane (51.5 mJ/m² compared to 0.4 mJ/m²) and a higher surface energy overall (72.8 mJ/m² compared to 50.8 mJ/m²). Therefore, the larger contact angle of water compared to diiodomethane can be attributed to the high polarity and surface free energy. Comparing the UT, SC and LT configurations the differences in the contact angle are small. The LT configuration shows the lowest contact angle for both test fluids. For diiodomethane, the contact angle could not be measured precisely due to the almost complete spreading of the liquid, as shown in Figure 5.25. Since contact angles above 5° could be evaluated by the software, the contact angle was assumed to be less than 5°.

SC   LT

Figure 5.25: Wetting behaviour of diiodomethane for the solvent cleaned (SC) and laser-treated (LT) configuration.

The resulting surface free energies for the average contact angles calculated by the OWRK method are shown in Figure 5.26. The RA configuration has a significantly lower surface free energy than the other configurations. The other three surface free energies are in the range between 46 mJ/m² and 52 mJ/m². Studies reported a surface free energy between 36.3 mJ/m² up to 39.0 mJ/m² for uncured epoxy resin [66,158]. Therefore, except for the RA configuration, a spreading of the epoxy based adhesive can be expected. Since the surface free energy of a surface is influenced by the chemistry and the surface roughness, both could contribute to the improved wetting of the LT configuration. The LT configuration showed the highest roughness of all. In the case of good wetting, an increase of the roughness will further increase the surface free energy [159]. Therefore, the increased roughness could be an explanation for the higher surface free energy. On the other side, the

chemical composition is also changed for the LT configuration and could also contribute to a higher surface free energy.

The higher surface free energy of the UT compared to the SC configuration is somewhat surprising, given that for the SC configuration a higher surface roughness was measured. Since the chemical composition should be similar on both surfaces, a higher surface free energy would be expected for the SC configuration. A reason for the higher surface free energy of the UT configuration could be the porous surface. While the milling residues do not contribute to the surface roughness, this layer can be penetrated by the test liquids and therefore improves the wetting.
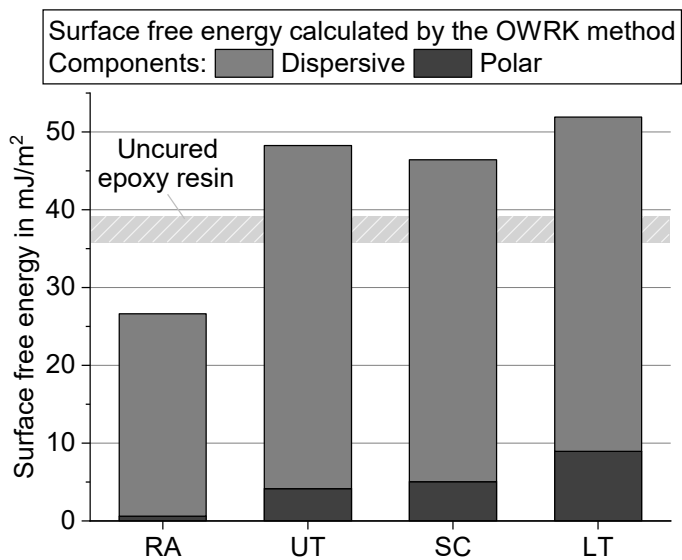
Figure 5.26: Surface free energy calculated with the OWRK method considering the determined average contact angles for the release agent applied (RA), untreated (UT), solvent cleaned (SC) and laser-treated (LT) configuration.

5.5 Carbon fibre surface area measurement

Since morphological investigations qualitatively showed a roughening of the fibre, the surface area of the carbon fibre rovings was quantified by an adsorption measurement. The result of the adsorption measurements and the subsequent evaluation with the BET method are shown in Table 5.1. The theoretical value of the surface area as derived by Figueiredo et al. [160] assumes a consistent cylindrical shape with a diameter of 7 μm and a density of 1.8 g/cm³ according to the datasheet of the T700S carbon fibre.

Table 5.1: Specific surface area of carbon fibre rovings calculated by the BET method.

Configuration	Specific surface area in m^2/g
Theoretical value	0.32
As received (AR)	0.42
As received + laser treated (AR+LT)	0.27

Given the observed roughness of the carbon fibres in Figure 5.7, the measured values appear to be surprising. The results show that the laser-treated fibre (AR+LT) shows the lowest surface area despite the observed roughening in the SEM images. The particles that were observed on the carbon fibre after the laser treatment also appear not to increase the surface area. The measured value for the AR+LT configuration is even lower than the theoretical value. The AR fibre, on the other hand, shows the largest surface area.

For the interpretation of the data, it has to be known that all of the surface area values are on the lower range of the measurable range when using nitrogen (0.2 m^2/g for the used porosimeter). Furthermore, it was known from previous publications that standard deviations up to 2 m^2/g can be expected for this type of measurement [161]. In order to increase precision,

krypton could be used. This was recognised ahead of the measurements. As several authors [160,162] reported a significant increase of the surface area up to 9 m^2/g due to oxidation, the goal of the adsorption measurement was to show whether similar values could be achieved by the laser treatment. The investigation instead showed that the surface area of carbon fibre rovings was mostly unaffected by the laser treatment. A reason for this result could be the treatment length and the temperature achieved during the laser treatment compared to the oxidation treatments used in the cited literature. For the oxidation experiments in a furnace, carbon fibres were treated with air supply and a temperature of 600 °C for a few minutes [162]. The laser treatment is locally limited to a few nanoseconds treatment duration. The temperature can only be estimated by numerical simulations and is in the range of approximately 730 °C, which is not significantly higher than the temperature in the furnace. Due to the difference in the treatment length, that is an order of a few magnitudes higher, the oxidation and therefore, surface area increase in the furnace is more pronounced. The fact that a ratio of the measured fibres remains untreated could further reduce the effect of laser treatment on the measured specific surface area.

On the other side, significant oxidation rates are accompanied by a weakening of the fibre, because material is burned off. Since the surface area and therefore, morphology is mainly unaffected, no significant weakening of the fibre can be expected after the laser treatment. Therefore, the presumably low oxidation rate could also be seen as an advantage since it also indicates that the strength of the carbon fibre is largely unaffected.

5.6 Adhesive scarf bond strength

The mechanical testing aimed to evaluate the effect of the surface treatment on the bond strength as close to the industrial aerospace processes as possible. The scarf bond was chosen for the evaluation of the bond strength because it closely resembles the stress distribution of a composite repair. Furthermore, the processes for the manufacturing of such a bond are very similar a composite repair. The scarf bond has two essential parameters that determine the failure mode, as described in Chapter 2.1. With shallower scarf angles and the presence of 90°-plies the chances of adherend failure increase. For an assessment of the effect of the surface treatment, on the other hand, either adhesive failure or a change of the failure mode for different treatment methods is necessary. Therefore, to prevent adherend failure that would overlay the effect of the surface treatment, a steep scarf angle with a UD lay-up was chosen for the initial investigation. Since the presence of cavities was known from the surface analysis by ion-beam milling (see Chapter 5.1.3) and the absolute size of cavities potentially would increase with shallower scarf angles, the influence of the scarf ratio was investigated in a second step.

Contaminations play a critical role in the performance of bonded joints. While a controlled process should be able to avoid contaminations, the ability of a surface treatment method to remove contaminations can be seen as an evaluation factor. Thus, the third part of the mechanical testing deals with the assessment of the removal of contaminations. Finally, the complexity of the adhesive bond was increased by testing a QI lay-up under static and cyclic loading.

5.6.1 Characterisation of a milled CFRP surface

Figure 5.27 shows the effect of the solvent cleaning and laser treatment on the scarf bond strength for a scarfing ratio of 1:10 and a UD lay-up. The assessment of the bond strength shows that surface treatment improves the bond strength significantly.
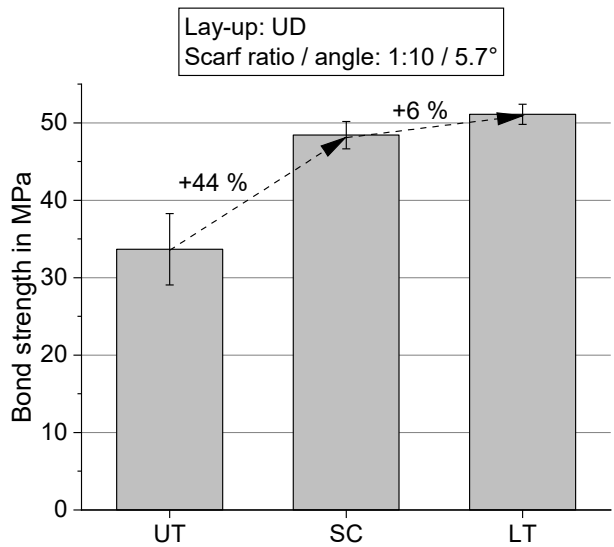
Figure 5.27: Comparison of the effect of surface treatment after milling for the untreated (UT), solvent cleaned (SC) and laser-treated (LT) configuration.

A solvent cleaning already improves the bond strength by 44 % compared to a milled and untreated surface. For laser treatment, a further improvement of 6 % can be observed. An analysis of variance (ANOVA) showed that the improvement of the LT configuration compared to the SC configuration is statistically significant (p-value < 0.05). Furthermore, the SC configuration was tested with 18 specimens from two different panels to account for the complex specimen manufacturing. The bond strengths of both panels

showed no significant difference and were therefore merged for the evaluation.

Both surface treatment methods achieve higher strengths than given in the material data sheet (40.7 MPa single lap shear strength with aluminium adherends and overlap of 12.7 mm [129]). This was partially expected as scarf bonded joints achieve higher strengths than single lap joints with the same overlap [13]. Furthermore, stiffer adherends increase the bond strength as bending and therefore, peel stresses are reduced [163]. On the other hand, the overlap that was applied for the material data sheet was smaller. As the stress concentrations at the scarf and single lap bond endings do not increase proportionally in size with increasing overlap, smaller overlaps exhibit higher strengths when referred to the bonded area [19]. Therefore, the achieved strengths after surface treatment can be considered as high, given the adhesive strength.

The assessment of the fracture surfaces is a fundamental part of the mechanical testing of bonded joints as the specimen can fail at different locations. Therefore, a chain model that was proposed by Reitz et al. [73] was adjusted by adding the repair laminate and implemented for the assessment. Figure 5.28 shows the bond line and the corresponding model with the five elements, each representing a failure location. Though this model is a simplification of the conditions in the bond, since the failure is an aggregate of the stress distribution and the respective strengths at the different locations, it helps to visualize the effect of the surface treatment.

As previously indicated, to examine the effect of surface treatment, two outcomes are required:

1. Adhesive failure at the primary laminate interface (AF Primary in Figure 5.28). This result returns a value for the strength of the interface.
2. A change of the fracture location for different surface treatment methods. The change of the fracture surface includes a shift from adhesive to cohesive failure or adhesive failure at the repair laminate in case of an improvement of the bond strength. In case of a weakening, a cohesive substrate failure of the primary laminate would be visible. This result returns a qualitative statement about the effect of surface treatment.
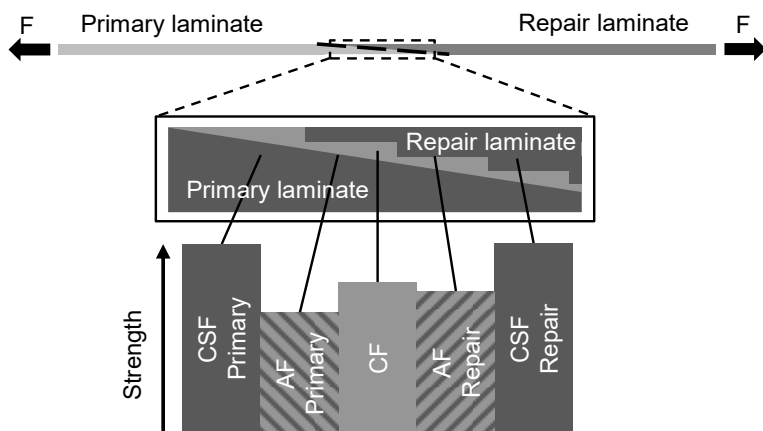
Figure 5.28: Schematic represantantion of the bond line and the model for the assessment of the fracture surface with the assumed strengths for an arbitrary configuration. CSF: cohesive substrate failure, AF: adhesion failure, CF: cohesion failure.

Figure 5.29 shows three representative fracture surfaces of a UT, SC and LT configuration and the corresponding estimated strengths of the elements. CF, AF Repair and CSF Repair are estimated to remain constant because these

elements are not influenced by the surface treatment. For the UT configuration, the overlap length is reduced due to manufacturing reasons. As the scarf angle is the same for all configurations, and the strength refers to the bonded area, the effect on the results should be negligible. The fracture surface of the UT configurations shows almost no residues of adhesive on the primary laminate. The repair laminate, on the other side, is entirely covered by adhesive. As the microscopic investigation in Chapter 5.1.2 showed that significant amounts of milling residues were present on the UT configuration, the surface was additionally investigated in the SEM.
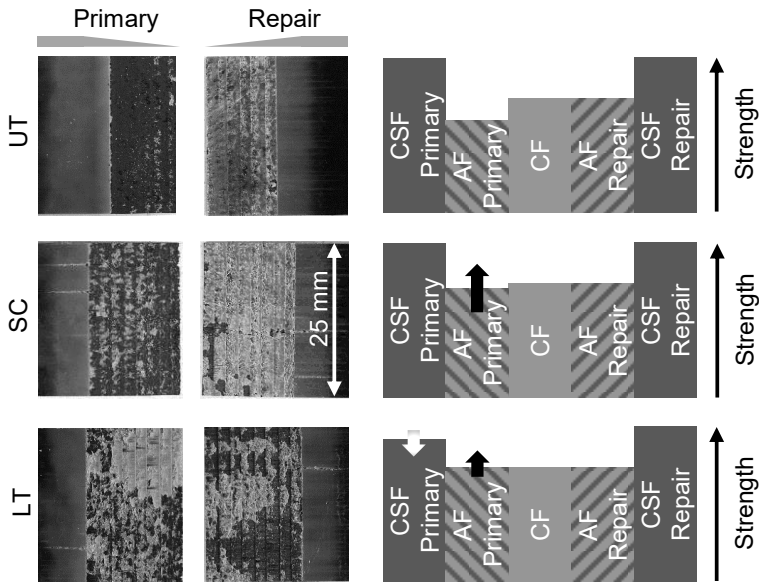
Figure 5.29: Representative fracture surfaces with an estimation of the strengths of the chain model for the untreated (UT), solvent cleaned (SC) and laser-treated (LT) configuration.

Figure 5.30 shows a section of the primary and repair laminate adherend of a UT configuration specimen. The primary laminate side of the fracture surface appears very smooth without any significant amounts of milling residues visible. On the repair laminate side, a rough and smooth section is visible. The rough part could indicate a cohesive failure but also removed milling residues. A definitive distinction is not possible, though it could be argued that similar to the adhesive disc in Figure 5.4, the adhesive peels of remaining milling residues on the primary laminate. This would also explain the comparably low strength as the adhesive is only partially able to bond with the primary laminate.
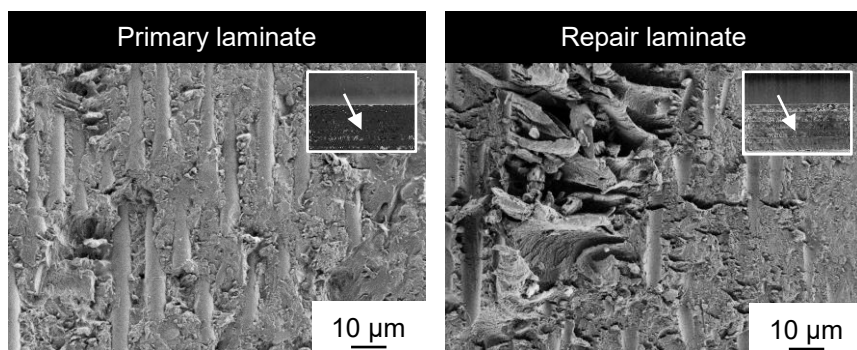
Figure 5.30: SEM images of the fracture surfaces of an untreated (UT) configuration.

The smooth section on the repair laminate shows fibre indentations. The fibre indentations indicate a weak bonding of the adhesive with the fibre. The darker spots on the fracture surface of the repair laminate side were found to be relatively smooth, while brighter parts were rougher. No significant areas with peeled of fibres were found on neither side.

For the surface treated configurations, both show mixed failure. While the solvent cleaned specimen shows predominantly adhesive failure at the primary laminate, for the laser-treated specimen, the failure changes to mainly cohesive and adhesive failure at the secondary laminate. This result supports the finding that the laser surface treatment improves the scarf joint

strength. A decrease in the interlaminar strength for the laser-treated surface due to unfilled cavities is expected and indicated in Figure 5.29. However, no cohesive substrate failure of the primary laminate is observable and thus should not influence the bond strength.

Both, the absence of cohesive substrate failure and the increased strength of the laser-treated configuration, are surprising given that cavities are present. The finding suggests that the strength increasing effects (fibre stripping and roughening) outweigh the influence of the cavities. A reason for the restricted influence of the cavities could be the small size and ratio. The primary laminate material is a unidirectional type prepreg with evenly distributed fibres. Resin-rich areas and the resulting cavities can only be expected between layers and are of limited size (compare Figure 5.1 and Figure 5.2). Therefore, also the effect is expected to be small but could increase for material with larger resin-rich areas like, e.g. plain weave fabric.

The fracture surface of the LT configuration shows a mix of AF primary, CF and AF Repair failure. The complex fracture pattern is partially caused by varying bond thickness. In regions with low thicknesses, a distinction between the failure modes is not always possible. Nevertheless, because of the achieved bond strength and high ratio of CF failure the laser surface treatment can be considered as successful.

As part of the fracture surface assessment, a quantitative method was developed to evaluate the amount of adhesive on the primary laminate after a fracture. The adhesive on the primary laminate can either be related to cohesive or adhesive failure on the repair laminate. Since the interface between the adhesive and repair laminate is not modified, it is a suitable indicator for the surface treatment effect. Figure 5.31 shows the ratio of adhesive on the primary laminate in correlation with the achieved bond strength.
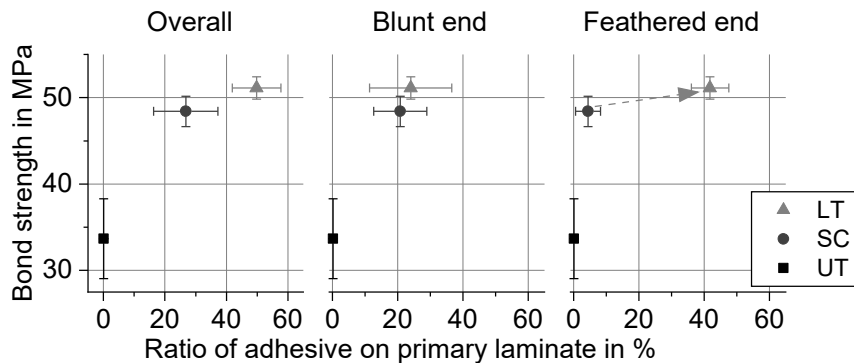
Figure 5.31: Correlation between the bond strength and ratio of adhesive on the primary laminate for the untreated (UT), solvent cleaned (SC) and laser-treated (LT) configuration.

The bond strength and adhesive ratio seem to correlate quite well for the overall bonded surface. The results, therefore, confirm the qualitative observations from the fracture surfaces. Furthermore, the effect can be separated between the blunt ending and feathered ending of the scarf for the SC and LT configuration. While the adhesive ratio is similar for both surface treatments at the blunt end, a significant difference can be observed for the feathered end. The scarf ends are subject to stress peaks. Consequently, the failure may start at the feathered end. As the increase of the bond strength is low compared to the increase of the adhesive ratio, the LT configuration could establish the transition to the preferred cohesive dominated failure.

5.6.2 Influence of the scarf ratio

The influence of the scarf ratio on the effect of the bond strength is shown in Figure 5.32. For this study, only the SC and LT configuration were compared since the goal was to evaluate if the laser treatment could achieve similar results as the established reference process.
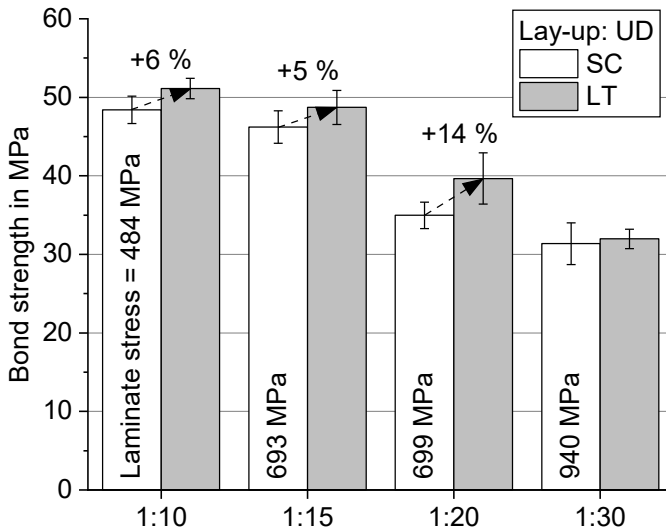
Figure 5.32: Comparison of the bond strength for the solvent cleaned (SC) and laser-treated (LT) configuration for different scarf ratios.

As for the previously shown scarf ratio of 1:10, the LT configuration performs similar or better than the SC configuration in terms of the bond strength. The result shows that the potential increase of cavities does not affect the bond strength negatively. Generally, decreasing bond strength can be observed for an increasing bond area. This is a result of the previously mentioned correlation between the size of the stress peaks and the bond area. Nevertheless, the strength is increased in terms of the laminate stress as shown by the values inside the bars. The laminate stress was estimated by the average maximum force of the SC configuration and the cross-section of the laminate given by the thickness (1.5 mm) and width (25 mm) of the adherend.

For a scarf ratio of 1:30, the difference between the SC and LT configuration was not significant. Additionally, the laminate stress is significantly higher

than for the other scarf ratios. Both observations could indicate an increasing rate of adherend failure. Generally, shallower scarf ratios are associated with an increasing degree of adherend failure [23]. Therefore, in the case of the 1:30 scarf ratio, adherend failure could overlay the effect of surface treatment.
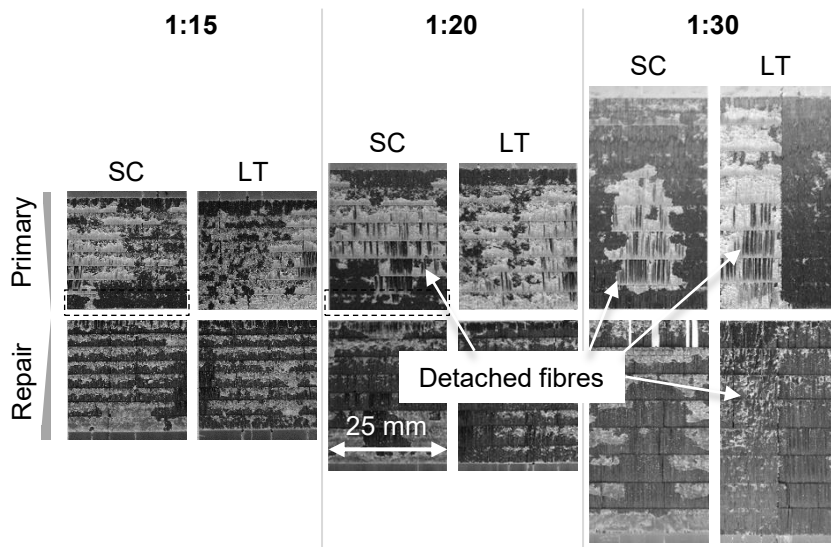
Figure 5.33: Representative fracture surfaces for the solvent cleaned (SC) and laser-treated (LT) configuration with different scarf ratios.

In order to verify this assumption, a UT configuration was additionally tested for the 1:30 scarf ratio. The UT configuration showed a bond strength of 31.5 ± 2.0 MPa, which is between the strength of the SC and LT configuration. Therefore it was concluded, that for a scarf ratio of 1:30, the strength is controlled by the adherend strength. This result also shows the limiting geometrical constraints for an assessment of a surface treatment method for the scarf bond.

Figure 5.33 shows fracture surfaces for the 1:15, 1:20 and 1:30 scarf ratio. Though the tendency of an overall higher adhesive ratio of the LT

configuration is not evident as for the 1:10 scarf ratio, the feathered end shows a significant difference for the 1:15 and 1:20 scarf ratio. The quantitative analysis in Figure 5.34 also confirms the increasing adhesive ratio on the feathered end for the LT configuration. Together with the increased bond strength, this observation further strengthens the assumption that the failure starts at the feathered end of the primary laminate.
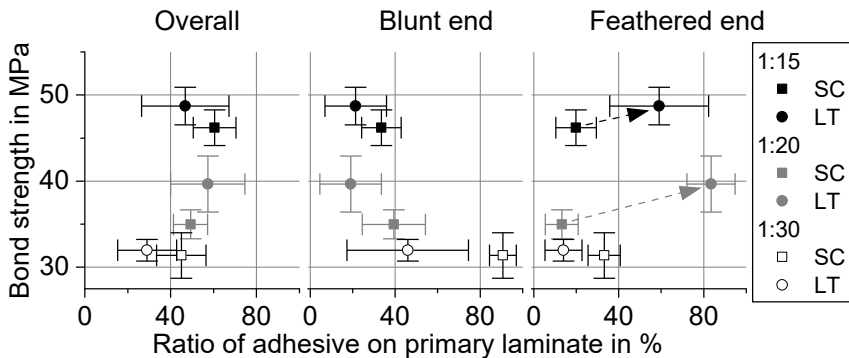
Figure 5.34: Correlation between the bond strength and ratio of adhesive on the primary laminate for the solvent cleaned (SC) and laser-treated (LT) configuration.

Another remarkable observation is an increasing rate of detached fibres from the repair laminate for the 1:20 and 1:30 scarf ratio. The detached fibres generally limit the significance of the quantitative analysis of the adhesive ratio. Since no detached fibres were found on the scarf endings, the quantitative analysis should be valid for these parts. The detached fibres confirm that adherend failure is present for the shallower scarf ratios and that the bond strength is increasingly dominated by this behaviour. Interestingly, for the 1:30 scarf ratio detached fibres from the primary laminate of the LT configuration are also visible. For the SC configuration, no failure of the primary laminate was detected. Consequently, this observation confirms that the primary laminate is weakened by the laser treatment, as

indicated in the chain model in Figure 5.29. The weakening effect seems to be not significant as the bond strength is uninfluenced by it.

As the geometry plays a critical role in the bond performance, cross-sections of the bonded areas have been prepared for every panel. Figure 5.35 shows the representative cross-sections for all four investigated scarf ratios that were prepared from the edges of the panels. Generally, the bond lines show regularly spaced repair laminate plies. This shows that the use of moulds is suitable for the manufacturing of high-quality bond lines for soft-patch repairs. Furthermore, the varying bond line thickness that is a result of the combination of the tapered scarf of the primary laminate and the stepped repair laminate is well visible.

Noticeably, the shallower scarf ratios of 1:20 and 1:30 show a blunt tip and to a lesser degree also the 1:15 scarf ratio. For shallower scarf ratios the thickness and therefore the geometrical stiffness transitions slower than for steeper scarf ratios. As a result, more extended tips with lower thicknesses are produced. The thin tips increase the flexibility and make the manufacturing of sharp tips more difficult. On the other hand, blunt tips cause an increase in the stress concentrations at the scarf endings. This effect increases for shallower scarf ratios [18]. As a consequence, higher bond strengths could be expected for sharper tips. Furthermore, a superimposed effect of the tip bluntness and surface treatment method can be expected. While for the SC and LT configuration, comparable tips were produced, comparability between scarf ratios is aggravated. As the influence of tip bluntness increases for shallower scarf ratios, the significance of the surface treatment decreases. Therefore, adding to the increased adherend failure, the tip bluntness could be a further explanation for the similarity of the bond strength for all three surface configurations of the 1:30 scarf ratio.
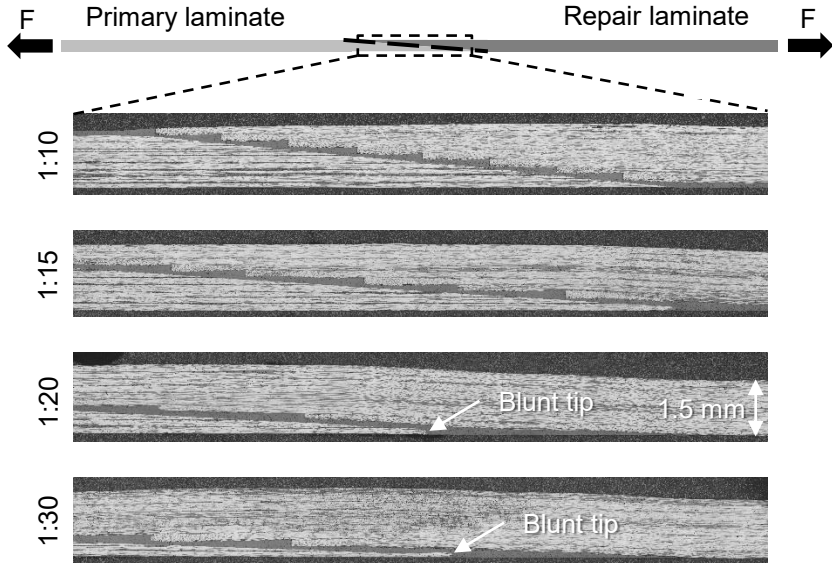
Figure 5.35: Cross-section images of the bond area in the region of the primary laminate feathered tip.

5.6.3 Influence of the laser parameter

The bond strength of the different laser parameter referenced to the SC configuration can be seen in Figure 5.36. The mean bond strength for all laser-treated configurations is higher than that of the SC configuration. The improvement based on the mean values ranges from 2.2 % to 7.6 %. The results indicate that the laser surface treatment improves the strength of the scarf joint, though the improvement is lower than 6 % for most of the laser parameter. No apparent correlation between the laser parameters and the bond strength can be made. Since laser parameter sets modify four process parameters (pulse frequency, pulse energy, hatch distance and scan velocity), a correlation is not straightforward. Modification of all four process parameters, on the other hand, was necessary to prevent process

101

duration-dependent heating of the material. It could rather be concluded that with the used parameter space, similar results can be achieved.

From the SEM images in Figure 5.5, it is apparent that all laser parameters remove milling residues and induce a stripping and roughening of the fibres with slight differences in the degree. Likewise, XPS results in Figure 5.17 show that the chemical compositions are in a similar range for all laser parameters. Consequently, all laser parameters improve the bonding strength compared to the SC configuration. While it is possible that the different laser parameters improve the bonding strength to different degrees, the effect is smaller than the scatter of the test setup. Additionally, as bond strengths appear to be limited by the adhesive, no further improvement is possible.
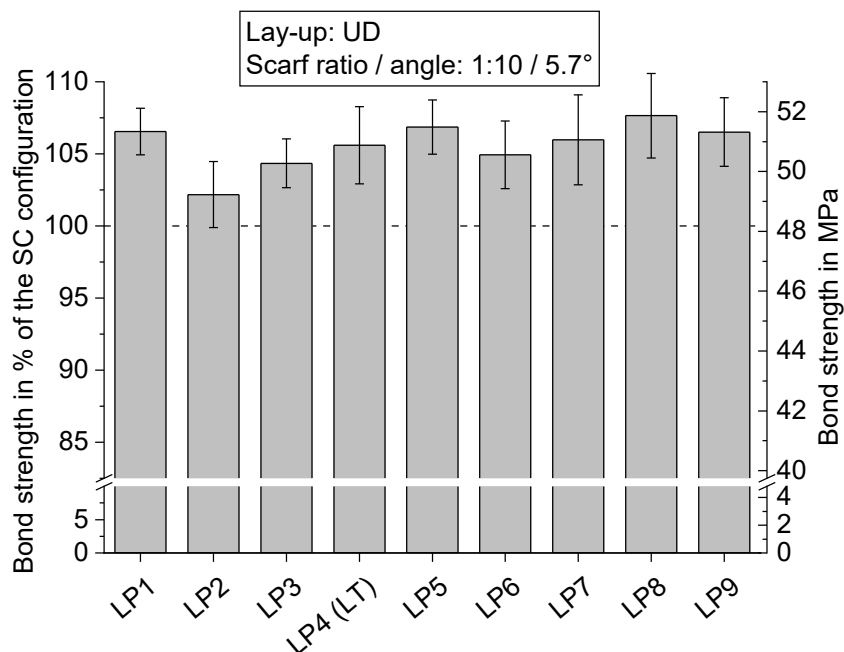
Figure 5.36: Comparison of the effect of different laser parameter on the bond strength in reference to the solvent cleaned (SC) configuration.

5.6.4 Removal of contamination

The ability to remove contaminations was evaluated by the application of release agent and subsequent solvent cleaning or laser treatment. Table 5.2 shows a comparison of the bond strength after surface treatment. The results demonstrate that while the solvent cleaning is not able to remove the release agent and only achieves a bond strength of 0.25 MPa, the laser treatment can restore a notable amount of the bond strength. The remaining difference in the bond strength compared to the results from Chapter 5.6.1 could be a result of a blunt tip, as shown in Figure 5.37.

Table 5.2: Comparison of the cleaning effect of the surface treatment methods after contamination with a release agent.

Configuration	Bond strength in MPa
Solvent cleaned (RA+SC)	0.25 ± 0.1
Laser treated (RA+LT)	43.8 ± 2.7

Figure 5.37: Cross-section image of the bond area showing the blunt tip.

As previously stated, a blunt tip decreases the bond strength for scarf bonded joints. Therefore, the strength values should only be compared for similar scarf endings. Additionally, the evaluation of the fracture surfaces is essential for the interpretation of the surface treatment effect. The comparison of the fracture surfaces is shown in Figure 5.38. A significant difference between the configurations can be observed. After solvent cleaning the primary laminate is very smooth, revealing the effect of the release agent. For laser treatment, a notable amount of adhesive is visible, though a difference between the previously tested LT configuration without prior release agent

application can be observed. The fracture surface suggests that the release agent was potentially not fully removed. On the other hand, the fracture surface is significantly rougher after the laser treatment and the difference compared to the previously tested LT configuration (see Chapter 5.6.1) could also be attributed to the blunt tip. Nevertheless, laser treatment shows a significantly superior ability to remove the release agent compared to isopropanol. Given that release agent is the worst possible type of contamination, because of the effect on the bond strength and the fact that it is not detectable by conventional non-destructive testing methods like ultrasonic scanning, this result is even more impressive. A release agent layer of a few nanometres can be expected [82]. During the stripping of the fibres, this release agent layer or at least the majority is removed.
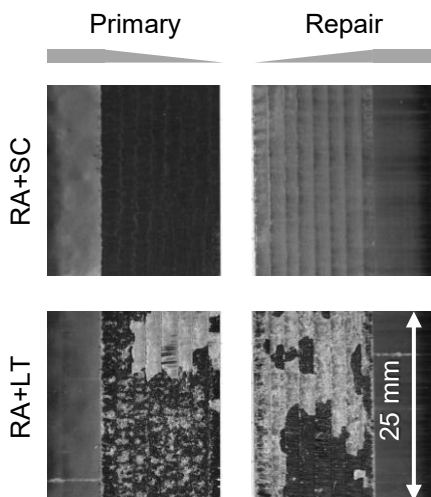
Figure 5.38: Representative fracture surfaces for a solvent cleaned (RA+SC) and laser-treated (RA+LT) after contamination with a release agent.

It could be argued that another solvent type like, e.g. acetone, would be able to remove the release agent. On the other side, different solvents are necessary to remove different contamination types, and therefore all solvents show limitations for certain contamination types. For an improved

104

cleaning effect, a combination of different solvents would be necessary further increasing the process time and complexity. Since laser treatment uses elevated temperature to sublimate the contaminant, it should be able to remove a variety of contamination types in a fast and repeatable process. This finding is very significant and can be seen as one major advantage of laser treatment compared to solvent cleaning.

5.6.5 Quasi-isotropic static and fatigue strength

During the surface analysis of the laser-treated surface, unfilled cavities were discovered. Despite the presence of cavities, the laser treatment improved the bond strength compared to an SC configuration. Aircraft structures are subject to cyclic loading, which could be critical when cavities are present. Therefore, in a conclusive study, the fatigue strength of an SC and LT configuration were compared for a QI lay-up.

For an estimation of fatigue strength of a respective adhesive bond, the static strength is an important parameter. Accordingly, in a first step, the static strength of the adhesive bond with a QI lay-up was evaluated. The results are shown in Table 5.3.

Table 5.3: Static strength for the SC and LT configuration with a QI lay-up.

Configuration	Static strength in MPa
Solvent cleaned (SC)	289.1 ± 27.2
Laser treated (LT)	322.0 ± 9.80

It has to be noted that the strength was evaluated by the thickness and width of the specimen. The overlap length and therefore, the bond strength could not be evaluated precisely because of the complex fracture pattern. The bond strength would result in 28.9 MPa for the SC and 32.2 MPa for the LT configuration, assuming a uniform overlap length of 15 mm. These values are significantly lower than the bond strength for a UD lay-up (compare Chapter 5.6.1) but are reasonable, given that the adherend strength and stiffness is

also considerably smaller. For the static strength, an improvement of 11 % for the LT compared to the SC configuration was determined.

The fatigue strength with respect to the maximum stress during cyclic loading is given in Figure 5.39.
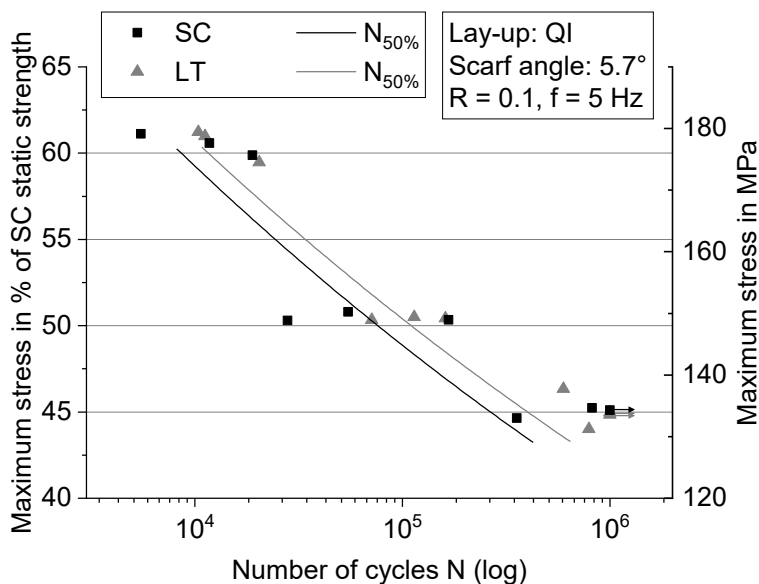
Figure 5.39: Fatigue strength comparison of the solvent cleaned (SC) and laser-treated (LT) configuration.

The maximum stress is in the range of around 50 % of the static strength for 10^5 cycles. For 10^6 cycles or more, the maximum stress is in the range of 45 % of the static strength. These values are significantly better than previously determined values by Yoo et al. [22] (40 % for 10^5 cycles and a scarfing ratio of 1:20), which highlights the quality of the bonding. Three specimens, two for the LT and one for the SC configuration, reached the limit of 10^6 cycles. These specimens are marked by an arrow and not considered for the calculation of the Wöhler line. The determined strengths and Wöhler lines

106

show a slight improvement for the LT configuration within reasonable scatter compared to the literature.

The fracture patterns showed a higher complexity compared to the UD lay-up adherends. Especially the failure of the 90° layer of the repair laminate, as shown in Figure 5.40 needs to be highlighted. Here, the completely detached 90° layer of the repair laminate is visible because of the step in the scarf. The 90° layer has the lowest strength in the loading direction. Furthermore, the ILSS of the repair laminate is around 10 % lower than that of the primary laminate (see Chapter 3.1.1). Therefore, this failure mode appears to be reasonable, though it is not clear whether the failure initiates in that region. Since failure initiation and propagation is a result of the local stress and strength, it is not clear whether the 90° layer is responsible for the resulting bond strength. Given that the strengths between both configurations differ and that the strength of the 90° layer is comparable, this assumption seems unlikely. In order to investigate potential patterns between different configurations despite the failure of the 90° layer, the fracture surfaces were compared for both configurations and load types.
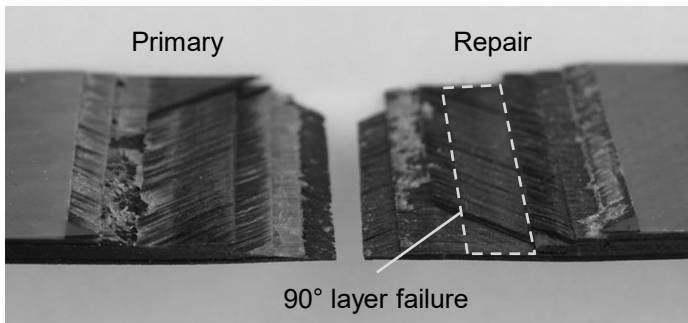
Figure 5.40: Failure of the 90° layer for QI lay-ups.

Representative fracture surfaces are shown in Figure 5.41. At first, no apparent pattern can be derived. It was known from the literature that stress peaks in scarf bonded joints with a QI lay-up are found near the 0° plies. Moreover, from previous mechanical testing of adherends with a UD lay-up,

it was concluded that failure likely initiates near the feathered end of the primary laminate. Therefore special interest was taken into these plies (outlined in Figure 5.41).
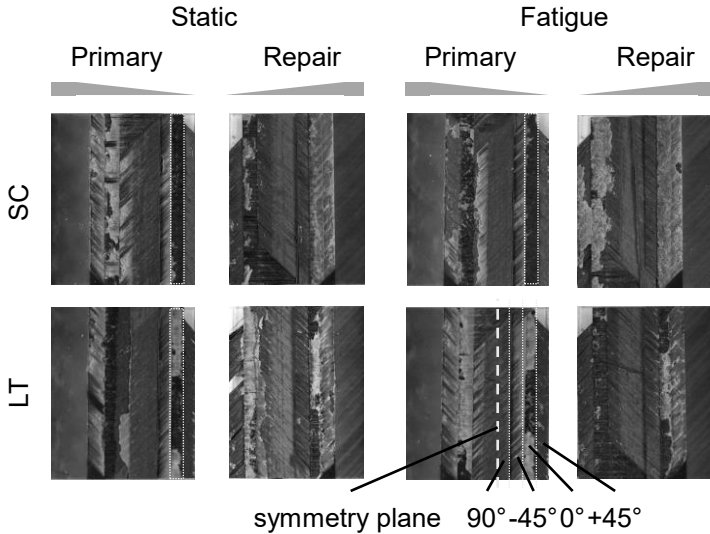
Figure 5.41: Representative fracture surfaces solvent cleaned (SC) and laser-treated (LT) configuration with a QI lay-up.

Here, a difference between both configurations could be spotted. The 0° ply of the SC configuration shows a smooth fracture surface, without any adhesive residues. In contrast, for the LT configuration, a mixed failure can be observed. The difference in the fracture surfaces could, therefore, indicate the improvement of the bond strength of the LT configuration. A difference in the fracture surface patterns near the regions where stress peaks can be expected was already observed for the UD lay-up. Furthermore, the results show that the presence of cavities does not influence the bond strength negatively for static or even cyclic tension-tension loading. It can instead be concluded that the strength improving mechanisms are also valid for cyclic loading and QI lay-ups.

6   Scarfed CFRP surface laser treatment model

Given the comprehensive information of the surface and the resulting bond strength, this section aims to develop a model view of the laser treatment-induced changes and the subsequent effect on the adhesion. Figure 6.1 shows a schematic representation of the major effects of laser treatment, which are explained in more detail in the following part.
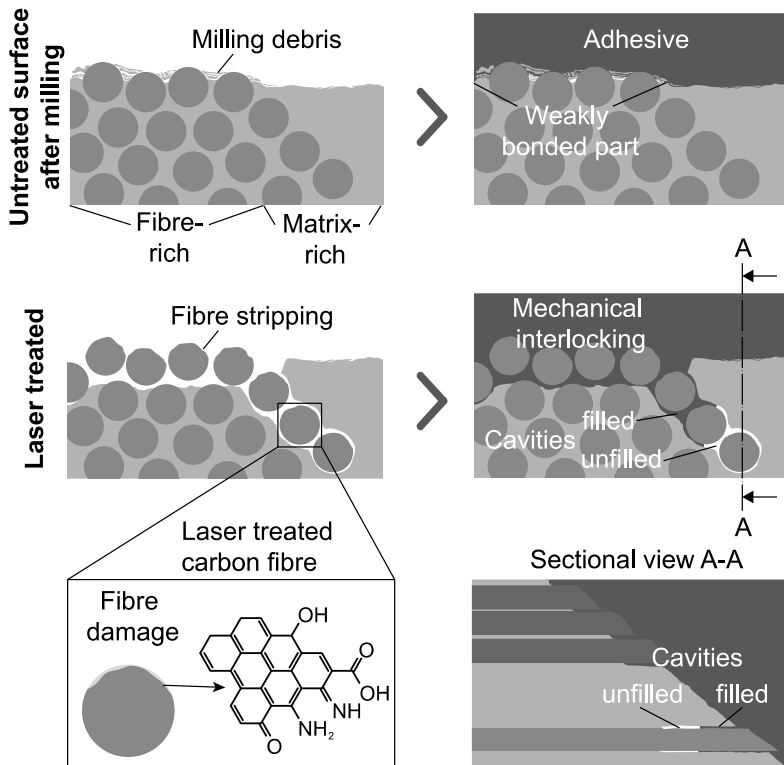
Figure 6.1: Schematic representation of the major effects after laser treatment and the influences on the adhesive properties.

The laser treatment causes a notable change on the surface. As the solvent cleaning, the laser treatment is able to remove the layer of milling debris efficiently. Large agglomerates of milling debris cause a disruption of the interlocking of the adhesive with the load transmitting part of the surface. The milling debris, on the other side, is only poorly attached to the surface and can be easily removed as the adhesive disc experiments showed. Compared to solvent cleaning, the surface is further roughened, and smaller milling particles can be removed. The change is accompanied by a complete circumferential stripping of the fibres. The stripping is evident in the LM, SEM and even roughness measurement. As a result, fibre stripping increases the effective surface area. Therefore, the removal of milling debris and fibre stripping should benefit bond strength. Moreover, as the investigation with contaminated surfaces confirmed, the laser treatment is also able to remove contaminations.

However, laser treatment also introduces cavities under epoxy resin-rich areas. Through the high transmitivity of the epoxy resin in the N-IR range, heat dissipation is only possible on the fibre surface. Hence, epoxy resin can be removed by heating of the fibre, but cannot be targeted directly. In cases where the epoxy resin layer on top is too thick and cannot be removed by the laser, cavities develop. Since fibres run continuously through the material, all cavities can potentially be filled by the adhesive. In practice, the capability to fill cavities is limited by the cavity volume and shape as well as the adhesive viscosity and curing behaviour. As a consequence, unfilled cavities remain in proximity to the surface and pose potential weak points in the bond.

Furthermore, the morphology of the fibre changes after the laser treatment. On the upper part, which is directly affected by the laser, the material is removed slightly reducing the fibre diameter. In addition, the fibre is roughened. The roughening is visible in the SEM, but cannot be confirmed by an adsorption measurement. Thus, the increase of the fibre surface through fibre roughening appears to be minor or not existent. The same can be stated

for particles in the nanometre range that appear on the surface. Because of the small size, a diffusion of the particles into the adhesive is conceivable.

As for the morphology, a significant change in chemistry can be observed after laser treatment. The analysis of the chemical change is complicated due to the simultaneous change of the constituents on the surface. Nevertheless, independent XPS measurements of CFRP and carbon fibre bundles showed that the resulting surface closely resembles an electrochemically treated carbon fibre. This surface shows a variety of functional groups, including carboxyl groups that are particularly important for a good chemical bonding with epoxy resin-based adhesives. The proposed mechanism on the fibre surface is, therefore, the removal of the surface layer, which reveals a reactive surface. This reactive surface is instead a result of the electrochemical treatment of the carbon fibre during their manufacturing than of the laser treatment.

The chemical alteration of the matrix cannot be resolved with the given methods. In the absence of contaminations, an epoxy resin-based adhesive bonds well to an epoxy resin-based matrix. Therefore, the uncertainty about the specific constitution of the matrix does not pose a significant limitation to the surface analysis. This is supported by the fact that the solvent cleaned surface, which is mostly covered by the matrix, also comprises a high ratio of functional groups. Consequently, the laser-treated surface should provide a suitable chemical condition for a good bond. As a result of the favourable chemical constitution and increased surface area, the wetting behaviour is improved compared to the solvent cleaned and untreated surface.

As a consequence, the bond strength can be significantly improved compared to an untreated surface and slightly improved compared to a solvent cleaned surface. The improvement is observed for steeper scarf ratios of 1:10 up to 1:20 and for quasi-isotropic lay-ups under cyclic loading. Therefore, the negative effect of cavities may be limited due to the restricted size and ratio compared to the bonded surface. For shallower scarf ratios, geometrical and adherend properties superimpose the effect of surface treatment. On the other hand, the fracture surface indicates a weakening of the laser-treated

surface, which could be induced by an increase of the cavity size. Nevertheless, the laser-treated configuration performed better for every scarf ratio, lay-up and load type tested. Therefore, the improving effects outweigh the weakening effects.

7   Conclusion

This research has investigated the effects of N-IR surface treatment on the adhesive properties of milled high-performance CFRP. The surface was characterized using different advanced analysis methods. Moreover, scarf joints that represent bonded composite repairs in aerospace were used for the assessment of the effect on the mechanical properties.

The results showed that laser treatment performed better (5-14 % depending on the lay-up and scarf ratio) than the reference process consisting of a solvent cleaning of the surface. Given that the reference process already improves the bond strength by 44 % compared to a milled and untreated surface, this is a remarkable result.

The primary effect of the laser treatment is the removal of milling debris. Milling debris on the untreated surface interrupts the load transfer between the adhesive and the milled surface and reduces the bond strength significantly. Furthermore, the stripping of fibres improves the bond strength compared to the already high standard of the reference process. The driving mechanism is the increase of the roughness and surface area according to the mechanical interlocking theory. The chemical composition shows a high functionality and no contaminations for the reference process as well as the laser treatment and is the foundation of the excellent adhesive properties.

The main downside of the process is the physically induced interaction between the epoxy resin matrix and the N-IR laser and the consequential formation of cavities under matrix-rich areas. Fracture surfaces of shallow scarf ratios with presumably larger cavities indicate a negative impact of cavities though no change was observed for the mechanical properties.

The major advantages of the laser treatment process compared to the reference process are the high surface treatment rates between 1.0 cm^2/s and 7.4 cm^2/s and high level of automation. Furthermore, the possibility to

remove harmful contaminations significantly increases the robustness of the laser treatment process. The change in appearance that is visible with the naked eye and can be used as an indicator of whether the surface has been treated moreover offers a fast process assessment.

Analysis methods used in this work show a good capability for the evaluation of the surface properties but need to be used combined for a proper interpretation of the induced changes. SEM showed very good capability for the observation of the morphology of the surface. Together with ion beam milling, a holistic view of the surface was achieved. Additionally, with roughness measurements, the change could be quantified. Increasing roughness appeared to correlate quite well with increasing bond strength in the absence of any contaminations. With XPS, the chemical composition could be described well, though the change of the ratio of the constituents aggravated a clear statement about the effect. Contact angle measurements were able to differentiate between various configurations and indicate a contaminated surface. A combination of the relatively cheap contact angle and roughness measurement could separate between a contaminated, untreated, solvent cleaned and laser-treated surface and would be suitable for process control.

The scarf bonded joint was generally suitable for the assessment of the effect of surface treatment. Despite the demanding manufacturing, statistically backed statements about the effects were achieved. Only for the shallowest scarf ratio of 1:30, the geometrical effects prevented a clear explanation.

In conclusion, the N-IR laser surface treatment offers a suitable extension to solvent cleaning in cases where a higher degree of automation, robustness and shorter process times are demanded. Therefore, this work contributes to an efficient approach to composite repairs of aircraft structures. The downside of a transmitivity in epoxy resin remains, and additional analyses and mechanical testing is necessary before this method can be applied for other CFRP materials or shallower scarf ratios.

8   Outlook

As indicated in the literature review and conclusion, laser parameters are dependent on the material. In this work, a unidirectional prepreg has been used. Unidirectional prepregs have high fibre volume fractions and a homogenous distribution of fibres. Both properties are excellent preconditions for an N-IR laser treatment. On the other side, fabric prepregs are also used in aerospace structures. Fabrics have lower fibre volume fractions, are less homogenous and as a result, are comprised of larger and thicker epoxy resin-rich areas. The demands on the laser surface treatment, therefore, are higher.

Preliminary experiments that were performed by Lufthansa Technik within the project LABOA showed lower strengths for a laser treatment compared to solvent cleaning for fabric adherends. One reason could be the existence of larger matrix-rich areas and the subsequent increase of connected cavity volume. For these experiments, the same laser treatment approach was chosen as for the unidirectional prepreg. Hence, it would be crucial to investigate if an improvement could be achieved if, e.g. higher energies would be used. While higher energies could also further degrade the fibre and matrix, more matrix could be removed to facilitate the filling of cavities.

Another possibility for the filling of cavities could be the use of lower viscosity adhesives or primer. A rheological study of the FM300 adhesive showed that the applied curing conditions are optimized in terms of viscosity. Since it is challenging to approve another adhesive, the use of an appropriate low viscosity primer could be a suitable solution. In this case, preliminary studies with the compatible primer BR 127 from Solvay showed a complete wetting of the treated surface indicating the potential of this approach. On the other hand, the application of a primer would further increase the complexity of the process, which would counteract the laser treatment approach.

Finally, as this work presented promising findings on the laboratory environment, it would be necessary to confirm the results on the industrial scale. This should include the laser surface treatment of a three-dimensional composite substructure with a multi-directional lay-up. The proposed combination of roughness and contact angle measurement could be used to quantify the surface treatment and compare it to the results achieved in the laboratory environment. Afterwards, the repair patch could be applied, and the substructure should be mechanically tested in order to verify the repair approach.

References

[1]   McConnell VP. Past is prologue for composite repair. Reinforced Plastics 2011;55(6):17–21.

[2]   Airbus. FAST Magazine: Flight Airworthiness Support Technology 2011(48).

[3]   Baker AA, Jones R. Bonded Repair of Aircraft Structures. Dordrecht: Springer Netherlands; 1988.

[4]   Hart-Smith LJ. Bonded-bolted composite joints. Journal of Aircraft 1985;22(11):993–1000.

[5]   Kradinov V, Madenci E, Ambur DR. Combined in-plane and through-the-thickness analysis for failure prediction of bolted composite joints. Composite Structures 2007;77(2):127–47.

[6]   Repair Robot - Aircraft Composites | Lufthansa Technik. [November 18, 2019]; Available from: https://www.lufthansa-technik.com/caire-repair-robot.

[7]   ULTRASONIC mobileBLOCK // ULTRASONIC 85 / 260 / 360. [November 18, 2019]; Available from: https://de.dmgmori.com/news-und-media/fachpresse-news/news/ultrasonic-mobileblock-und-ultrasonic.

[8]   Holtmannspötter J, Czarnecki JV, Feucht F, Wetzel M, Gudladt H-J, Hofmann T et al. On the Fabrication and Automation of Reliable Bonded Composite Repairs. The Journal of Adhesion 2015;91(1-2):39–70.

[9]   Baldan A. Adhesively-bonded joints and repairs in metallic alloys, polymers and composite materials: Adhesives, adhesion theories and surface pretreatment. Journal of Materials Science 2004;39(1):1–49.

[10]   Blass D, Kreling S, Nyga S, Westphalen T, Jungbluth B, Hoffman H-D et al. CFRP bonding pre-treatment with laser radiation of 3 μm wavelength: laser/material interaction. In: Klotzbach U, Washio K, Arnold CB, editors. Laser-based Micro- and Nanoprocessing X: SPIE; 2016, p. 973614.

[11]   Baldan A. Adhesion phenomena in bonded joints. International Journal of Adhesion and Adhesives 2012;38:95–116.

[12] Harman AB, Wang CH. Improved design methods for scarf repairs to highly strained composite aircraft structure. Composite Structures 2006;75(1-4):132–44.

[13] Li J, Yan Y, Zhang T, Liang Z. Experimental study of adhesively bonded CFRP joints subjected to tensile loads. International Journal of Adhesion and Adhesives 2015;57:95–104.

[14] Liu B, Xu F, Feng W, Yan R, Xie W. Experiment and design methods of composite scarf repair for primary-load bearing structures. Composites Part A: Applied Science and Manufacturing 2016;88:27–38.

[15] Goh JY, Georgiadis S, Orifici AC, Wang CH. Effects of bondline flaws on the damage tolerance of composite scarf joints. Composites Part A: Applied Science and Manufacturing 2013;55:110–9.

[16] Wang CH, Gunnion AJ. On the design methodology of scarf repairs to composite laminates. Composites Science and Technology 2008;68(1):35–46.

[17] Baker AA, Chester RJ, Hugo GR, Radtke TC. Scarf repairs to highly strained graphite/epoxy structure. International Journal of Adhesion and Adhesives 1999;19(2-3):161–71.

[18] Adkins DW, Byron Pipes R. End effects in scarf joints. Composites Science and Technology 1985;22(3):209–21.

[19] Campilho RDSG, Moura MFSF de, Domingues JJMS. Stress and failure analyses of scarf repaired CFRP laminates using a cohesive damage model. Journal of Adhesion Science and Technology 2007;21(9):855–70.

[20] Bendemra H, Compston P, Crothers PJ. Optimisation study of tapered scarf and stepped-lap joints in composite repair patches. Composite Structures 2015;130:1–8.

[21] Hayes-Griss JM, Gunnion AJ, Afaghi Khatibi A. Damage tolerance investigation of high-performance scarf joints with bondline flaws under various environmental, geometrical and support conditions. Composites Part A: Applied Science and Manufacturing 2016;84:246–55.

[22] Yoo J-S, Truong V-H, Park M-Y, Choi J-H, Kweon J-H. Parametric study on static and fatigue strength recovery of scarf-patch-repaired composite laminates. Composite Structures 2016;140:417–32.

118

[23] Kumar SB, Sridhar I, Sivashanker S, Osiyemi SO, Bag A. Tensile failure of adhesively bonded CFRP composite scarf joints. Materials Science and Engineering: B 2006;132(1-2):113–20.

[24] Johnson CL. Effect of ply stacking sequence on stress in a scarf joint. AIAA Journal 1989;27(1):79–86.

[25] Banea MD, da Silva LFM. Adhesively bonded joints in composite materials: An overview. Proceedings of the IMechE 2016;223(1):1–18.

[26] Matta S, M. R. Prediction of mechanical behaviour of adhesively bonded CFRP scarf jointed specimen under tensile loading using localised DIC and CZM. International Journal of Adhesion and Adhesives 2019;89:88–108.

[27] Gunnion AJ, Herszberg I. Parametric study of scarf joints in composite structures. Composite Structures 2006;75(1-4):364–76.

[28] Xiaoquan C, Baig Y, Renwei H, Yujian G, Jikui Z. Study of tensile failure mechanisms in scarf repaired CFRP laminates. International Journal of Adhesion and Adhesives 2013;41:177–85.

[29] Ellert F, Bradshaw I, Steinhilper R. Major Factors Influencing Tensile Strength of Repaired CFRP-samples. Procedia CIRP 2015;33:275–80.

[30] Karpat Y, Bahtiyar O, Değer B. Mechanistic force modeling for milling of unidirectional carbon fiber reinforced polymer laminates. International Journal of Machine Tools and Manufacture 2012;56:79–93.

[31] Ahmad J. Machining of Polymer Composites. Boston, MA: Springer US; 2009.

[32] Hintze W, Hartmann D, Schubert U. Stirnfräsen von CFK zur Fügeflächenherstellung und Reparaturvorbereitung. ZWF 2012;107(6):462–6.

[33] Li M, Huang M, Jiang X, Kuo C-l, Yang X. Study on burr occurrence and surface integrity during slot milling of multidirectional and plain woven CFRPs. Int J Adv Manuf Technol 2018;97(1-4):163–73.

[34] Voß R, Henerichs M, Kuster F, Wegener K. Chip Root Analysis after Machining Carbon Fiber Reinforced Plastics (CFRP) at Different Fiber Orientations. Procedia CIRP 2014;14:217–22.

[35]   Wang C, Liu G, An Q, Chen M. Occurrence and formation mechanism of surface cavity defects during orthogonal milling of CFRP laminates. Composites Part B: Engineering 2017;109:10–22.

[36]   Wang DH, Ramulu M, d. Arola. Orthogonal cutting mechanisms of graphite/epoxy composite. Part II: multi-directional laminate. International Journal of Machine Tools and Manufacture 1995;35(12):1639–48.

[37]   Hintze W, Hartmann D. Modeling of Delamination During Milling of Unidirectional CFRP. Procedia CIRP 2013;8:444–9.

[38]   Koplev A, Lystrup A, Vorm T. The cutting process, chips, and cutting forces in machining CFRP. Composites 1983;14(4):371–6.

[39]   Kaneeda T, Takahashi M. CFRP cutting mechanism. (1st report). Surface generation mechanism at very low cutting speeds. Journal of the Japan Society for Precision Engineering 1989;55(8):1456–61.

[40]   Hintze W, Hartmann D, Schütte C. Occurrence and propagation of delamination during the machining of carbon fibre reinforced plastics (CFRPs) – An experimental study. Composites Science and Technology 2011;71(15):1719–26.

[41]   Wang DH, Ramulu M, d. Arola. Orthogonal cutting mechanisms of graphite/epoxy composite. Part I: unidirectional laminate. International Journal of Machine Tools and Manufacture 1995;35(12):1623–38.

[42]   Voss R, Seeholzer L, Kuster F, Wegener K. Influence of fibre orientation, tool geometry and process parameters on surface quality in milling of CFRP. CIRP Journal of Manufacturing Science and Technology 2017;18:75–91.

[43]   Pecat O, Rentsch R, Brinksmeier E. Influence of Milling Process Parameters on the Surface Integrity of CFRP. Procedia CIRP 2012;1:466–70.

[44]   Haddad M, Zitoune R, Eyma F, Castanie B. Study of the surface defects and dust generated during trimming of CFRP: Influence of tool geometry, machining parameters and cutting speed range. Composites Part A: Applied Science and Manufacturing 2014;66:142–54.

[45]   Boatman ES, d. Covert, d. Kalman, d. Luchtel, Omenn GS. Physical, morphological, and chemical studies of dusts derived from the machining of composite-epoxy materials. Environmental Research 1988;45(2):242–55.

120

[46] Freese J de, Holtmannspötter J, Raschendorfer S, Hofmann T. End milling of Carbon Fiber Reinforced Plastics as surface pretreatment for adhesive bonding – effect of intralaminar damages and particle residues. The Journal of Adhesion 2018;118(2):1–19.

[47] Reisgen U, Schiebahn A, Marx B, Schoft J, Ringler K. Reparieren statt Ersetzen. Kunststoffe 2018(2):23–6.

[48] Doobe M. Kunststoffe erfolgreich kleben. Wiesbaden: Springer Fachmedien Wiesbaden; 2018.

[49] Emonts M, Fischer K, Schmitt S, Schares RL. Modelling of Indirect Laser-induced Thin-film Ablation of Epoxy for Local Exposing of Carbon Fibers. Physics Procedia 2016;83:1347–56.

[50] Fischer F, Romoli L, Kling R. Laser-based repair of carbon fiber reinforced plastics. CIRP Annals - Manufacturing Technology 2010;59(1):203–6.

[51] Garrison BJ, Srinivasan R. Laser ablation of organic polymers: Microscopic models for photochemical and thermal processes. Journal of Applied Physics 1985;57(8):2909–14.

[52] Takahashi K, Tsukamoto M, Masuno S, Sato Y. Heat conduction analysis of laser CFRP processing with IR and UV laser light. Composites Part A: Applied Science and Manufacturing 2016;84:114–22.

[53] Sato H, Nishio S. Polymer laser photochemistry, ablation, reconstruction, and polymerization. Journal of Photochemistry and Photobiology C: Photochemistry Reviews 2001;2(2):139–52.

[54] Ohkubo T, Tsukamoto M, Sato Y. Numerical simulation of combustion effects during laser processing of carbon fiber reinforced plastics. Appl. Phys. A 2016;122(3):603.

[55] Ohkubo T, Sato Y, Matsunaga E-i, Tsukamoto M. Three-dimensional numerical simulation during laser processing of CFRP. Applied Surface Science 2017;417:104–7.

[56] Ohkubo T, Sato Y, Matsunaga E-i, Tsukamoto M. Thermal effect of laser ablation on the surface of carbon fiber reinforced plastic during laser processing. Appl. Phys. A 2018;124(2):603608.

121

[57] Djurišić AB, Li EH. Optical properties of graphite. Journal of Applied Physics 1999;85(10):7404–10.

[58] Goeke A, Emmelmann C. Influence of laser cutting parameters on CFRP part quality. Physics Procedia 2010;5:253–8.

[59] Sheng P, Chryssolouris G. Theoretical Model of Laser Grooving for Composite Materials. Journal of Composite Materials 1995;29(1):96–112.

[60] Pagano N, Ascari A, Liverani E, Donati L, Campana G, Fortunato A. Laser Interaction with Carbon Fibre Reinforced Polymers. Procedia CIRP 2015;33:423–7.

[61] Hartwig A, Vitr G, Dieckhoff S, Hennemann O-D. Surface treatment of an epoxy resin by CO2 laser irradiation. Angew. Makromol. Chemie 1996;238(1):177–89.

[62] Herzog D, Jaeschke P, Meier O, Haferkamp H. Investigations on the thermal effect caused by laser cutting with respect to static strength of CFRP. International Journal of Machine Tools and Manufacture 2008;48(12-13):1464–73.

[63] Rauh B, Kreling S, Kolb M, Geistbeck M, Boujenfa S, Suess M et al. UV-laser cleaning and surface characterization of an aerospace carbon fibre reinforced polymer. International Journal of Adhesion and Adhesives 2018;82:50–9.

[64] Encinas N, Oakley BR, Belcher MA, Blohowiak KY, Dillingham RG, Abenojar J et al. Surface modification of aircraft used composites for adhesive bonding. International Journal of Adhesion and Adhesives 2014;50:157–63.

[65] Botana-Galvín M, Blanco G, González-Rovira L, Rodríguez MA, Botana FJ. Adhesive behaviour of carbon fibre reinforced plastic panels manufactured using woven and unidirectional tape after ultraviolet laser surface treatment. Journal of Composite Materials 2018;52(7):853–65.

[66] Boerio FJ, Roby B, Dillingham RG, Bossi RH, Crane RL. Effect of Grit-Blasting on the Surface Energy of Graphite/Epoxy Composites. The Journal of Adhesion 2006;82(1):19–37.

[67] Zaldivar RJ, Nokes JP, Steckel GL, Kim HI, Morgan BA. The Effect of Atmospheric Plasma Treatment on the Chemistry, Morphology and Resultant

Bonding Behavior of a Pan-Based Carbon Fiber-Reinforced Epoxy Composite. Journal of Composite Materials 2010;44(2):137–56.

[68] Chin JW, Wightman JP. Surface characterization and adhesive bonding of toughened bismaleimide composites. Composites Part A: Applied Science and Manufacturing 1996;27(6):419–28.

[69] Parker BM, Waghorne RM. Surface pretreatment of carbon fibre-reinforced composites for adhesive bonding. Composites 1982;13(3):280–8.

[70] Schweizer M, Meinhard D, Ruck S, Riegel H, Knoblauch V. Adhesive bonding of CFRP: a comparison of different surface pre-treatment strategies and their effect on the bonding shear strength. Journal of Adhesion Science and Technology 2017;31(23):2581–91.

[71] Fischer F, Kreling S, Jäschke P, Frauenhofer M, Kracht D, Dilger K. Laser Surface Pre-Treatment of CFRP for Adhesive Bonding in Consideration of the Absorption Behaviour. The Journal of Adhesion 2012;88(4-6):350–63.

[72] AMS CACRC Commercial Aircraft Composite Repair Committee. Masking and Cleaning of Epoxy and Polyester Matrix Thermosetting Composite Materials. 400 Commonwealth Drive, Warrendale, PA, United States: SAE International. doi:10.4271/ARP4916.

[73] Reitz V, Meinhard D, Ruck S, Riegel H, Knoblauch V. A comparison of IR- and UV-laser pretreatment to increase the bonding strength of adhesively joined aluminum/CFRP components. Composites Part A: Applied Science and Manufacturing 2017;96:18–27.

[74] Zhan X, Gao C, Lin W, Gu C, Sun W, Wei Y. Laser Cleaning Treatment and its Influence on the Surface Microstructure of CFRP Composite Material. J Powder Metall Min 2017;06(01).

[75] Gude MR, Prolongo SG, Ureña A. Adhesive bonding of carbon fibre/epoxy laminates: Correlation between surface and mechanical properties. Surface and Coatings Technology 2012;207:602–7.

[76] Li S, Sun T, Liu C, Yang W, Tang Q. A study of laser surface treatment in bonded repair of composite aircraft structures. R Soc Open Sci 2018;5(3):171272.

[77] Jölly I, Schlögl S, Wolfahrt M, Pinter G, Fleischmann M, Kern W. Chemical functionalization of composite surfaces for improved structural bonded repairs. Composites Part B: Engineering 2015;69:296–303.

[78] Park Y-B, Song M-G, Kim J-J, Kweon J-H, Choi J-H. Strength of carbon/epoxy composite single-lap bonded joints in various environmental conditions. Composite Structures 2010;92(9):2173–80.

[79] Song M-G, Kweon J-H, Choi J-H, Byun J-H, Song M-H, Shin S-J et al. Effect of manufacturing methods on the shear strength of composite single-lap bonded joints. Composite Structures 2010;92(9):2194–202.

[80] Morgan BA, Zaldivar RJ, Kim HI, Steckel GL, Chaney JA, Nokes JP. Effect of isopropanol rinse on adhesion of plasma-treated carbon-fiber reinforced epoxy composites. Journal of Composite Materials 2011;45(12):1331–6.

[81] Zaldivar RJ, Kim HI, Steckel GL, Nokes JP, Morgan BA. Effect of Processing Parameter Changes on the Adhesion of Plasma-treated Carbon Fiber Reinforced Epoxy Composites. Journal of Composite Materials 2010;44(12):1435–53.

[82] Dighton C, Rezai A, Ogin SL, Watts JF. Atmospheric plasma treatment of CFRP composites to enhance structural bonding investigated using surface analytical techniques. International Journal of Adhesion and Adhesives 2019;91:142–9.

[83] Zaldivar RJ, Nokes JP, Patel DN, Morgan BA, Steckel G, Kim HI. Effect of using oxygen, carbon dioxide, and carbon monoxide as active gases in the atmospheric plasma treatment of fiber-reinforced polycyanurate composites. J Appl Polym Sci 2012;125(4):2510–20.

[84] Williams TS, Yu H, Yeh P-C, Yang J-M, Hicks RF. Atmospheric pressure plasma effects on the adhesive bonding properties of stainless steel and epoxy composites. Journal of Composite Materials 2013;48(2):219–33.

[85] Li H, Liang H, He F, Huang Y, Wan Y. Air dielectric barrier discharges plasma surface treatment of three-dimensional braided carbon fiber reinforced epoxy composites. Surface and Coatings Technology 2009;203(10-11):1317–21.

[86] Sánchez Serrano J, Ureña A, Lazcano Ureña S, Blanco Varela T. New approach to surface preparation for adhesive bonding of aeronautical composites:

124

atmospheric pressure plasma. Studies on the pretreatment lifetime and durability of the bondline. Composite Interfaces 2015;22(8):731–42.

[87] Bénard Q, Fois M, Grisel M, Laurens P. Surface treatment of carbon/epoxy and glass/epoxy composites with an excimer laser beam. International Journal of Adhesion and Adhesives 2006;26(7):543–9.

[88] Zhan X, Chen S, Li Y, Wang H, Yang Y. Effect of surface cold ablation on shear strength of CFRP adhesively bonded joint after UV laser treatment. International Journal of Adhesion and Adhesives 2019;94:13–23.

[89] See TL, Liu Z, Cheetham S, Dilworth S, Li L. Laser abrading of carbon fibre reinforced composite for improving paint adhesion. Appl. Phys. A 2014;117(3):1045–54.

[90] Yang W, Sun T, Cao Y, Li S, Liu C, Tang Q. Laser-Based Surface Modification of Microstructure for Carbon Fiber-Reinforced Plastics. Lasers Manuf. Mater. Process. 2018;5(2):168–81.

[91] Fischer F, Kreling S, Dilger K. Surface Structuring of CFRP by using Modern Excimer Laser Sources. Physics Procedia 2012;39:154–60.

[92] Kreling S, Fischer F, Delmdahl R, Gäbler F, Dilger K. Analytical Characterization of CFRP Laser Treated by Excimer Laser Radiation. Physics Procedia 2013;41:282–90.

[93] Palmieri FL, Belcher MA, Wohl CJ, Blohowiak KY, Connell JW. Laser ablation surface preparation for adhesive bonding of carbon fiber reinforced epoxy composites. International Journal of Adhesion and Adhesives 2016;68:95–101.

[94] Fischer F, Kreling S, Gäbler F, Delmdahl R. Using excimer lasers to clean CFRP prior to adhesive bonding. Reinforced Plastics 2013;57(5):43–6.

[95] Moreira RDF, Oliveira V, Silva FGA, Vilar R, Moura MFSF de. Influence of femtosecond laser treated surfaces on the mode I fracture toughness of carbon-epoxy bonded joints. International Journal of Adhesion and Adhesives 2018;82:108–13.

[96] Genna S, Leone C, Ucciardello N, Giuliani M. Increasing adhesive bonding of carbon fiber reinforced thermoplastic matrix by laser surface treatment. Polym Eng Sci 2017;57(7):685–92.

[97]   Schmutzler H, Popp J, Büchter E, Wittich H, Schulte K, Fiedler B. Improvement of bonding strength of scarf-bonded carbon fibre/epoxy laminates by Nd: YAG laser surface activation. Composites Part A: Applied Science and Manufacturing 2014;67:123–30.

[98]   Sun C, Min J, Lin J, Wan H, Yang S, Wang S. The effect of laser ablation treatment on the chemistry, morphology and bonding strength of CFRP joints. International Journal of Adhesion and Adhesives 2018;84:325–34.

[99]   Völkermeyer F, Jaeschke P, Stute U, Kracht D. Laser-based modification of wettablility for carbon fiber reinforced plastics. Appl. Phys. A 2013;112(1):179–83.

[100] Kreling S, Blass D, Fischer F, Dilger K. CFRP bonding pre-treatment using M-IR laser radiation. 20th International Conference on Composite Materials 2015.

[101] Bora MÖ, Akman E, Çoban O, Genc Oztoprak B, Demir A. The Effect of CO_2 Laser-Induced Microhole Formations on Adhesive Bonding Strength of CFRP/CFRP Joints. Polym. Compos. 2019;40(7):2891–900.

[102] Tao R, Alfano M, Lubineau G. Laser-based surface patterning of composite plates for improved secondary adhesive bonding. Composites Part A: Applied Science and Manufacturing 2018;109:84–94.

[103] Hughes JDH. The carbon fibre/epoxy interface—A review. Composites Science and Technology 1991;41(1):13–45.

[104] Tang L-G, Kardos JL. A review of methods for improving the interfacial adhesion between carbon fiber and polymer matrix. Polym. Compos. 1997;18(1):100–13.

[105] Drzal LT, Rich MJ, Koenig MF, Lloyd PF. Adhesion of Graphite Fibers to Epoxy Matrices: II. The Effect of Fiber Finish. The Journal of Adhesion 1983;16(2):133–52.

[106] Drzal LT, Rich MJ, Lloyd PF. Adhesion of Graphite Fibers to Epoxy Matrices: I. The Role of Fiber Surface Treatment. The Journal of Adhesion 1983;16(1):1–30.

[107] Al Aiti M, Jehnichen D, Fischer D, Brünig H, Heinrich G. On the morphology and structure formation of carbon fibers from polymer precursor systems. Progress in Materials Science 2018;98:477–551.

126

[108] Ehrburger P, Louys F, Lahaye J. The concept of active sites applied to the study of carbon reactivity. Carbon 1989;27(3):389–93.

[109] Dawson EA, Parkes GMB, Barnes PA, Chinn MJ, Pears LA, Hindmarsh CJ. A study of evolved gas control and its effect on carbon yield during the activation of carbon fibres by controlled rate methods. Carbon 2002;40(15):2897–903.

[110] Ismail IMK. Structure and active surface area of carbon fibers. Carbon 1987;25(5):653–62.

[111] Paiva MC, Bernardo CA, Nardin M. Mechanical, surface and interfacial characterisation of pitch and PAN-based carbon fibres. Carbon 2000;38(9):1323–37.

[112] Moosburger-Will J, Jäger J, Strauch J, Bauer M, Strobl S, Linscheid FF et al. Interphase formation and fiber matrix adhesion in carbon fiber reinforced epoxy resin: Influence of carbon fiber surface chemistry. Composite Interfaces 2016;24(7):691–710.

[113] Qian X, Chen L, Huang J, Wang W, Guan J. Effect of carbon fiber surface chemistry on the interfacial properties of carbon fibers/epoxy resin composites. Journal of Reinforced Plastics and Composites 2012;32(6):393–401.

[114] Wang L-l, Li P, Li L-c, Yu Y-h, Yang X-p. Effect of Surface Properties of T800 Carbon Fibers on Epoxy/Fiber Interface Adhesion. Polymers & Polymer Composites 2013;21(9):607.

[115] Fitzer E, Geigl K-H, Hüttner W, Weiss R. Chemical interactions between the carbon fibre surface and epoxy resins. Carbon 1980;18(6):389–93.

[116] Jiang G, Pickering SJ, Walker GS, Wong KH, Rudd CD. Surface characterisation of carbon fibre recycled using fluidised bed. Applied Surface Science 2008;254(9):2588–93.

[117] Figueiredo JL, Pereira MFR. The role of surface chemistry in catalysis with carbons. Catalysis Today 2010;150(1-2):2–7.

[118] Oh S-M, Lee S-M, Kang D-S, Roh J-S. Microstructural changes of polyacrylonitrile-based carbon fibers (T300 and T700) due to isothermal

oxidation (1): focusing on morphological changes using scanning electron microscopy. Carbon letters 2016;18:18–23.

[119] Larson JV, Smith TG, Erickson PW. Carbon fiber surface treatments; 1971.

[120] Gulyás J, Földes E, Lázár A, Pukánszky B. Electrochemical oxidation of carbon fibres: surface chemistry and adhesion. Composites Part A: Applied Science and Manufacturing 2001;32(3-4):353–60.

[121] Jones C. Effects of electrochemical and plasma treatments on carbon fibre surfaces. Surf. Interface Anal. 1993;20(5):357–67.

[122] Downey MA, Drzal LT. Toughening of carbon fiber-reinforced epoxy polymer composites utilizing fiber surface treatment and sizing. Composites Part A: Applied Science and Manufacturing 2016;90:687–98.

[123] Moosburger-Will J, Bauer M, Laukmanis E, Horny R, Wetjen D, Manske T et al. Interaction between carbon fibers and polymer sizing: Influence of fiber surface chemistry and sizing reactivity. Applied Surface Science 2018;439:305–12.

[124] Kafi A, Huson M, Creighton C, Khoo J, Mazzola L, Gengenbach T et al. Effect of surface functionality of PAN-based carbon fibres on the mechanical performance of carbon/epoxy composites. Composites Science and Technology 2014;94:89–95.

[125] Hexcel ready to fly on the A350 XWB. Reinforced Plastics 2013;57(3):25–6.

[126] Hexcel Corporation. Technical data sheet - HexPly® M21/34%/UD194/T800S; 2011.

[127] Hexcel Corporation. Technical data sheet - HexPly® M20/34%/194/IM7 (12K); 2016.

[128] Jenkins S. HexPly M20 prepreg: A material solution for composite repair. SAMPE Europe Conference 2016 2016.

[129] Solvay. Technical data sheet - FM®300-2 film adhesive; 2011.

[130] Toray Composite Materials America, Inc. Technical data sheet - T700S carbon fibre.

[131] Toray Composite Materials America, Inc. Technical data sheet - T800S intermediate modulus carbon fibre; 2018.

[132] Voisey KT, Fouquet S, Roy D, Clyne TW. Fibre swelling during laser drilling of carbon fibre composites. Optics and Lasers in Engineering 2006;44(11):1185–97.

[133] Rahmani H, Ashori A, Varnaseri N. Surface modification of carbon fiber for improving the interfacial adhesion between carbon fiber and polymer matrix. Polym. Adv. Technol. 2016;27(6):805–11.

[134] Holtmannspötter J, Wetzel M, Czarnecki J von, Brucksch R. Ultra high-resolution imaging of interface layers. Adhes Adhes Sealants 2013;10(4):22–7.

[135] Grünwald W. Application Booklet - Leica EM RES102 Ion Beam Milling System: Ion Beam Preparation of Samples for Electron Microscopy; 2014.

[136] Deutsches Institut für Normung. Aerospace series - Fibre reinforced plastics - Test method; determination of tensile strength of tapered and stepped joints(DIN EN 6066); 1996.

[137] Chung HJ, Rhee KY, Lee B, Lee JH. Effect of oxygen plasma treatment on the bonding strength of CFRP/aluminum foam composite. Journal of Alloys and Compounds 2009;481(1-2):214–9.

[138] Holtmannspötter J, Czarnecki JV, Wetzel M, Dolderer D, Eisenschink C. The Use of Peel Ply as a Method to Create Reproduceable But Contaminated Surfaces for Structural Adhesive Bonding of Carbon Fiber Reinforced Plastics. The Journal of Adhesion 2013;89(2):96–110.

[139] Nakayama Y, Soeda F, Ishitani A. XPS study of the carbon fiber matrix interface. Carbon 1990;28(1):21–6.

[140] Lindsay B, Abel M-L, Watts JF. A study of electrochemically treated PAN based carbon fibres by IGC and XPS. Carbon 2007;45(12):2433–44.

[141] Allington RD, Hamerton I, Hay JN, Howlin BJ, Attwood D. Inverse Gas Chromatography Characterization of Carbon Fiber Surfaces - Effects of Applied Surface Treatment. High Performance Polymers 2005;17(4):561–74.

[142] Lowell S, Shields JE, Thomas MA. Characterization of porous solids and powders: Surface area, pore size and density. Dordrecht: Springer; 2011.

[143] DIN EN ISO 4288:1998-04, Geometrische Produktspezifikation (GPS)_-Oberflächenbeschaffenheit: Tastschnittverfahren_- Regeln und Verfahren für die Beurteilung der Oberflächenbeschaffenheit (ISO_4288:1996); Deutsche Fassung EN_ISO_4288:1997. Berlin: Beuth Verlag GmbH. doi:10.31030/7434013.

[144] DIN EN ISO 4287:2010-07, Geometrische Produktspezifikation (GPS)_-Oberflächenbeschaffenheit: Tastschnittverfahren_- Benennungen, Definitionen und Kenngrößen der Oberflächenbeschaffenheit (ISO_4287:1997_+ Cor_1:1998_+ Cor_2:2005_+ Amd_1:2009); Deutsche Fassung EN_ISO_4287:1998_+ AC:2008_+ A1:2009. Berlin: Beuth Verlag GmbH. doi:10.31030/1699310.

[145] Owens DK, Wendt RC. Estimation of the surface free energy of polymers. J. Appl. Polym. Sci. 1969;13(8):1741–7.

[146] Lauth. Einführung in die Physik und Chemie der Grenzflächen und Kolloide. Berlin, Heidelberg: Springer Berlin Heidelberg; 2016.

[147] DIN 50100:2016-12, Schwingfestigkeitsversuch_- Durchführung und Auswertung von zyklischen Versuchen mit konstanter Lastamplitude für metallische Werkstoffproben und Bauteile. Berlin: Beuth Verlag GmbH. doi:10.31030/2580844.

[148] Tranchard P, Duquesne S, Samyn F, Estèbe B, Bourbigot S. Kinetic analysis of the thermal decomposition of a carbon fibre-reinforced epoxy resin laminate. Journal of Analytical and Applied Pyrolysis 2017;126:14–21.

[149] Feih S, Mouritz AP. Tensile properties of carbon fibres and carbon fibre–polymer composites in fire. Composites Part A: Applied Science and Manufacturing 2012;43(5):765–72.

[150] Akcin Y, Karakaya S, Soykasap O. Electrical, Thermal and Mechanical Properties of CNT Treated Prepreg CFRP Composites. MSA 2016;07(09):465–83.

[151] Arikan E, Holtmannspötter J, Zimmer F, Hofmann T, Gudladt H-J. The role of chemical surface modification for structural adhesive bonding on polymers - Washability of chemical functionalization without reducing adhesion. International Journal of Adhesion and Adhesives 2019;95:102409.

[152] Fiedler B, Hojo M, Ochiai S, Schulte K, Ando M. Failure behavior of an epoxy matrix under different kinds of static loading. Composites Science and Technology 2001;61(11):1615–24.

[153] Al-Turaif HA. Surface morphology and chemistry of epoxy-based coatings after exposure to ultraviolet radiation. Progress in Organic Coatings 2013;76(4):677–81.

[154] Dodiuk H, Goodman SH. Handbook of thermoset plastics. San Diego: William Andrew; 2014.

[155] Dai Z, Shi F, Zhang B, Li M, Zhang Z. Effect of sizing on carbon fiber surface properties and fibers/epoxy interfacial adhesion. Applied Surface Science 2011;257(15):6980–5.

[156] Weitzsacker CL, Bellamy M, Sherwood PMA. Studies of the effect of size on carbon fiber surfaces. Journal of Vacuum Science & Technology A: Vacuum, Surfaces, and Films 1994;12(4):2392–7.

[157] Luo Y, Zhao Y, Duan Y, Du S. Surface and wettability property analysis of CCF300 carbon fibers with different sizing or without sizing. Materials & Design 2011;32(2):941–6.

[158] Page SA, Berg JC, Månson J-AE. Characterization of epoxy resin surface energetics. Journal of Adhesion Science and Technology 2001;15(2):153–70.

[159] Bico J, Thiele U, Quéré D. Wetting of textured surfaces. Colloids and Surfaces A: Physicochemical and Engineering Aspects 2002;206(1-3):41–6.

[160] Figueiredo JL, Bernardo CA, Baker RTK, Huttinger KJ. Carbon Fibers Filaments and Composites. Dordrecht: Springer Netherlands; 2012.

[161] Hackley VA, Stefaniak AB. "Real-world" precision, bias, and between-laboratory variation for surface area measurement of a titanium dioxide nanomaterial in powder form. J Nanopart Res 2013;15:1742.

[162] Meyer LO. Untersuchungen zur Pyrolyse - eine Methode zur Rückgewinnung von Kohlenstofffasern aus CFK-Fertigungsabfällen: Eine Methode zur Rückgewinnung von Kohlenstofffasern aus CFK-Fertigungsabfällen. Zugl.: Hamburg-Harburg, Techn. Univ., Institut für Kunststoffe und Verbundwerkstoffe, Diss., 2011. 1st ed. Hamburg: TuTech-Verl; 2011.

[163] Banea MD. Influence of adherend properties on the strength of adhesively bonded joints. MRS Bull. 2019;44(8):625–9.

Supervised student theses and research projects

Schleich F., Instandsetzung von Rotorblättern an Windenergieanlagen. Research project, 2016. In cooperation with Innogy SE.

Werner H., Numerische Betrachtung der Tragfähigkeit von Faser-Metall-Laminaten in Hinblick auf deren Lochleibungseigenschaften. Master's thesis, 2016.

Reinecke S., Auslegung und Bewertung eines mechanischen Prüfverfahrens für die Nachweisführung von Reparaturen an Schaumsandwichstrukturen. Bachelor's thesis, 2016. In cooperation with Lufthansa Technik AG.

Koord J., Numerische Betrachtung der interlaminaren Bruchzähigkeit von Faser-Metall-Laminaten. Master's thesis, 2016.

Philipkowski T., Validierung analytischer Modelle zur Vorhersage der Druckfestigkeit von Faser-Kunstoff-Verbunden. Research project, 2016.

Hartleib F., Charakterisierung von laserbehandelten CFK-Oberflächen. Research project, 2016.

Schmidt S., Auslegung der Schubsteggeometrien eines 2 MW Holz-CFK-Leichtbau-Rotorblatts. Bachelor's thesis, 2016. In cooperation with PHI blades GmbH.

Lucius L., Bewertung von Oberflächenvorbehandlungen für CFK Strukturklebungen. Bachelor's thesis, 2016.

Großheider K., Mechanische Eigenschaften von CFK-Reparaturen unter Einfluss verschiedener Parameter der Laseraktivierung. Bachelor's thesis, 2017.

Reese J., Parameterstudie über die Aktivierung von CFK-Strukturen durch Plasmabehandlung zur Verbesserung der Klebeeigenschaften und Bruchfestigkeit. Master's thesis, 2017.

Heidari B., Implementierung eines tri-linearen Kohäsivzonenmodells zur Untersuchung des Delaminationsverhaltens von Faser-Metall-Laminaten in einer FEM-Simulation. Research project, 2017.

Hübner H., Erstellung eines parametrischen FEM-Modells zur Simulation von Zugversuchen an Softpatch klebereparierten CFK-Laminaten. Research project, 2017.

Mundkowski J., Weiterführende Entwicklung eines out-of-autoclave-Verfahrens für CFK-Reparaturen in der Luftfahrt. Master's thesis, 2017. In cooperation with Lufthansa Technik AG.

Goralski P., Untersuchung der Ermüdungseigenschaften von geschäfteten CFK-Klebereparaturen. Research project, 2018.

Fuchs J., Einfluss der Prozessparameter laserbasierter Oberflächenvorbehandlung auf die Zugscherfestigkeit von CFK-Klebeverbindungen. Bachelor's thesis, 2018.

Steilmann T., Untersuchung der Auswirkung von plasmaaktivierten Kohlenstofffasern auf die Faser-Matrix-Anhaftung mit dem Single-Fibre Fragmentation Test. Bachelor's thesis, 2018.

Gichev G., Erweiterung eines FE-Models zur Untersuchung des Einflusses einer Nanopartikelmodifikation der Matrix auf die Schadensentwicklung in FKV. Bachelor's thesis, 2018.

Lüllau A., Untersuchung des Einflusses von Laminierabweichungen und Laminataufbau auf CFK Klebeverbindungen mittels Akustische Emissionsanalyse und Digitaler Bildkorrelation. Master's thesis, 2018.

Kanngießer M., Ermittlung des Einflusses von laserbasierter Oberflächenaktivierung auf die Rissausbreitung in CFK Klebereparaturen. Bachelor's thesis, 2018. In cooperation with Lufthansa Technik AG.

Boll B., Entwicklung einer Methode zur prädiktiven Analyse von FTIR Daten. Research project, 2018.

Koert B., Einfluss der Defektgröße und -position auf die mechanischen Eigenschaften von geschäfteten CFK-Klebungen. Bachelor's thesis, 2019.

Thoelen F., Untersuchung laserbehandelter Kohlenstofffasern mit dem Single-Fiber-Fragmentationtest. Bachelor's thesis, 2019.

Mertens J., Entwicklung eines Verfahrens zur Absicherung einer stabilen CFK-Oberfläche für das strukturelle Kleben. Master's thesis, 2019. In cooperation with Airbus SE.

Wonschik K., Auswirkungen der mechanischen Oberflächenbehandlung im Rahmen von Klebereparaturen an CFK-Strukturen. Master's thesis, 2019. In cooperation with Lufthansa Technik AG.